**Dissertation**
**submitted to the**
**Combined Faculties for Natural Sciences and for Mathematics of the**
**Ruperto-Carola University of Heidelberg, Germany**
**for the degree of**
**Doctor of Natural Science**

presented by Dipl. Phys. Jens Hoffmann
born in Kandel/Pfalz
Oral examination: 28.01.2009

# Ionic fragmentation channels in electron collisions of small molecular ions

Referees:

Prof. Dr. Andreas Wolf

Prof. Dr. Thomas Stöhlker

## Kurzfassung

*Ionische Fragmentationskanäle in Elektronenstößen von kleinen molekularen Ionen*

Dissoziative Rekombination (DR) ist einer der wichtigsten Verlustprozesse von molekularen Ionen im interstellaren Medium (IM). Ionenspeicherringe erlauben diesen Prozess unter IM-ähnlichen Bedingungen zu untersuchen. Am Heidelberger Test-Speichering TSR wurde im Rahmen dieser Arbeit ein neues Detektorsystem aufgebaut, um den der DR verwandten Prozess der Ionenpaarbildung studieren zu können. Dieses neuartige System erweitert den vorhandenen Elektrontargetaufbau um die Möglichkeit, in einem Magnetfeld stark abgelenkte negative ionische Fragmente nachzuweisen. Rekombinationsprozesse lassen sich am TSR mit einzigartiger Energieauflösung studieren, indem dem Ionenstrahl zwei voneinander unabhängige Elektronenstrahlen überlagert werden.
In der vorliegenden Arbeit wurde die Ionenpaarbildung der molekularen Ionen $HD^+$, $H_3^+$ und $HF^+$ untersucht. Im Fall von $HD^+$ wurden hoch aufgelöste Quanteninterferenzstrukturen gefunden. Durch Analyse der Quantenoszillationen konnten neue Erkenntnisse über die Reaktionsdynamik der Ionenpaarbildung gewonnen werden. Bei $H_3^+$ war es erstmals möglich, verschiedene Reaktionskanäle getrennt zu beobachten und Interferenzstrukturen nachzuweisen. Die Ionenpaarbildung von $HF^+$ wurde bis hin zu relativen Energien untersucht, für die in früheren Experimenten keine Aussage möglich war.



## Abstract

*Ionic Fragmentation Channels in Electron Collisions of Small Molecular Ions*

Dissociative Recombination (DR) is one of the most important loss processes of molecular ions in the interstellar medium (IM). Ion storage rings allow to investigate these processes under realistic conditions. At the Heidelberg test storage ring TSR a new detector system was installed within the present work in order to study the DR sub-process of ion pair formation (IPF). The new detector expands the existing electron target setup by the possibility to measure strongly deflected negative ionic fragements. At the TSR such measurements can be performed with a uniquely high energy resolution by independently merging two electron beams with the ion beam.
In this work IPF of $HD^+$, $H_3^+$ and $HF^+$ has been studied. In the case of $HD^+$ the result of the high resolution experiment shows quantum interferences. Analysis of the quantum oscillations leads to a new understanding of the reaction dynamics. For $H_3^+$ it was for the first time possible to distinguish different IPF channels and to detect quantum interferences in the data. Finally the IPF of $HF^+$ was investigated in an energy range, where in previous experiments no conclusive results could be obtained.

# Contents

# Chapter 1

# Introduction

Molecules and molecular ions are the key elements in the production of dense clouds in the interstellar medium (IM) and play an important role in the chemistry of planetary atmospheres. Therefore loss mechanisms of molecules are of great interest, especially for light molecular ions like $H_2^+$ or $H_3^+$. Collisions between molecules or molecular ions and electrons, photons, atoms or even other molecules and molecular ions can cause energy transfer between the reactants, rearrangement of the molecular geometry, as well as fragmentation of the ionic molecules. The most important loss process caused by photons or electrons in the IM is Dissociative Recombination (DR), whereas Dissociative Excitation (DE) is mostly caused by ion collisions with heavy targets.
This work focusses on IPF (Ion Pair Formation), a subprocess of DR, leading to negatively and positively charged fragments as reaction products. The storage ring technique provides an experimental framework which allows to study such processes under conditions comparable to those in the IM. Since the 1990's facilities like the Test Storage Ring (TSR) have been used to examine various molecular ions in interaction with electrons or photons. Especially DR was studied for a variety of different molecules starting from the benchmark molecule $HD^+$ and the simplest polyatomic ion $H_3^+$ to heavy diatomic molecules like $HF^+$ or $CF^+$.
On the other hand IPF has received limited attention in the past decades. From the experimental side of view IPF is a challenging field in detector developments at storage rings, because the IPF fragments are strongly bent away from the original pathway in such devices (see chapter 3). However, IPF can also give deep insight into the reaction mechanism of molecular ions in collisions with electrons.
The present work focuses on the detection of ion pair fragments using a new detection system which has been recently installed as a part of the new electron-ion collision setup located at the heavy ion storage ring TSR. The setup consists of an electron beam device [26] and a detection chamber [31] featuring different detectors: one for mainly atomic ion recombination products (MIDAS; [57]) and one for

neutral fragments of ion molecule interactions (BAMBI; cf. [33; 72]). This work completes the detector facility with a detector for strongly deflected IPF fragments (DEMON).
With this newly installed detector for ion pair fragments, experimental data were taken for the most important ionic molecules $H_2^+$ and its deuterated isotope $HD^+$, respectively, for $H_3^+$ and as well as for $HF^+$. The latter is important mainly in industrial applications, while still being detectable in the IM. In the case of $HD^+$ the new results obtained by using the high resolution setup at the TSR, lead to a new theoretical understanding of the fragmentation processes and the involved potential energy curves. Therefore semiclassical calculations were applied, using amongst others the Fast-Fourier-Transformation (FFT) technique, whose empirical application on this problem was developed within the present work. In the case of $H_3^+$ the energetic high resolution of the TSR setup showed energy dependend structures in the IPF cross section which had never been observed before. Thanks to the new electron target setup is was also possible for the first time to distinguish different fragmentation channels in the IPF of $H_3^+$.
The present work firstly provides an overview of IPF and the recombination processes between molecular ions and electrons in general in chapter 2. Chapter 3 then focuses on the experimental details of the new detection setup for strongly deflected molecular fragments which was constructed, taken into operation and refined all along the here presented work. Chapter 4 presents applications of the new setup to IPF measurements on $HD^+$ and $H_3^+$ and discusses the arising implications for theoretical models seeking to describe IPF, namely of $HD^+$. Chapter 5 then presents an IPF measurement performed on $HF^+$. This work concludes with the summarizing chapter 6, which also gives an outlook on possible future experiments to be performed using the new IPF detector setup, as well as possible refinements of the latter.

# Chapter 2

# Electronic collisions of molecular ions

For discussing the various processes of the electronic collisions of molecular ions, it is helpful to use the concept of potential energy surfaces. The most common ansatz to describe the behavior of molecules is the Born-Oppenheimer approximation [48]. Here the many-body-problem is simplified by the assumption that the electrons react instantaneously to the movement of the nuclei, due to the large mass difference between the electron and nuclei. The approximation allows to decouple the treatment of the electronic motion and the nuclear motion and to solve the electronic Schrödinger equation for a potential corresponding to fixed nuclear positions. The resulting eigenvalues produce the potential energy surfaces (PES) and, in the diatomic case, potential energy curves (PEC) respectively.

## 2.1 Interaction of electrons with positively charged molecular ions

The interaction of an electron with a positive molecular ion can lead to various final product species and states. Elastic collisions leave the ion unchanged, whereas inelastic collisions can change the rotational and vibrational (rovibrational) state of the initial molecular ion [33; 69]. Alternatively, processes such as dissociative excitation (DE) and dissociative recombination (DR) cause electron-induced fragmentation of the molecule. In DE scattering of electrons results in charged and neutral fragments of the molecule and the electron remains free, while in DR the molecular compound formed by the electron capture dissociates into neutral products. A process related to DR is ion pair formation (IPF), where positively *and* negatively charged fragments are produced. The focus of this work lies on the

latter electron capture processes, which have been experimentally studied for the molecules $HD^+$, $H_3^+$ and $HF^+$.

### 2.1.1 Dissociative excitation

Dissociative excitation is a scattering process where the molecular ion $AB^+$ is excited by the electron into a repulsive state $AB^{*+}$ and subsequently dissociates in charged ($A^+$) and neutral fragments (B) (see fig. 2.1):

$$AB^+ + e^-(E) \rightarrow AB^{*+} + e^- \rightarrow A^+ + B + e^- \tag{2.1}$$

Depending on the composition of the initial molecular ion the fragments $A^+$ and $B$ can be either atomic or molecular.

The electronic transition into the repulsive state follows the Franck-Condon principle [22; 23; 42], based on the fact that the electrons change their state fast, while the internuclear distances remain the same. The transition probability within the Franck-Condon region (see fig. 2.1) is determined by the overlap of the wavefunction of the bound state $\Psi_{AB^+}$ and the dissociative state $\Psi_{AB^{*+}}(R, E)$ and is described by the Frank-Condon factor $f(v, E)$

$$f(v, E) = \int \Psi^*_{AB^+}(R, v)\Psi_{AB^{*+}}(R, E)\, dR \tag{2.2}$$

with the internuclear distance $R$, the collision energy $E$ and $v$ the vibrational energy level.
For DE this process, even at a fixed value of $E$, is not restricted to a single value of $R$, as the scattering electron may retain some of its kinetic energy and so the transition can occur at any internuclear distance where the initial electron energy $E$ exceeds the excitation energy $E_{\min}(R)$. The energy of the incident electron is possibly transformed into internal excitations of one or even both fragments and the kinetic energy of the products (KER).
A second possible DE pathway can occur already below the energetic threshold for the process described by equation (2.1). Here the electron is captured by the ion forming a neutral excited molecule $AB^{**}$, which autoionizes and dissociates subsequently:

$$AB^+ + e^- \rightarrow AB^{**} \rightarrow AB^{*+} + e^- \rightarrow A^+ + B + e^- \tag{2.3}$$

These mechanisms have been studied previously in storage ring experiments, e.g. on the He-dimer ion at the Test Storage Ring (TSR) in Heidelberg [35]. For this system the energetic threshold mentioned is expected at 6 eV collision energy. The experimental results on DE, however, show a threshold of around 3 eV indicating the importance of the second mechanism (eq. 2.3) mentioned above.

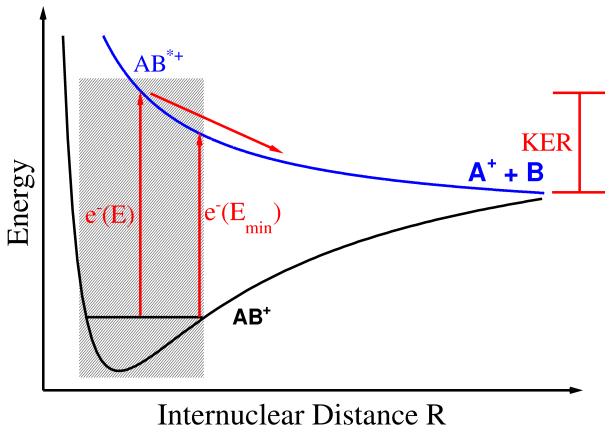


Figure 2.1: *Schematic drawing of the potential energy curves of the electron impact dissociative excitation of a diatomic molecule $AB^+$, capturing an electron $e^-(E)$ into the repulsive state $AB^{*+}$, which subsequently dissociates into the final products $A^+$+$B$ with a Kinetic Energy Release (KER). The transition probability to the repulsive state is given by f(v,E) (see equation 2.2) in the Franck-Condon region (grey shaded area).*

A third DE mechanism is the collision with a residual gas species X in the storage ring, i.e. molecule-molecule as well as molecule-atom collisions. This is the most important loss process for molecular ions in collision experiments [52] and follows the reaction:

$$\mathrm{AB}^+ + \mathrm{X} \rightarrow \mathrm{A}^+ + \mathrm{B} + \mathrm{X} \tag{2.4}$$

Although this process can limit the beam lifetime, it can be very useful by providing information on the ion beam current, for instance through the observed $A^+$ count rate. Assuming no pressure change in the storage ring, and thus no increase or decrease of the amount of residual gas, mechanism 2.4 leads to direct access to the ion beam current and thus to its fluctuations caused by the ion source. This allows to normalize the measured count rates of various processes can be normalized to the residual gas DE rate and, consequently, to the ion beam intensity for relative comparison (see chapter 4 and 5).

### 2.1.2 Dissociative recombination

Dissociative recombination is an efficient destruction process of molecules in ionized media such as interstellar clouds, technical plasmas or the upper layers of

atmospheres. The principle is the following: A molecular ion captures an electron and dissociates into neutral fragments,

$$\mathrm{AB}^+ + \mathrm{e}^-(E) \rightarrow \mathrm{A} + \mathrm{B} + \text{Kinetic Energy Release (KER)}. \tag{2.5}$$

Depending on the electron impact energy $E$ and the initial internal excitation of the ion, fragments are emitted in final states with possible kinetic energy release (KER). In counting experiments, the DR rate coefficient as a function of the electron impact energy is measured. The dynamics of the process become accessible in fragment imaging measurements where the KER as well as the fragment angular distribution are measured [72]. In addition, for polyatomic molecules it is also possible to determine the branching ratios for different final compounds in DR rate experiments using a grid in front of the detector (for more details see [67]) or by a position and mass sensitive detector [34].
Two different DR mechanisms are of importance for the molecular breakup investigations and will thus be described in more detail in the following.

### Direct dissociative recombination

Direct DR is a purely electronic two-step process:

$$\mathrm{AB}^+(\nu, J) + \mathrm{e}^-(E) \rightarrow \mathrm{AB}^{**} \rightarrow \mathrm{A}(n, l) + \mathrm{B}(n', l') \tag{2.6}$$

The principle is illustrated for a diatomic molecule in fig. 2.2, where two PEC representing the bound ionic state $\mathrm{AB}^+$ and the repulsive state $\mathrm{AB}^{**}$ are shown. The capture of the electron leads to the formation of a highly excited neutral molecular compound state which stabilizes by rapid dissociation along the repulsive PEC. For low electron energies a curve crossing close to equilibrium distance, as observed for example in $\mathrm{H}_2^+$ and its isotopomers, is necessary to yield a good overlap of the wave function between the bound state $\Psi_{AB^+}(R, \nu)$ and the neutral dissociative state $\Psi_{AB^{**}}(R, E)$ (see figure 2.2); this overlap is described by the respective Franck-Condon factor $f(v, E)$. Assuming only one dissociative curve per symmetry, and the electronic coupling $V_{el}$ between the states as well as the quantum defect to vary only slowly with the internuclear distance $R$, the direct cross section can be written as

$$\sigma_{DR,direct} = \frac{const}{k^2} \cdot \frac{r}{2} \cdot f(\nu, E)^2 \cdot V_{el}^2 \cdot S \tag{2.7}$$

with a multiplicity ratio $r$ between neutral and molecular electronic states, the electron wavenumber $k$ before the collision and the survival factor $S$, which describes the loss due to autoionization [1].

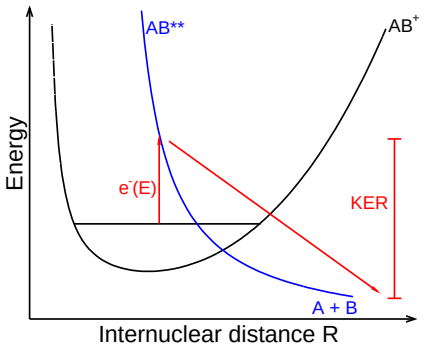


Figure 2.2: *Schematic drawing of the potential energy curves for the direct dissociative recombination mechanism for a diatomic molecular ion; black curve: ground state of the molecular ion; blue curve: repulsive dissociative state.*

**Indirect dissociative recombination**

In systems like $HeH^+$ suitable PEC for direct DR do not exist at low energies but recombination can still efficiently occur through the indirect process due to non-adiabatic couplings [53]. In this mechanism the electron is first captured to form a neutral Rydberg state with the incident molecular ion as the core, which becomes rovibrationally excited in the collision. Subsequently this state can then couple to a repulsive state $AB^{**}$ along which the system can dissociate into neutral fragments,

$$AB^+(v, J) + e^-(E) \rightarrow AB^*_{Ryd}(v', J', n_{Ryd}, l_{Ryd}) \rightarrow AB^{**} \rightarrow A(n, l) + B(n', l'), \quad (2.8)$$

as shown in figure 2.3. The Rydberg states are described by the vibrational and rotational quantum numbers $v'$ and $J'$ and the principal and orbital angular momentum quantum numbers $n_{Ryd}$, and $l_{Ryd}$ of the electron. To each of the ionic PEC a series of neutral Rydberg states converges. This process can interfere with direct DR as the same repulsive state can be taken. The indirect DR process is very sensitive on the energy of the captured electron and, as originally suggested for $H_2^+$, can be responsible for low-energy resonances in various systems [53].

### 2.1.3 Ion pair formation

While extensive experimental and theoretical investigations have been carried out on DR, ion pair formation has received only limited attention for a long time. The reason lies in the difficulties in detecting charged fragments in a storage ring, especially light ones and those with a charge opposite to the initial ion, i.e. negative ions. The process is initiated similarly as DR by electron capture, but the intermediate molecular system dissociates into charged fragments (see figure 2.4):

$$AB^+(v, J) + e^-(E) \rightarrow AB^{**} \rightarrow A^- + B^+(n', l') \quad (2.9)$$

In general, the ion pair channel is one of several final Rydberg states. Thus, the cross section for ion pair formation depends on the branching among possible final

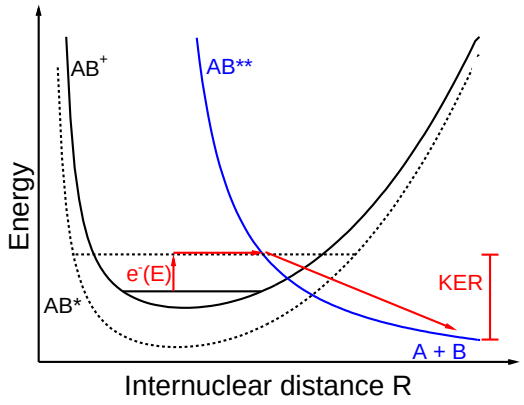


Figure 2.3: *Schematic drawing of the potential energy curves for the direct dissociative recombination mechanism for a diatomic molecular ion; black curve: ground state of the molecular ion; black dashed curve: neutral excited Rydberg states; blue curve: repulsive dissociative state.*

reaction channels.
As shown in figure 2.4, the excited potential curve $AB^{**}$ crosses (in a picture neglecting the coupling between the various curves) the final state curves, which leads to the dissociation of the molecule in an ion pair. In case coupling between this PEC and the Rydberg states becomes important and the situation can change, for example as observed for $HD^+$ (see chapter 4). Following the reaction dynamics the system, represented by wave packets, emerges after the electron capture along the dissociative pathway. The coupling of the states now opens different pathways towards the ion pair limit. At small internuclear distances a split up of the wave-packet becomes possible, similar to the two slit experiment in the quantum mechanics. If a second crossing at large internuclear distances is available, these wave-packets can transit back to the original pathway and interfere. This will result in characteristic interference structure. The transition probability between two states is described by the Landau-Zener formula [16]

$$P_{ij}(E) = 1 - exp\Big( - \frac{2\pi c_{ij}^2}{\alpha v} \Big) \tag{2.10}$$

with $c_{ij}$ the electronic coupling matrix element between the states $i$ and $j$, $\alpha$ the slope difference between the potentials, and $v$ the relative velocity of the fragments [10; 79].

## 2.2 Fragmentation experiments in storage rings

Experiments on the fragmentation of molecular ions require good control on the ions as well as on the collision partners of the ion beam. By using the storage ring technique the molecular ion beam can be prepared while it is circulating on a closed orbit. In the next section this technique will be described in more detail, followed by an introduction to the basic concept of performing rate measurements.

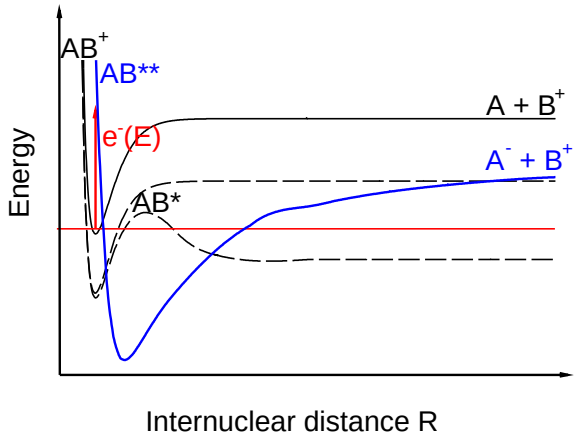


Figure 2.4: *Schematic drawing of potential energy curves involved in the ion pair formation; black solid line: ionic ground state; blue curve: dissociative state; black dashed curves: Rydberg potential curves.*

### 2.2.1 Multipass merged beam technique

A storage ring combines sources of ion production with a ring system, where the ions are circulating on a closed orbit. The closed orbit is achieved either using magnetic or electrostatic fields, so that the storage times much longer than the revolution time can be reached. This means that the ion beam passes a defined interaction region at each revolution and the ions can be manipulated carefully. The ions can either be excited, deexcited, charge-changed or, in the case of molecules, be destroyed with subsequent detection of the fragments. In order to get a well-defined beam, a cooling procedure of the initially intrinsically hot ions is needed. Through active cooling of an ion beam with electrons [39] or photons [74], well-defined conditions for experiments are achieved, e.g., the velocity spread of the ion beam becomes negligible and the ion beam size shrinks in coordinate space.
Two types of storage ring are possible. On the one hand electrostatic storage rings are available, for instance ELISA at the University of Aarhus [73], which rely on the electric charge of the injected ions and the strength of the electric field. The advantage is that the force which keeps the ions on the closed orbit depends only on the strength of the electric field and the charge state of the ion, and is thus independent of the ion mass at a given kinetic energy of the beam. The disadvantage, on the other hand, is that such rings are typically operated at beam energies of tens of keV, making it difficult to handle in particular light ions. On the contrary, higher beam velocities are accessible in magnetic storage rings for light ions. This allows to realize small relative energies between the ion and the merged electron

beam, enhancing the energy resolution in the experiments.
On the other hand in magnetic ion storage rings, in operation since the 1980s, as for example the Test Storage Ring (TSR) in Heidelberg [62], the Experimental Storage Ring (ESR) at the GSI in Darmstadt [11] or CRYRING at the Manne Siegbahn Laboratory in Stockholm [46], the ion beam is kept on a closed orbit due to the Lorentz force, which depends on the mass-to-charge ratio. This limits the storage of high mass ions, such as large biomolecules, depending on the rigidity of the bending magnets. The advantages, on the other side, are the possibility to achieve higher beam energies for low mass ions, which increases the maximum storage times. The next section will focus on different aspects of magnetic storage rings which have been used for the experiments presented in this thesis.

### Magnetic storage rings

In magnetic storage rings the ions are stored on a closed orbit by bending dipole magnets (see fig. 2.5 and for example [62]). The energy of the stored ion beam is limited by the magnetic rigidity $\overrightarrow{B}\overrightarrow{\rho}$ of the storage ring, with the magnetic field $\overrightarrow{B}$ and the radius of the ion beam trajectory in the dipole magnets $\overrightarrow{\rho}$. This limits the energy of the ion beam:

$$E_{ion} = (B\rho)^2 \cdot \frac{q^2}{2 \cdot m_{ion}}, \text{ with } m_{ion} = \frac{m(^{12}\text{C})}{12} \cdot A \tag{2.11}$$

$$\Rightarrow E_{ion} \approx 47.93 \cdot (B\rho)^2 \cdot \frac{q^2}{A} \text{ [MeV]}. \tag{2.12}$$

The maximum kinetic energy of the ion beam is inversely proportional to the mass $A$ of the molecular ion and thus decreases for heavier species, which is the most important limiting factor for such devices. Thus the beam lifetime itself is limited by collisions of the ion beam with atoms or molecules of the residual gas in the storage ring. These collisions lead to breakup of molecules or to a change in the charge of an atomic ion. Additionally, they increase the background count rate of the experiments performed at the storage ring. To minimize the mentioned residual gas influence on the ion beam, it is necessary to provide good vacuum conditions in the range of $10^{-11}$ mbar.

Using a radio frequency (RF) accelerating electric field synchronized to the ion beam revolution, a storage ring can also be utilized as a synchrotron and the ion beam can be further accelerated in the ring (see chapter 5). This requires synchronous control of the bending field intensity as it is provided at the TSR [43] or at Cryring [46].
The ions for the experiments are provided by an ion source, where in the most common way the ions are produced in a plasma chamber. The discharge employing

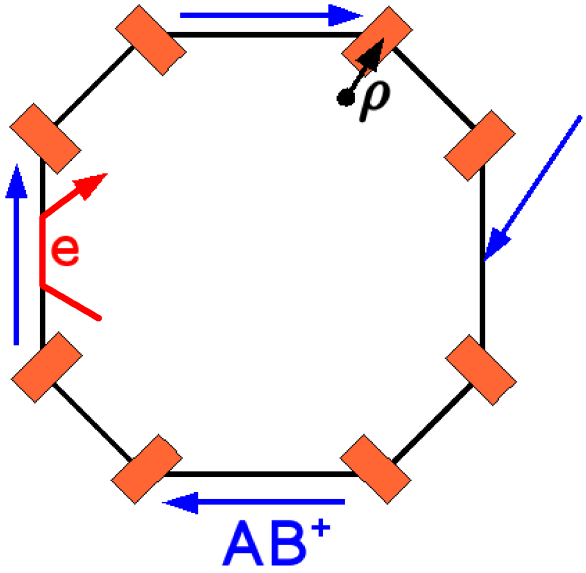


Figure 2.5: *Sketch of a magnetic storage ring. Ions from an accelerator are injected (right hand side) and stored (blue arrows). Dipole magnets (orange) bend the beam onto a closed orbit. The bending radius is marked with the black arrow ($\overrightarrow{\rho}$). In one straight section a target beam can be merged with the ion beam. This can be either photons or, like in the sketch electrons (red arrow). Not shown here are detection and diagnostic instruments (see fig. 2.10)*

electron collisions, this leads to intrinsic excitation of the ion, as well as to a large spread of the ion beam in phase space. Two types of cooling are thus necessary.

### Internal cooling

Internal cooling is provided by spontaneous emission if the lifetimes of the radiatively decaying states are short compared to the storage times. This process is possible for infrared-active molecular ions only, which can cool down vibrationally and rotationally to thermal equilibrium with the chamber walls during the storage. Molecules end up mostly in the vibrational ground state while the lowest rotational states can remain excited. A prominent example for this cooling process is the $HD^+$-molecule, where the ground state is reached within several ms for the vibrational excitation [83].
Rotational and vibrational excited states of molecules lacking an electric dipole moment, like $H_2^+$, cannot cool radiatively. Here an electron beam can induce vibra-

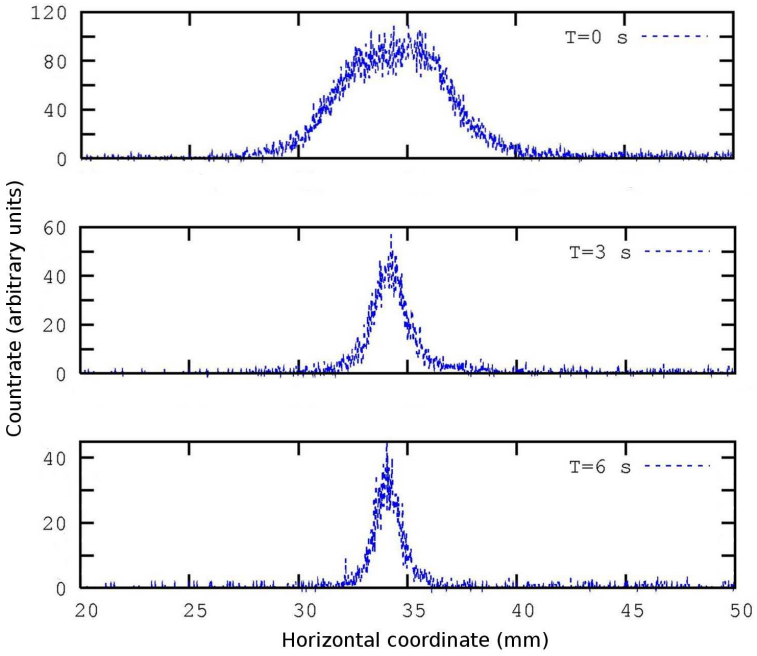


Figure 2.6: *Phase space cooling of the diatomic molecule $CF^+$ in a storage ring. Shown are horizontal beam profiles with the count rate of the ions in arbitrary units versus a horizontal coordinate in mm inside the beam tube. The FWHM represents the width of the ion beam during the cooling procedure. A final width of 1mm was reached as can be seen in the last panel. [50]*

tional and rotational cooling by superelastic collisions (SEC), where rovibrational energy is transferred from the ion to the electron

$$H_2^+(v, J) + e^-(E) \rightarrow H_2^{**} \rightarrow H_2^+(v', J') + e^-(E + \Delta E), \tag{2.13}$$

where $v' < v$, $J' < J$ and $\Delta E > 0$ [55].
The effects of this type of cooling were observed in several experiments for example on $D_2^+$ [56] or $H_2^+$ [80]. Using the Coulomb Explosion Imaging (CEI)- technique at the TSR, SEC for $H_2^+$ was studied in more detail, finding this process to be mainly responsible for the vibrational deexcitation [70].

### Phase space cooling

An electron beam merged with the ion beam in a straight section of a storage ring can provide phase space cooling, as the electrons can absorb thermal energy of the ions. Since the electrons are produced colder than the ions and permanently renewed, active cooling of the ions is induced through collisions. In fig. 2.6 a

recent example for phase space cooling of an ion beam of the diatomic molecule $CF^+$ is shown [18]. In this case the ion beam was merged with an electron beam over a length of about 1.5 m. The data were taken at the Heavy Ion Test Storage Ring (TSR) in Heidelberg using a Beam Profile Monitor (BPM) (see section 2.3). It can be clearly seen that the width of the beam shrinks to a small diameter of 1 mm. A cooling time of 4.4 s was extracted from the data set [50]. Another recent example is the cooling of $HF^+$ which was demonstrated using an imaging system located at the TSR. Here a projection of the ion beam during cooling is given by using fragmentation products from the DR process and calculating the projected distance of the two fragments H and F. In this case the shrinking of the distribution of the center-of-mass of the horizontal and vertical coordinate show indirectly the cooling of the ion beam (see figure 2.7). To reach such optimal beam properties the electron beam has to be merged with the ion beam at a velocity $v_e$ matching that of the ions $v_{ion}$. The electron beam conditions are determined by the specific conditions of the electron source. Some basics on electron beams and sources will be given in the following.

### Electron beam properties

To emit electrons from a surface they have to overcome the material specific work function. This can be achieved in various ways. Most commonly used are either thermal emission or laser-stimulated photoemission. For the thermal emission, a part of the Boltzmann electron energy distribution in the conductor is simply "pushed" above the work function by heating of the emitter material. For the photoemission, the electrons are photoexcited to the conduction band of a semiconductor material. Deposition of a Cs/O monolayer onto the semiconductor surface lowers the vacuum level below the conduction band energy (for more

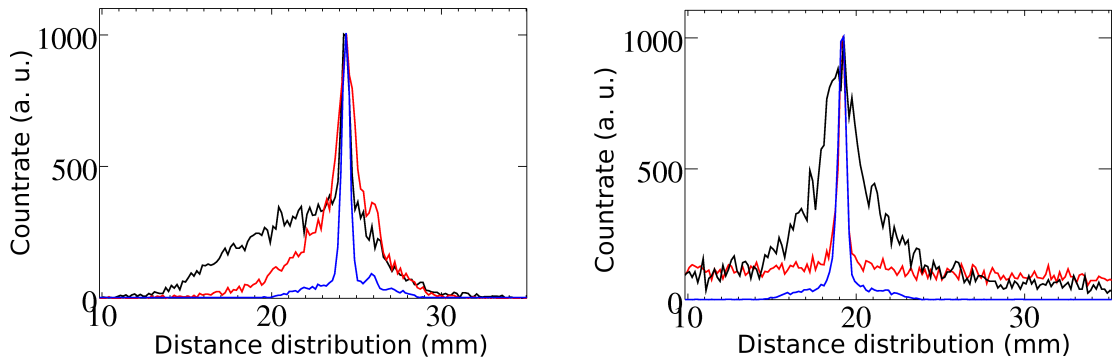


Figure 2.7: *Transverse center-of-mass distribution during the cooling procedure of $HF^+$. (a) Distribution in x direction on the imaging detector and (b) y direction; black curves t = 0-2 s; red curves t = 3-4 s; blue curves t = 10-12 s [44].*

details see [76]). For the latter technique the cathode can be cooled down to the temperature of liquid nitrogen to reach ultimately low initial energy spread of the emitted electron cloud. The energy dilation of the electron beam limit the ion beam temperature that can be reached by phase space cooling.
In order to merge the electron bath and the ion beam, the electron beam is manipulated with magnetic fields so that the two beams interact under an angle of 0°. Due to these fields the initial temperature of the electrons, $T_\perp$ and $T_\parallel$ are decoupled. The cathode properties and operating conditions determine the initial transverse temperature. In order to reduce the temperatures the electron beam is expanded and accelerated adiabatically. While the expansion is realized by the passage of the electrons from a high magnetic field intensity in the range of $B_i = 10000$ G to a low magnetic field of $B = 400$ G, the adiabatic acceleration is provided by slowly increasing the kinetic energy of the electrons by a set of electrodes in the first stage of the electron target (see [26; 57]). The final transverse temperature is then expressed by

$$k_B T_\perp = \frac{B}{B_i} k_B T_{\perp,i}, \tag{2.14}$$

with a magnetic field strength $B$ after expansion and the magnetic field in the cathode region $B_i$. The ratio of both is called the expansion factor $\xi = B_i/B$. The longitudinal temperature is mainly the result of the kinetic transformation. Upon acceleration of the electrons to ion velocity, the initial longitudinal energy spread is maintained. The corresponding velocity spread however, decreases because of $E \sim v^2$. As the temperature is related to the velocity spread through $k_B T_\parallel \sim \Delta v^2$ and $\Delta v_f = \frac{dv(E)}{dE}\Delta E = \frac{1}{\sqrt{2mE}}(kT_\parallel)$, the final longitudinal temperature is given by

$$k_B T_{\parallel,f} = \frac{1}{2} m \Delta v_f^2 = \frac{1}{2E}(k_B T_{\parallel,i})^2. \tag{2.15}$$

Additional contributions arise from two heating effects, the transverse-longitudinal-relaxation (TLR) and the longitudinal-longitudinal-relaxation (LLR) [57]. The final longitudinal temperature is thus given by

$$k_B T_\parallel = k_B T_\parallel^{kin} + \frac{\partial \Delta E_{TLR}}{\partial x} dx + \Delta E_{LLR} \tag{2.16}$$

Due to the non zero temperatures the resolution of the collision experiment is limited by the velocity distribution of the electrons

$$f(v) = \frac{m_e}{2\pi k_B T_\perp} \left( \frac{m_e}{2\pi k_B T_\parallel} \right)^{\frac{1}{2}} \times \exp\left( -\frac{m_e v_\perp^2}{2k_B T_\perp} - \frac{m_e (v_\parallel - v_d)^2}{2k_B T_\parallel} \right), \tag{2.17}$$

with $v_d = v_{detuning}$, a velocity which is not equal the cooling velocity.
Since $kT_\parallel \ll kT_\perp$ this so called flattened double Maxwellian electron distribution

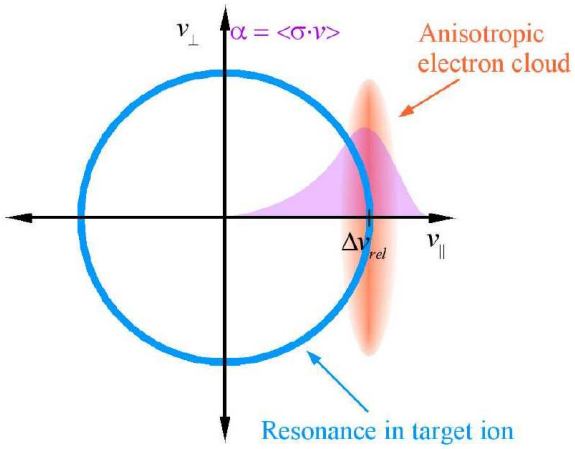


Figure 2.8: *The anisotropic electron distribution in the velocity frame is shown as a lens (orange), while the ion beam resonance forms a hollow sphere (blue circle). Tuning the relative energy of the electrons and therefore the velocity, the electron cloud moves along the x-axis forming the observed peak structures (violet) with an extended low energy tail [57].*

has the form of an ellipsoid in the velocity space. In the same frame the narrow ionic resonance is represented by a hollow sphere. While changing the relative energy of the ion and electron beam the electron distribution moves along the $v_\parallel$ axis. The overlap of the sphere and the distribution results in the observed peak structure with a long low energy tail and a sharp drop on the high energy side (see fig. 2.8).
The relative energies are calculated by subtracting a space charge potential from the directly measured energy. This potential is created through the repulsive Coulomb force between the electrons. If an electron approaches the beam it is screened by $\Phi_{SC}(r, n_{e^-})$ and so the kinetic energy is lowered. If one assumes a cylindrical electron beam with a homogeneous density profile in a cylindrical beam tube the space charge potential is [57]

$$\Phi_{SC}(r, n_e) = \frac{n_e e r_{beam}^2}{4\epsilon_0} \begin{cases} 1 - \left(\frac{r}{r_{beam}}\right)^2 + 2ln\frac{r_{tube}}{r_{beam}} & \text{,for } r \leq r_{beam} \\ 2ln\frac{r_{tube}}{r} & \text{,for } r_{beam} > r > r_{tube} \end{cases} \tag{2.18}$$

The electron energy is then defined by

$$E_{lab} = eU_0 - e\Phi_{SC}(r, n_e). \tag{2.19}$$

with the measured potential $U_0$.
In the experiments the energy resolution depends on the electron temperatures,

whereas the space charge correction is important for obtaining the correct energy in the center of mass frame. The electron beam setup at the TSR enabled to realize a high energy resolution (see chapter 2.3) in the measurements on the cross sections (chapter 4) and rate coefficient (chapter 5).

### 2.2.2 Rate measurements

During molecular reactions, rate measurements with interacting electron and ion beams, the electrons serve as a target. With the measured density of the electrons $n_e$, the ion current $I_{ion}$ in the storage ring and the electron energy dependent detector counts $D(E)$ one is able to determine the rate coefficient as a function of the collision energy $E$ of the electron and ion recombination

$$\alpha(E) = \frac{D(E)}{I_{ion} n_e} \frac{L}{l}, \tag{2.20}$$

with the scaling factor $\frac{L}{l}$, where $L$ is the length of the storage ring and $l$ the interaction length between ions and electrons.

The total kinetic energy in the center-of-mass frame of electron and ion is, in a nonrelativistic approximation, given by

$$E_{CM} = (\sqrt{E_{d,lab}} - \sqrt{E_{cool,lab}})^2 \tag{2.21}$$

where $E_{cool,lab}$ is the electron energy corresponding to the electron velocity matching the one of the ions, measured in the laboratory frame, and $E_{d,lab}$ is the energy difference of the detuned electron beam with respect to $E_{cool,lab}$, also measured in the laboratory frame. Both energies have to be space charge corrected according to equation 2.18 and 2.19.
The measured rate has to be corrected in order to take into account that in the merging and demerging regions an angle between the two beams occurs and therefore the relative energies are different than in the straight interaction region. This so-called toroidal correction (see chapter 4) typically leads to a higher rate coefficient than initially measured. In order to compare the theoretical recombination cross section $\sigma$ with the experimental rate coefficient the former has to be convoluted with the electron velocity distribution (see equation 2.17) in the center-of-mass-frame

$$\alpha(v_d) = \int_0^\infty \sigma(v) v f(v_d, \overrightarrow{v}) d^3v = < \sigma v >_{v_d} . \tag{2.22}$$

Considering equation 2.17 one is able to distinguish the electron temperatures from the measured line width using fitting routines where the electron temperatures are kept as free parameters [29].

## 2.3 Acceleration and storage ring facilities at the MPI-K

### 2.3.1 Accelerator facility at the MPI-K

At the Max-Planck-Institute for Nuclear Physics three accelerators with exchangeable ion sources (see fig. 2.9) are used to produce ion beams for the heavy-ion Test Storage Ring (TSR). Two accelerators are based on the Van-de-Graaff principle, where a high voltage platform is charged to several million volts by a rotating pelletron chain. The so called MP-Tandem accelerator requires negative ions as precursors, so that the final beam is then produced by charge transfer in a gas target located in the middle of the acceleration distance on the high voltage platform. In contrast the ISSI accelerator is a single ended Van-de-Graaff accelerator which can reach up to 3 MV. Here, the ions are produced directly in the desired charge state by a source mounted on the high voltage terminal inside the steel tank. The High Current Injector (HCI) consists of a 6 m long radiofrequency-quadrupole (RFQ) section followed by eight drift tubes with seven accelerating gaps [51]. Employing the focusing effect of this quadrupole structure yields to high currents and prevents in particular the slow beam to blow up through intra-beam repulsion. Subsequent to these accelerators a post-accelerator allows to increase

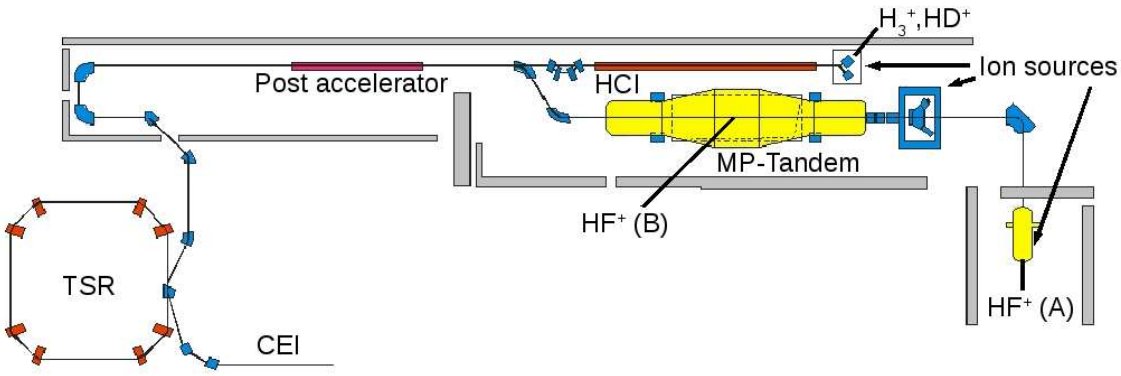


Figure 2.9: *The MPI-K accelerator facility. On the right hand side the ISSI used for the $HF^+$ ion pair measurement, in the middle the MP-Tandem which was used for the $HF^+$ DR measurements ($HF^+$(B)), above the High Current Injector (HCI) which was used with the post accelerator (top left) for the $HD^+$ and $H_3^+$ ion pair measurements. Right top inside the squares the location of the high voltage platform of the used ion sources ($HF^+$(A), $HF^+$(B), $HD^+$ and $H_3^+$). Down left the TSR facility were the measurements took place. Attached to the TSR is the Coulomb Explosion Imaging (CEI) beamline (cf [33])*

further the beam energy before reaching the TSR.
For the experiments presented in this work the following sources have been used with the accelerator facility: In the $HD^+$ as well as the $H_3^+$ measurement the so called CHORDIS (Cold or HOt Reflex Discharge Ions Source) ion source was used. Thereby the ions were directly produced from an $H_2$ and $D_2$ gas mixture in the case of $HD^+$ and $H_2$ gas only for $H_3^+$. Subsequently the ions were accelerated to a final energy of 5.19 MeV using the HCI and the downstream following post accelerator. Later experiments on the ion pair formation of $HF^+$ were performed with the ISSI accelerator equipped with a penning source. Here the energy is limited to 2.6 MeV. so that the ions had to be further accelerated inside the storage ring by using the synchrotron mode of the TSR [43] and to reach the desired final energy.

### 2.3.2 The ion storage ring TSR

The TSR is a magnetic storage ring with ultrahigh vacuum (UHV) conditions (p $\simeq 5 \times 10^{-11}$ mbar) and a circumference of approximately 55.4 m. The closed orbit is provided by the magnetic field of eight dipole magnets with a deflection of 45° each. They are grouped pairwise with a small straight section in between. Between each group are long straight sections, where the beam injection and extraction, electron cooling, the beam diagnostics, the radiofrequency (RF) cavity and the experimental setup are placed (see fig. 2.10). The stored beam is focussed using quadrupole magnets in doublet and triplet configuration. With this ring setup ion beams with a maximum rigidity $B\rho$ of 1.5 Tm can be stored.
For a stored ion beam the Schottky pickup is one diagnostic instrument, which allows to measure the ion beam revolution frequency. This is done using cylindrical pickups surrounding the ion beam. With this assembly the AC component of the ion beam can be measured directly in order to reconstruct the revolution frequency and its spread. The frequency spread is a measure for the momentum spread of the ion beam. A cooled ion beam has a typical frequency spread of $\Delta f/f \sim 10^{-4}$.

Using rest gas ionization by the ion beam it is possible to determine the horizontal and vertical beam position in the beam tube. This is done using a homogeneous transverse and vertical electrical field to map the ion beam position on position sensitive detectors (resistive anode). This so called Beam Profile Monitor (BPM) can in principle also be used to record the ion beam current as for instance applied in atomic lifetime measurement [21] or dielectronic recombination experiments on atomic ions (cf. [24]). Another instrument to measure the current is a DC transformer where the induced signal on the ion current monitor (see fig. 2.10) is measured directly as a current equivalent value. However, both methods are often not applicable for molecular beams because of the low intensity of the ion beams which are mostly limited either by the ion production. Also, in particular the neutral particle detectors at the BAMBI-beamline can only be exposed

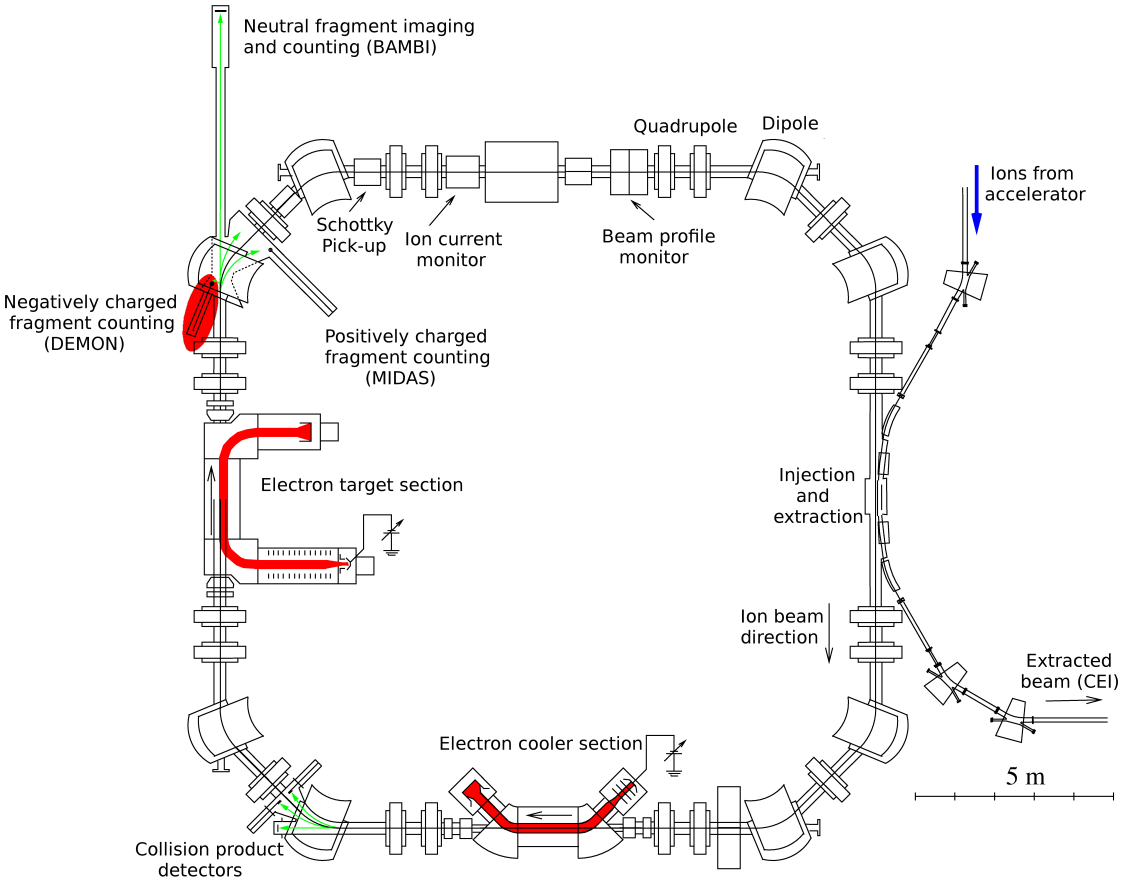


Figure 2.10: *The Test Storage Ring at the Max-Planck-Institute for Nuclear Physics. The beam is injected at the right hand side (blue arrow). In the next straight section the cooling electron beam (red) from the Electron cooler is merged with the beam. The following dipole magnet encloses a detector chamber. In the next straight section follows the electron target (in red the electron beam) including the experimental area, with the dipole chamber for the DEMON and MIDAS detectors as well as the BAMBI- setup for neutral products. Finally the diagnostic straight section with the Schottky Pick-up and the BPM. Also drawn but not discussed in this work is the extraction beamline at the injection. In this beamline Coulomb-Exposion-Imaging (CEI) measurement can be performed (e.g. [33]).*

to a limited count rate. The ion pair detector on the other side can handle high count rates and therefore, if high intensity ion beams as in the case of $HD^+$ and $H_3^+$are available, a combination of DC measurement and the restgas induced DE rate detected at a detector located inside the TSR (MIDAS, see next chapter and [57]) can be used to obtain an absolute calibration of the ion beam current (see chapter 4). Nevertheless although a high intensity beam was available in the $HF^+$ ion pair measurement only the MIDAS-detector was used to record the ion current as discussed separately in chapter 5.
A unique tool at the TSR is the twin electron beam setup. Here two electron beams can be merged independently with the ion beam to provide very stable ion beam conditions and to simultaneously conduct high precision measurements of the rate coefficients. Beam dragging can thus be reduced to a minimum, in particular approaching low relative energies [26]. Since 2003 the electron target has been in operation at the TSR. The colder longitudinal and transversal temperatures reached by the electron target, results in a better energy resolution compared to the electron cooler, so that latter was since then mainly used to cool the ion beam and define its energy (see below).

### 2.3.3 The electron beam setup at the TSR

The energy resolution depends on the energy spread of the electron beam, which is highly sensitive to the production method of the electron beam (see chapter 2.1). For the twin electron setup of the TSR one has the following situation: The electron cooler is mounted perpendicular to the TSR plane and is equipped with a thermal cathode producing the electron beam, which is guided in and out of the TSR with a magnetic guiding field. The electron beam is expanded by a factor $\xi$ of 9.6. The electron cooler provides typical electron currents of a few mA and densities $n_{e,cooler}$ of approximately $2 \times 10^7$ cm$^{-3}$. Transverse and longitudinal temperatures $kT_\perp \approx 10.0$ meV and $kT_\parallel \approx 0.1$ meV are achieved. For the electron target two different types of cathodes are available: On one hand a thermionic cathode and on the other hand a photocathode. In both setups the electrons are detached from the emitter material using an extracting voltage. Then the beam is magnetically expanded by a factor $\xi$ between 10 and 50 and further accelerated using a set of electrodes mounted in the target acceleration section (see [26]). The beam is guided in and out of the TSR using toroidal magnets (see [26]) and the expansion is adapted to the needs of the respective experiment.
Depending on this setting, typical densities in the range of $n_{e,target} \approx$ 1-5 $\times 10^6 cm^{-3}$ are reached. The difference of the two types of cathodes lies in the production mechanism. For the termionic cathode a relatively high current is applied on the cathode material ($I_{ca} = 1.25$ mA) which leads to cathode temperatures of $T_{cath} \approx$

1000 K. In contrast, the photocathode material (GaAs-samples) is cooled down to liquid nitrogen temperatures and the electrons are emitted from the samples using laser light. The resulting temperatures are typically one order of magnitude lower. ($T_{cath} \approx 100$K). This difference is reflected comparing the longitudinal and transversal temperatures. While the thermionic cathode leads to temperatures of $kT_{\perp} \approx 2.0$ meV and $kT_{\parallel} \approx 0.045$ meV respectively, the photocathode temperatures are $kT_{\perp} \approx 0.5$ meV and $kT_{\parallel} \approx 0.03$ meV. Nevertheless both types of cathodes have smaller temperatures than the cooler and therefore the resolution of the target, described by equation 2.17, is more independent of the electron source. This also shows up if the cooling performance of both devices is compared like it is shown in fig. 2.11. Taken everything into account it explains the preference for the target section for all molecular experiments.
Downstream of the electron target various detectors are installed awaiting neutral and charged fragments coming from the interaction section. Neutral fragments are detected in the Beamline for Advanced Molecular Breakup Investigations (BAMBI) where several detectors are located. A camera system mounted about 12 m from the interaction region allows molecular breakup imaging (for details see [72]) and for measurement of the DR and DE rate coefficient two surface barrier detectors are available [33; 61]. Positive fragments are detected with the MIDAS detector [57] already in the TSR dipole chamber [31] located downstream the electron target, while the negative fragments are measured using the DEMON-detector described in the following.

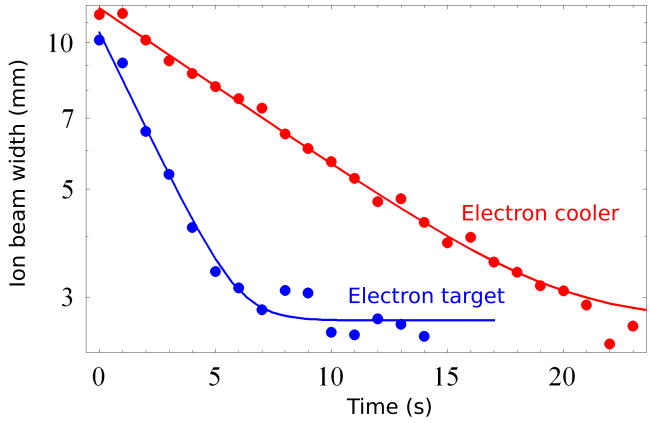


Figure 2.11: *Comparison of the horizontal cooling time of $CF^+$ of the electron cooler and electron target. Fitting of the exponential decay leads to the cooling times $\tau_{ecool} = 13.5$ s and $\tau_{etarget} = 4.4$ s respectively.*

# Chapter 3

# Detection of strongly deflected ions

Many of the molecular collisions discussed in chapter 2 lead to ionic product channels with fragments of strongly different charge-to-mass ratio as compared to the initial molecular ion. The detection of these fragments ions imposes a number of new challenges to the storage ring technique, as in many cases they require a special set of detection devices. This is caused by the strong influence of the storage ring beam optics on these fragment ions and their corresponding large excursions from the stored beam orbit. The next sections give an outline of the detection system created for enlarging the range of ionic fragments accessible in experiments at the TSR.

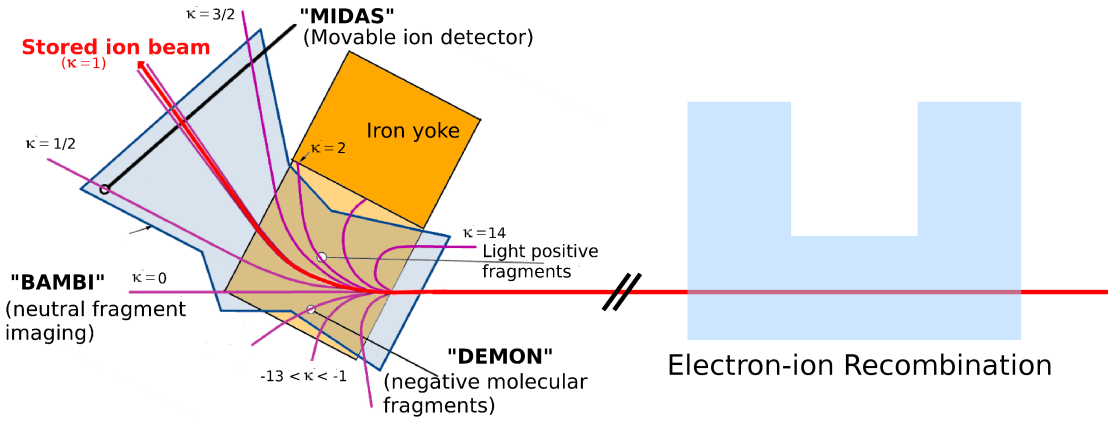


Figure 3.1: *Schematic top view of the dipole chamber located downstream the electron target. The horizontally movable DEMON-detector (bottom) is operating in the range $\kappa$ smaller than one.*

## 3.1 Magnetic fragment selection

In electron-ion collision experiments the energy release is in the eV range and therefore small compared to the ion beam energy which is in the MeV region. Then the product ions remain close to their original trajectory in the straight sections of the TSR. In the following dipole magnet (of inductance $B$) they are separated according to their orbital radius (see figure 3.1)

$$r = \frac{mv}{qB} \tag{3.1}$$

as given by their mass $m$, charge $q$ and velocity $v$. A useful parameter to relate the charge to mass ratio of product and ion is $\kappa$ [57], defined as

$$\kappa = \frac{q_p/m_p}{q_i/m_i}, \tag{3.2}$$

where $p$ indicates the products and $i$ the original circulating ion.

So one can define the radius of the products $r_p$ in the dipole field as a function of $\kappa$ by

$$r_p(\kappa) = \frac{r_i}{\kappa} \tag{3.3}$$

where $r_i = 1.15$ m for the TSR. Due to the dependence of the radius on the charge, movable detectors are needed for fragment detection. For neutral fragments the detectors can be installed in a fixed position (see fig. 3.1).
For products from atomic ion species ($m_p = m_i \pm m_{e^-} \approx m_i$, because $m_e \ll m_i$) the ($\kappa < 1$) -range corresponds to a capture of an electron ($q_p < q_i$), whereas products of an ionization process have $\kappa > 1$ ($q_p > q_i$). These cases are covered by the MIDAS detector [57] outside the magnetic field of the dipole. The molecular case is much more difficult, because a wide spectrum of masses and charge states in the products is possible. For charged fragments the required detection radius is mass dependent and lies in the range of $\kappa > 1$ for DE and $\kappa < -1$ for IPF, while for neutrals $\kappa$ is zero. For the latter the BAMBI beamline can be used (see [72]), whereas for $\kappa$ with $1 < \kappa \leq 3/2$ the MIDAS detector can be used [57]. Fragments with $\kappa > 3/2$ and $\kappa < -1$ were not detectable with the existing detector setup. In summary, there are four different categories of $\kappa$ for a positive ion beam. The star marks $\kappa$ ranges which were not accessible before the installation of the new detector setup:

| | | |
|---|---|---|
| $\kappa < 0$ | : | Negative fragments and reloaded atomic ion products ⊛ |
| $\kappa = 0$ | : | Neutral fragments |
| $1/2 \leq \kappa \leq 3/2$ | : | Positive molecular fragments, atomic ion products |
| $3/2 < \kappa$ | : | Light positive molecular fragments ⊛ |

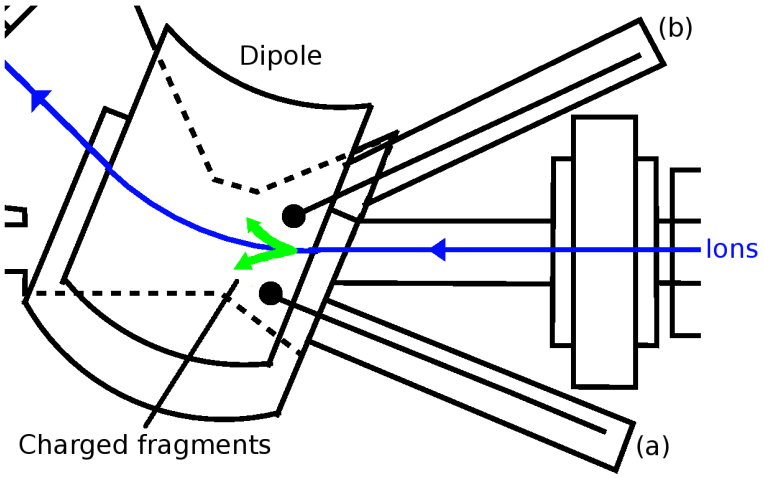


Figure 3.2: *Schematic view from top and outside of the TSR onto the dipole chamber. In the right upper corner the detector forseen for light positive fragments (b), on the bottom the DEMON detector for negative fragments (a).*

## 3.2 The DEMON detector

As part of the equipment of the TSR electron target, two positions have been included in the design of the downstream dipole chamber for detecting the molecular breakup in light charged fragments: one inside the TSR covering the light positive fragment ($3/2 < \kappa$) and one outside for the negative fragment detection ($\kappa \leq -1$) (see figure 3.2). To cover a wide $\kappa$ range, each detector has to be movable. A single detector setup has been designed by Wissler [31]. Within this work, this setup was constructed, installed and taken into operation. It was chosen to assemble this detector on the outer position ((a) in figure 3.2) in order to give access to a new molecular process not studied at the TSR before, namely ion pair formation (IPF). Only a negative fragment provides a clear signature of IPF (see chapter 2). This detector, called DEMON – DEtector for MOlecular Negative fragments – (see fig. 3.3) was installed in 2005 and will be discussed in detail in the following.

### 3.2.1 The hardware of the detector setup

The basic layout of the setup consists of a vacuum chamber, a translation stage and manipulator arm (see fig. 3.3) separated from the TSR by a UHV-valve (i). An ion getter pump is mounted on top of the vacuum chamber (ii) (see also figure 3.4(a)), whereas a Ti-sublimation pump is installed on the bottom (see figure 3.4(a),(ii)) in order to provide the vacuum in the order of $10^{-10}$ mbar, required in order not to disturb the vacuum conditions in the TSR. On the front side a small manipulator

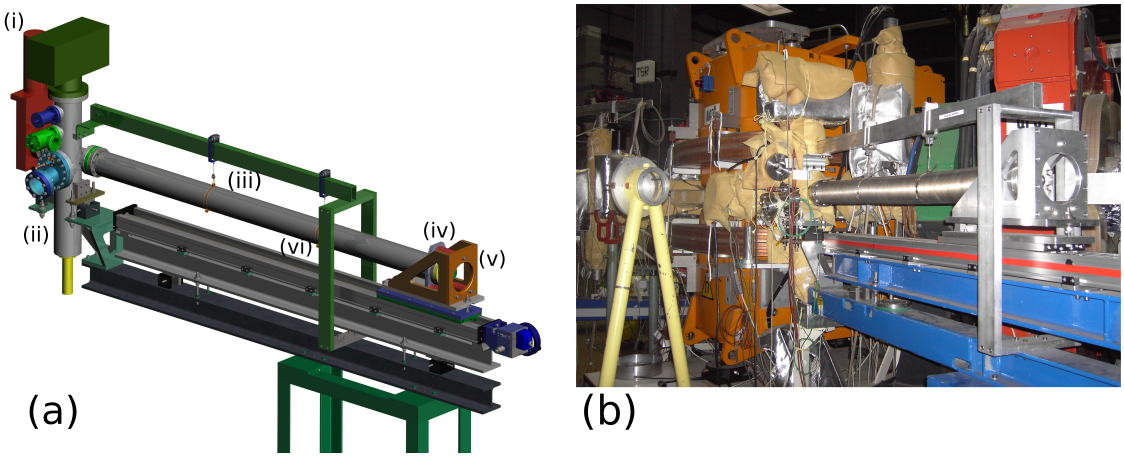


Figure 3.3: *The DEMON detector as a drawing (a) and as a photograph (b). (i) The valve dividing the dipole chamber from the detector, followed by the detector vacuum chamber (see also fig. 3.4) (ii). Following this chamber is the bellow (iii), with the manipulator arm inside (not visible), which is mounted on the back (iv). Both are fixed on the slide on the left (v), which is installed on the translation stage (vi).*

for a titanium cover for the detection system (see section below) is placed, which can be controlled by looking through a vacuum window of the chamber (see figure 3.4(a,v)). An $^{241}$Am $\alpha$ emitter is located inside the chamber (see figure 3.4(b)) to check the functionality of the detection system. The latter consists of the manipulator arm, a hollow pipe mounted on the inner side of a bellow (figure 3.3(iii,iv)). The inner side of the tube is on atmosphere, while the space between bellow and tube is kept under ultra high vacuum. On the front end of the tube the core of the system, the scintillation crystal is located. It is separated from the airside by a welded window. The whole movable setup is installed on a slide (v) thus allowing changes of the horizontal position of the detector. Furthermore the detection system consists of a light guide and a photomultiplier (see figure 3.7). Specific details on the detection of the particles with this setup will be given in the following section.

### 3.2.2 Operating principle of the DEMON detector

Due to the fact that only one negative fragment can be formed in the collision of a molecular ion with the electron beam, the detector for these particles does not require a mass resolution. This allows the usage of a fast scintillating crystal as the first detection stage, as it is also used in the MIDAS-setup [57]. While normally a photomultiplier tube (PMT) is following such a crystal, in the DEMON

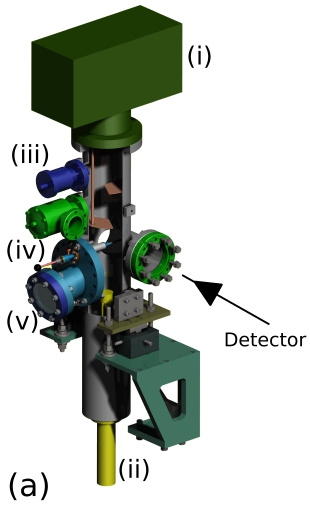



Figure 3.4: *(a) the vacuum chamber, with the ion getter pump (i), the Ti sublimation pump (ii), vacuum gauge (iii), pumping valve (iv), the manipulator for the titanium cover and the vacuum window (v). (b) the $^{241}Am$ $\alpha$ source and the source holder seen through the window (a,v).*

setup a lightguide follows. This is necessary as the detector is operating in the dipole chamber and therefore inside the magnetic field of the dipole. In this field of around 1 T no photomultiplier tube is usable.

### The YAP:Ce scintillating crystal

Detector material studies for the usage in ultra high vacuum [31] led to the decision for the non-hygroscopic Cer-doped Yttrium-Aluminum-Perowskit (YAP:Ce)-crystal, which has a high photon yield, fast decay time (25-30ns) and emits photons at 330 to 380 nm wavelength with a maximum at 350 nm [77]. The crystal is housed in a titanium box (see fig. 3.5) which is open in beam direction and in direction of the photon detection system. The beam-side opening is covered with a 0.75 $\mu$m thick aluminum foil. This foil was forseen to shield stray light. The detector worked well with this setup for the ion pair measurement for $HD^+$ and $H_3^+$. During tests with a $CF^+$ beam, detecting the negative ion pair fragment $F^-$, no clear signature of the charged fragment was visible. Although this fragment with its initial energy of 1.83 MeV deposits an energy of 0.71 MeV on the crystal, only an overall rise of the countrate could be observed. In the pulse height spectrum the $F^-$ peak was not distinguishable from the background. Subsequently, the aluminum foil was removed (for more details on these measurements with and without foil see chapter 3.5).
The crystal holder box itself is mounted on the vacuum side of the detector setup. The scintillation crystal is pressed onto the surface of a UHV-window, which screens the vacuum side from the atmosphere side (see figure 3.6), using a spring to optimize the contact of both in that way, that the light loss due to a slit is mini-

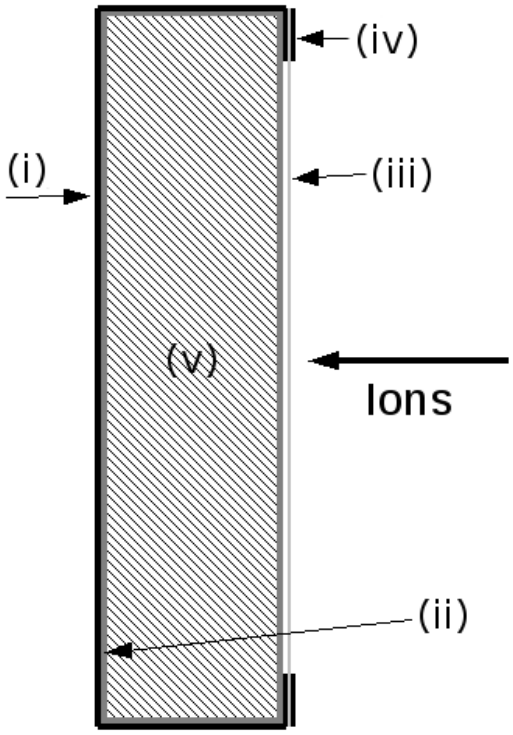


Figure 3.5: *Vertical cut through the crystal holder. It shows (i) the titanium box, (ii) the aluminum coating, (iii) aluminum foil, (iv) titanium frame and (v) the crystal itself. On the right: the flight direction of the ions onto the detection system.*

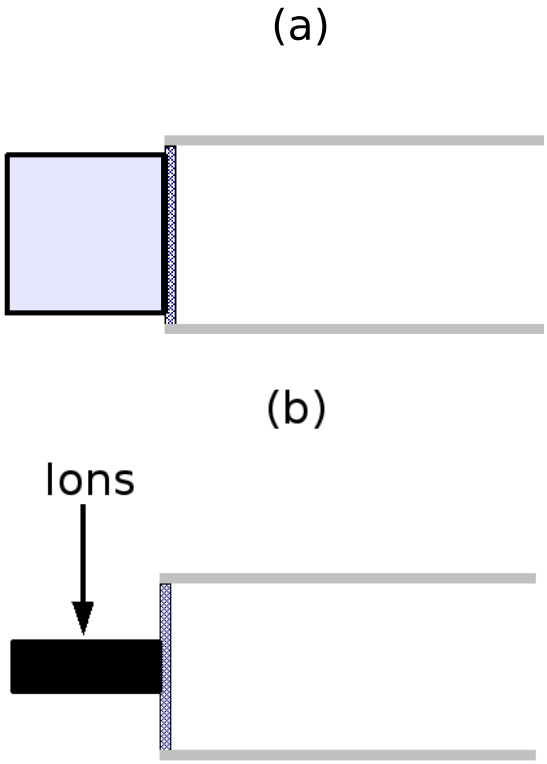


Figure 3.6: *Detector head as used in the setup. (a) Front view; from left to right, the YAP:Ce crystal which is pressed with a spring (not drawn here) onto the screening glass which is welded inside a stainless steel tube. (b) Top view; the arrow indicates the path of the ions.*

mized. The dimensions of the crystal itself are $30 \times 30 \times 10$ mm$^3$. The top and the side-surfaces are polished and coated with aluminum (thickness = $0.1\mu$m) such as to reflect all light to the bottom surface, where it is coupled out. After passing the vacuum window the light enters the light detection system. Two possible readout setups are available for DEMON, which will be discussed in the following.

### Ethylene glycol based liquid lightguide

One possibility to detect the photons emitted by the crystal is a lightguide-photomultiplier setup. Therein the lightguide is a unique design specially adapted to the needs in the DEMON setup. It is based on the principle of total reflection

at the boundary surface of ethylene glycol and teflon. The basic construction was performed in 2002 ([31]). At that time the lightguide consisted of a teflon tube locked on both sides with UV-grade quartz glass cylinders with diameters of 26 mm and lengths of around 50 mm. The glass cylinders were fixed to the teflon tube with specially developed plastic hose clips. Unfortunately the difference in thermal expansion coefficients of the teflon tube and the ethylene glycol were not compensated in this assembly, such that temperature change caused leakage of ethylene glycol. The loss of light guiding liquid resulted in creation of air bubbles which decreased the transmission of the lightguide. In order to compensate the difference in expansion coefficients of liquid and teflon a new design of the lightguide was developed. It is based on the original setup, but encloses the teflon tube in a stainless steel housing, which is equipped with a bellow to compensate the difference in thermal expansion coefficient between liquid and teflon tube. This new housing required an exchange of one of the two glass cylinders with a 20 mm longer one in order to get contact to the vacuum window (see fig. 3.7). On both sides the glass cylinders are fixed by a gasket ring and a screw cap. With this construction it was possible to seal the lightguide. The lightguide is then filled

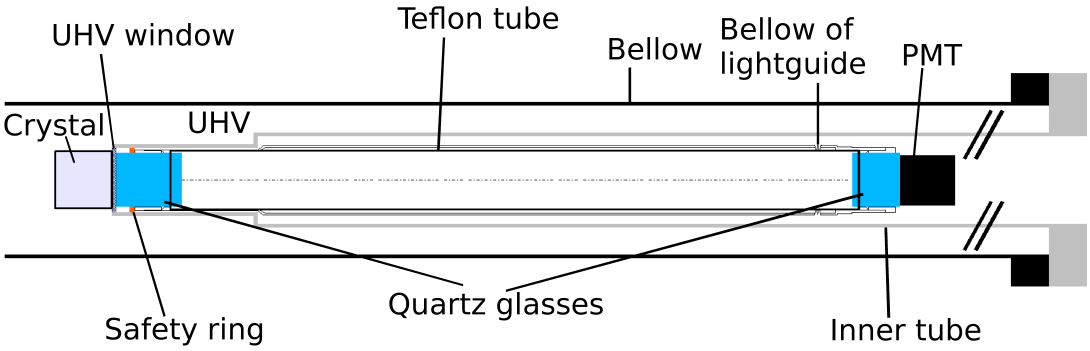


Figure 3.7: *The lightguide setup as used in the DEMON detector assembly.*

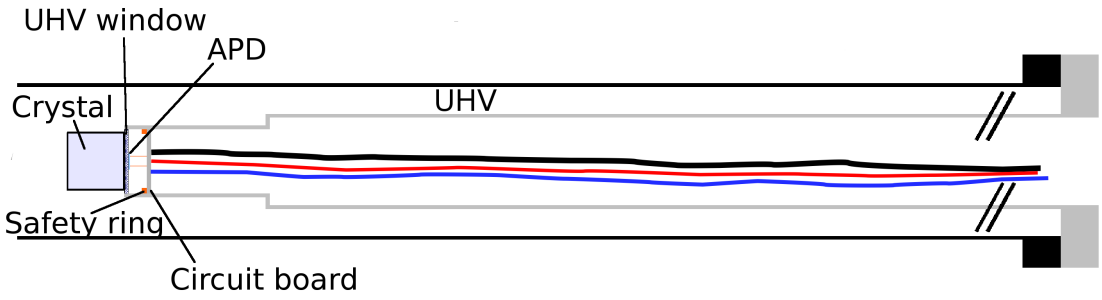


Figure 3.8: *The APD setup as used in the DEMON detector assembly.*

with 10° C cold ethylene glycol, which before filling is kept for 20 min under a pressure of 1 mbar in order to evaporate air still dissolved in the liquid.
On the side with the 70 mm cylinder the scintillation light is coupled in and guided to the opposite side, where it is detected by the photomultiplier tube (PMT; Hamamatsu R7056).

### Avalanche Photodiode (APD)

Using the lightguide setup low energy heavy fragment hits on the detector are difficult to distinguish from the background rate due to the transmission losses of the light intensity. Therefore an Avalanche Photodiode (APD) was tested in order to get rid of the lightguide and achieve a better energy resolution. The diode used was a $5 \cdot 5$ mm$^2$ Silicon APD from Hamamatsu (APD 4829, identical to the S8664 series) with a maximum quantum efficiency at a wavelength of 600 nm and a spectral response range from 320 nm to 1000 nm. The measurement principle is based on the Avalanche effect (impact ionization) which can lead to the Avalanche breakdown of the diodes, a form of electronic current multiplication that allows very large currents to flow within normally insulation materials. This is used as the detection principle, whereas the APD is recovered after an event which causes an avalanche breakdown by a high series resistor in the ns range. In principle one can achieve count rates up to 100 MHz with such a setup. Nevertheless big technical effort has to be applied. This mainly due to the temperature dependent high dark count rate and the changing breakdown voltage. Therefore a very stable temperature and voltage is needed, which would in principle require active cooling of the APD and very stable power supplies. Up to now, the APD was operated by manually controlling the voltages and adjusting them to the temperature changes. In figure 3.9 the APD as it was used at the TSR is shown. The APD is sticking

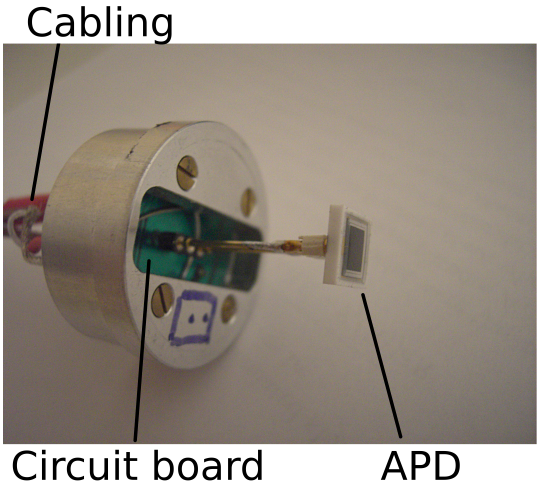


Figure 3.9: *Photograph of the APD setup as used during the test measurements.*

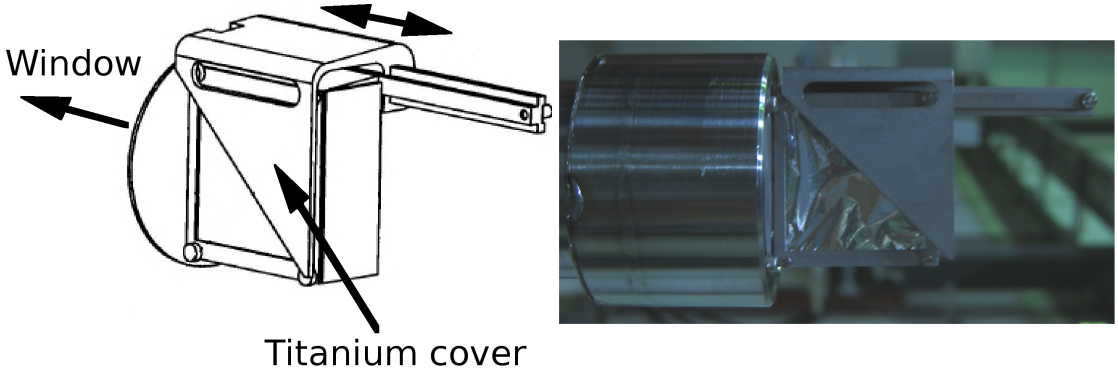


Figure 3.10: *The crystal holder and the movable triangular titanium cover as a drawing and in real as mounted on the front of the detector arm.*

out of the circuit board to get contact to the welded window. This is necessary due to a safety ring (see figure 3.8) in the detector arm, which prevents breaking of the screening window by mismanipulation of the detector.

#### Vertical position of ion pair fragments

While the atomic detector MIDAS can also be moved along the vertical direction to find the optimum detector position (see [57]), this is not possible for DEMON. In order to gain information about the vertical positions of ion impacts on the scintillator and, if necessary, to adjust the ion beam axis, a triangular-shaped titanium cover is movably mounted on the crystal holder box (figure 3.10). With this cover it is possible to obtain information about the vertical position of the negative fragments by scanning the horizontal direction (for details see chapter 3.5). If the beam lies too high or too low in the vertical direction it is possible to correct the vertical beam position with the TSR magnets.

## 3.3 Ionic fragment focussing and steering

As mentioned in the last section, corrections on the closed orbit of the ion beam can be necessary, in order to make the detection of light negative fragments possible. In the next subsection the experimental situation for this case will be explained. The following subsection will give an explanation of possible corrections of the closed orbit.

### 3.3.1 Initial experimental situation

The electron target beam is merged and demerged with the ion beam using two toroidal guiding fields. These fields disturb the ion beam trajectory in the TSR. Because the electron target is mounted in the horizontal plane of the TSR the Lorentz force of the toroid field goes along the vertical direction. This disturbance of the flight path of the initial ion beam can be completely compensated by a pair of vertical correction dipole magnets at the entrance and the exit of the interaction region. These pairs are installed symmetrically on both sides of the interaction region. Thus the ion beam passes the first correction magnet (KDY1), then the second one (KDY2) and then enters the toroid field. This scheme is reversed at the exit. Whereas KDY1 produces a magnetic field in the same direction than

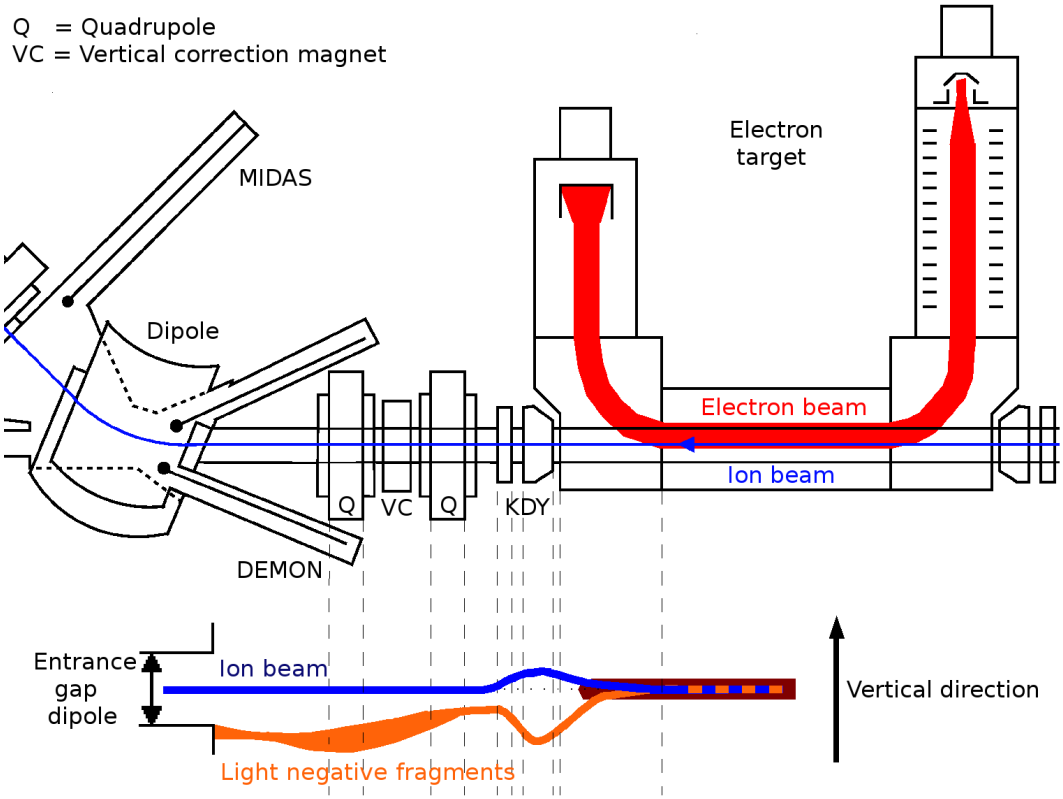


Figure 3.11: *Initial situation for the molecule-electron reaction with a light charged fragments as products. While the correction magnets KDY 1 and KDY2 compensate the deviation of the ion beam (blue), they do not for the light fragments (orange). The fragments are bent to a lower path in the case for negative fragments. Additionally the magnetic field of the focussing quadrupoles are set in a way that the ion beam is well focussed, while the light fragments get overfocussed.*

the toroid, the KDY2 field has opposite direction and overcompensates the toroid field. Careful adjustment of the currents of KDY1 and KDY2 makes it possible to control the ion beam position in the vertical direction and to adjust the ion trajectory to the intended position (see figure 3.11). For molecular ions the beam position is monitored with the 3D imaging system located at the BAMBI beamline. There the neutral DR fragments are detected, giving a projection of the ion beam position in the target section. The monitoring is done during the adjustment using commercial CCD cameras imaging the phosphor screen of this system (see [71; 72]). Calculation of the center-of-mass-distribution of the DR fragments allows fine tuning of the beam axis. An optimal position of the neutrals on the imaging detector automatically leads to an optimal position of the charged fragments on the DEMON detector in the case that the mass ratio of the initial ion and the fragment independent on the charge is larger than one third. As found out empirically, the situation changes dramatically if the mass ratio is equal or smaller than one third. In this case the light fragments are strongly deflected in the toroid at the exit side of the target (see figure 3.11). Therefore they leave the homogeneous field of the following correction magnet KDY2. The next correction magnet which normally bends the ions back to their original path is not able to do this anymore. In contrary, due to its upwards directed force on the ions, the fragments are bent down again. Finally this leads to a very low path. Thus the ions are not able to enter the entrance gap of the dipole chamber (figure 3.11). In order to correct this path, corrections of the ion beam orbit have to be applied,

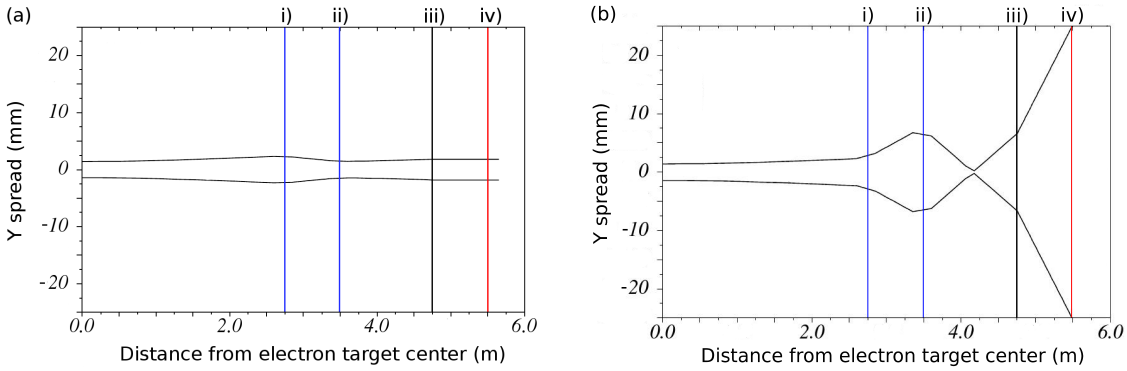


Figure 3.12: *Vertical spread of an $H_3^+$ ion beam (a) and negative ion pair fragment $H^-$ (b) due to the quadrupoles in the dipole chamber (at 5.5m) taking no toroid and KDY fields into account;( (i) and (ii) quadrupoles, (iii) entrance of the dipole chamber and (iv) detection place of the fragments). The situation in (b) equals the one after the closed orbit corrections have been applied, while (a) shows the initial situation. The diameter of the $H^-$ cone is larger than 50 mm at the detection point, therefore only a fraction of the products can hit the scintillator crystal [50].*

which also change the fragment trajectory.
In addition to this strong deflection, the fragment beam spreads due to the TSR's focussing quadrupole magnets. These fields are adjusted in such a way that the spread of the stored ion beam is minimized (see fig. 3.12). For charged fragments these settings of the quadrupoles lead to a spatial dispersion inside the dipole chamber which can exceed the crystal height. In figure 3.12 the situation is shown for the initial beam as well as for light fragments assuming a trajectory initially centered in the beam pipe. In figure 3.11 this effect is schematically included for these low mass molecular charged fragments.
In experiments such as those presented in chapter 4.3 various corrections have been applied in order to gain reasonable results. In the following the closed orbit correction will be presented, while the focussing effect has to be corrected analytically, which will be shortly mentioned in a dedicated chapter.

### 3.3.2 Closed orbit corrections for light-fragment measurements

For imaging as well as for DR rate experiments it is necessary for the ion beam trajectory to be centered in the horizontal and vertical plane. While the horizontal position can be corrected by changing the rigidity of the ring by increasing or decreasing the main dipole field, the vertical position is corrected by the vertical correction magnets. As mentioned earlier, MIDAS is the detector of choice in the case of the charged fragments leaving the dipole field. In this case no changes have to be applied at all, because MIDAS is movable in horizontal and vertical directions. For DEMON it depends on the mass of the fragment whether corrections have to be applied or not. Assuming a beam well adjusted in that way that the neutral fragments are centered in the BAMBI beamline, no corrections have to be done if the mass of the fragments is greater than one third of the initial ion mass, whereas for the lighter masses corrections have to be applied as has been found out empirically. This can be done in two ways: by a vertical shift of the ion beam trajectory or by introduction of an angle in vertical direction.
The vertical shift will be applied in the sections following the correction magnets KDY. Thereby four vertical correction dipoles are needed. Each of them is located in between the quadrupole pairs in front of and after a main bending dipole magnet pair. Thus the correction magnets affect the orbit from after the electron target until the injection section, where the beam is bent back onto its original orbit. This calculation of this orbit correction is shown in figure 3.13 [50]. As can be seen the ion beam is bent upwards by the first correction magnet in front of the detection chamber inside the dipole field. In the straight section following the dipole pair the first vertical correction magnets are used in order to bend the

beam to a path parallel to the original orbit, while the second is used to bend the beam downwards to this orbit. To bring the ions back to their original orbit, the correction magnet following the second dipole pair is needed. The ion beam is then kept untouched until the ions again reach the exit of the second KDY pair. The correction has to be done carefully, checking the storing and cooling properties after each change. Once an optimal setting for beam storing and cooling as well as fragment detecting is found, the settings are kept constant over the whole experimental period.
Another way to allow the detection of light charged fragments is the introduction of an ion beam inclination in vertical direction. In this case a sinusoidal change is applied (see figure 3.13). Therefore the same correction magnets can be used as discussed before, with the difference that the second and third correction magnets do not bend the ion beam onto a path parallel to its original orbit. In this case the second correction dipole bends the beam back in the opposite direction, such that the ions cross the vertical coordinate of their original orbit. The last correction magnet then bends the beam back onto its initial orbit. The same care about preservation of storing and cooling properties of the TSR has to be applied than for the vertical shift. Likewise the settings are kept constant during the experiments.
As it turned out during the ion pair measurement of $H_3^+$, an additional angle in the electron target region provided by the KDY increases the detection efficiency (see chapter 4). In this case the electron beam trajectory of the electron target was changed by modifying the target's guiding field.

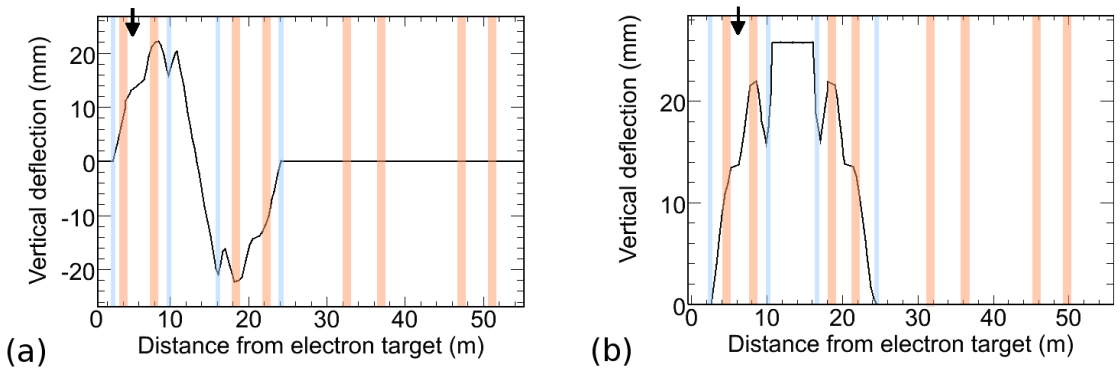


Figure 3.13: *Calculations of the vertically corrected orbit of the ion beam. In this case the manipulation of the closed orbit by the correction dipoles (light blue) are applied after the electron target (0 m). In light orange the position of the storage ring deflecting magnets; (a) shows as a correction by application of an angle, while (b) shows the vertical shifting method. The arrow indicates the detector position.*

## 3.4 Data acquisition setup

Settings like the cooler setup or the magnetic fields of the target are kept static during molecular experiments. These settings are controlled via the MPI-EUNet system, which consists of several remote slave units with digital and remote I/O connected to a networking master by serial wires or optical fibers. Each slave houses multiple digital analog in- and outputs. For controlling all the parameters of the EUNet a unified client-interface (HSI-Pult) is used. the data acquisition system (mileDAQ, [57]) is used decoupled from this interface. It controls all the needed experimental parameters which are not necessarily fixed, like injection times for the TSR or the variation of the electron beam energy, and reads out all the involved instruments, e.g. the detector counts.

### 3.4.1 Detection system electronics

Before starting a rate measurement the DEMON and MIDAS detectors are tested and set up using $^{241}$Am $\alpha$-sources, which are located in the vacuum chambers of each setup (e.g. see fig. 3.4). While the detection system of MIDAS is described elsewhere [57], the system of DEMON will be described here in more detail. It consists of the hardware for the signal convolution, as well as of the controlling and signal counting VME computer unit.
The light pulses from the crystal of the DEMON setup are detected by a photomultiplier tube whose signals are directed to a preamplifier. The output of this amplifier is then directed to a spectroscopic amplifier (SA), where the ingoing signal is filtered and whose outgoing signal is split. On one hand the latter is inserted into a delay amplifier. The amplified signal is fed into a 16 bit peak sensing ADC. The latter is gated by a single channel analyzer (SCA) which ensures that the signal amplitude lies within a certain intended window and thus allows background suppression. A second logic output of the SCA is connected to a 250 MHz 32-channel multiscaler, where also the electron currents and voltages of cooler and target, the BPM rate, the DC signal, the normalization countrate from the MIDAS detector, and timing information from an external clock are recorded. The scaler, the ADC, but also the digital I/O are controlled by a VME computer system which is installed as a DAQ frontend [57].

### 3.4.2 Measurement scheme

For all molecular recombination measurements at the TSR the following scheme has been established. Depending on the needs of the specific measurement the electron gun potential of the target is set to a start value, followed by the request for an ion beam injection by sending a TTL signal from the VME front-end to

the ring control. After the injection is done a confirmation signal from the ring control is read back, which starts the measurement cycle. This cycle consists of a precooling step and a "wobble" scheme which contains a cooling, a reference and a measurement step, where each step can have different duration and repetition rates:

- the "precooling step" gives the electron cooler and/or the electron target some time for intrinsic and phase space cooling of the ion beam. Normally the electron cooler is kept for the entire measurement at cooling energy, thus setting the electron target to the cooling condition might not be necessary. This means, the target can in some situations assist the cooler and help to reduce the total cooling time.

- during the "cooling step" the electron target is set to cooling energy for interstage cooling if the cooling energies are matching.

- the rate measured in the "reference step" is either taken for normalization or background substraction (rest gas DE) of the rate of the measurement step. The energy is mostly chosen in such a way that the expected electron induced rate at this energy is low or zero (for more details see chapter 4 and 5). The energy is like at the cooling step kept constant throughout all measurement cycles included in one run. In special experimental situations several such reference measurements can be included in the "wobble"-scheme.

- The energy in the "measurement step" is varied from measurement cycle to measurement cycle and the measured rate in this step is background subtracted, normalized and corrections are applied to the energy and the rate itself (see chapter 3.4.3). As a result one gains the rate according to equation 2.20, where the information of the ion current is taken from the cooling or reference step (fore more details see chapter 4 and 5).

While the precooling step has a typical duration of a few seconds, each step of the wobble cycle is of only a few ms. After each voltage jump the data acquisition waits for 5 ms to allow the HV-power supply to reach its setpoint. The voltages, the repetition rate and the durations of the steps are given by the experimenter in a configuration file, which is imported into the measurement control program mileDAQ (for more details see [57]). The data-acquisition (DAQ) software sweeps through all scaler and ADC channels and writes the data to a raw file.
The scheme used in the described way has the advantage of not being limited by the ion beam lifetime but has the disadvantage that long-term variations of the restgas pressure due to the different measurement energies lead to variations of the beam lifetime and the background rate, depending on the position of the energy

scan. This is caused by the fact that for each position of an energy scan an new injection has to be done. This kind of measurement procedure can take several hours for a given energy interval.

### 3.4.3 General data processing procedure

The raw data are transformed into histogram files by mainly using two programs. The first one was used for the experiments on $HD^+$ and $H_3^+$ measurements (see chapter 4), while the second was used for the $HF^+$ raw data (chapter 5). Former is called md2h.c, which transforms to so called hbook files usable with the PAW analysis framework [65]. This files were used in the online control of the experiment, while for the offline analysis these files were further converted to the data format of ROOT [66] which is the dedicated new data analysis framework for all measurements done at the TSR. In the $HF^+$ experiments a new macro called md2root.c [60] was used, directly creating ROOT files. In the following the major steps for the offline analysis of all measurements will be presented. Specific details of each measurement will be laid out in a dedicated chapter.

#### Count rate recording

For all measurements in the present work pulse hight spectra of molecular fragment induced detector events are taken. In order to gain the detector countrate out of this data, a window in a certain range of the ADC spectrum was chosen and the spectrum was integrated in these bounderies. This gives the countrate for each step and energy. These raw counts are not normalized to the total measuring time at this point.

#### Normalization with respect of time

For each step the duration of the measurement is sent to the scaler by using a 10 MHz clock, whose pulses are counted during the data acquisition. The raw detector counts of DEMON are then divided by the time which was spent at each step. In order to gain a rough estimation of the measured rate during the measurement in the "online" analysis software this raw spectrum is divided to the MIDAS rate at cooling energy as it is shown eg. in fig. 4.1.

#### Normalization with respect of the ion current

In the first step after time normalization in the offline analysis the DEMON count rate has to be normalized to the ion current. This is normally done by transforming

the measured time normalized rate of MIDAS to an ion current equivalent (for more details see section 4). This leads to an ion current normalized rate

$$R_{ion}(E) = \frac{R_{\mathrm{DEMON}}(E)}{I_{ion}(R_{\mathrm{MIDAS}})}\frac{L}{l} \tag{3.4}$$

with the rate $R_{\mathrm{DEMON}}$ from DEMON, $R_{\mathrm{MIDAS}}$ from MIDAS and the length ratio $L/l$ of the whole circumference and the overlap of ion and electron beam. Normalization of this rate by the electron density $n_e$ results in the rate coefficient $\alpha(E)$.

### Normalization to the electron density

The electron density is calculated according to

$$n_e = \frac{I_e}{e\xi\pi r_{cath}^2\beta\gamma} \tag{3.5}$$

with the radius $r_{cath}$ of the thermionic cathode being $r_{tc} = 0.8$ mm (used for the experiments presented in chapter 4) or, for the photocathode $r_{pc} = 1.5$ mm. $\xi$ is the expansion, $\gamma = (E_{rel} + E_{0,e})/E_{0,e}$, where $E_{rel}$ is defined as the relative energy with respect to the cooling energy $E_{0,e}$, $\beta = \sqrt{1 - 1/\gamma^2}$, $\gamma$ the Lorenz factor and $I_e$ the electron current. The electron current was measured using a current to frequency converter and recorded using the scaler. The rate coefficient $\alpha$ is computed in dependence of the electron impact energy in the laboratory frame by

$$\alpha(E) = \frac{R_{ion}(E)}{n_e} \tag{3.6}$$

### Transformation into the center-of-mass-frame

The conversion of the lab-energy frame to the center-of-mass frame needs precise knowledge of the ion beam energy and therefore for the space charge corrected cooling energy of the electron target. This is obtained by doing an energy scan around the expected cooling energy in the lab frame. The cooling energy was then found by mapping the rate structures found at negative and positive relative velocities respectively. After this step as a further correction the influence of the electron target toroids has to be taken into account.

### Toroid effect correction

In the merging and demerging sections of the electron and the ion beam, their is a non-vanishing angle between $\overrightarrow{v_e}$ and $\overrightarrow{v_i}$. This results in a relative velocity

vector $\overrightarrow{v_d}$ different from that in the collinear interaction region. This results in an effectively increased collision energy. This effect can be corrected if a map of the magnetic field is used [26] together with a deconvolution method, which is described by Lampert et al [2].

### Cross section

The cross section is finally derived by a simple division of the rate coefficient with the corresponding relative velocity $v_d(E)$ for each measured point. This is valid as long as the energy at which the cross section is calculated is greater than the electron temperature $k_B T_\perp$. One obtains

$$\sigma_{exp}(E) = \frac{\alpha_{exp}(E)}{v_d(E)} \ . \tag{3.7}$$

## 3.5 Systems studied in the present work

Different systems were studied in the present work, whose preparatory test measurements will be presented in this chapter. These tests were used in order to gain information about detection efficiency and energy resolution of the two possible light detection systems for the photons emitted by the YAP:Ce scintillation crystal as well as about fragment beam positions on the detectors in the various experiments.

### Electron-ion collisions of $HD^+$

In the case of $HD^+$ two ion pair fragmentation channels are possible:

$$HD^+ + e^- \rightarrow HD^{**} \rightarrow \left\{ \begin{array}{l} D^- + H^+ \\ H^- + D^+ \end{array} \right\} (E > 1.913 \text{ eV}) \tag{3.8}$$

Both channels are energetically accessible at a threshold collision energy of 1.913 eV. In figure 3.14 the cross section for both channels measured at CRYRING is shown.

### Electron-ion collisions of $H_3^+$

In the collision experiments of $H_3^+$ two ion pair channels are energetically possible. One is accessible at 5.4 eV, while the second opens at 8.1 eV:

$$H_3^+ + e^- \rightarrow H_3^{**} \rightarrow \left\{ \begin{array}{ll} H^- + H_2^+ & (E > 5.4\, eV) \\ H^- + H^+ + H & (E > 8.1\, eV) \end{array} \right. \tag{3.9}$$

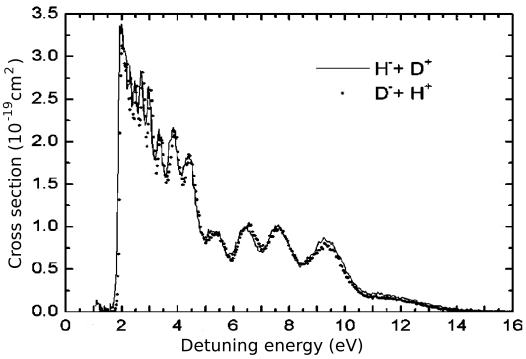


Figure 3.14: *The ion pair formation cross section of both channels of $HD^+$; measured at CRYRING [3].*

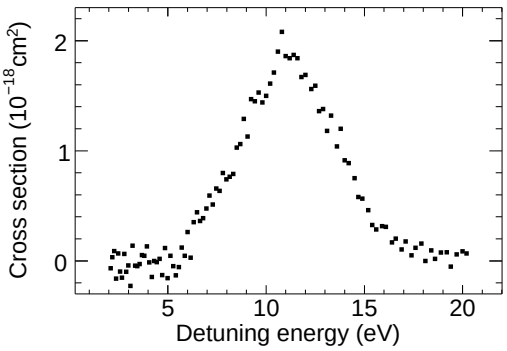


Figure 3.15: *The ion pair formation cross section of $H_3^+$; measured at CRYRING [54].*

The cross section of the total $H^-$ fragments for both channels measured at CRYRING is shown in figure 3.15.

### Electron-ion collisions of $HF^+$

In the case of $HF^+$ direct and indirect ion pair formation are possible leading to the following reaction paths

$$HF^+(v=0) + e^- \rightarrow HF^{**} \rightarrow H^+ + F^- \quad (3.10)$$

$$HF^+(v=0) + e^- \rightarrow HF_{nv}^{Ryd} \rightarrow HF^{**} \rightarrow H^+ + F^- \quad (3.11)$$

An energetic threshold is predicted at 17 meV, but due to rotational excitation of about 25 meV at room temperature and the limited energy resolution, it is not observable in the storage ring technique up to now.

## 3.5.1 Ion beam conditions

Table 3.2 gives an overview of the basic conditions for the above mentioned ion-electron collision studies. They will be presented in detail in chapters 4 and 5, but the preparatory test measurements will be presented here, including the tests with the $\alpha$ source. The experiments with the di- and triatomic hydrogen ions as well as the $\alpha$ particle measurement were performed with the stray light protective aluminum foil in front of the crystal, while the APD test as well as the ion pair formation of the hydrogen fluoride ion and another test with the $\alpha$ source were performed without this foil. As mentioned earlier, the foil was removed due to the unsatisfactory results in a test using $CF^+$.

| Ion | $E_{ion}$ (MeV) | $E_e$ (keV) | $n_e$ ($10^6\,cm^{-3}$) | Cooler used | Cooling time (s) | Ion source and gas | Detected fragment and energy deposited energy on crystal |
|---|---|---|---|---|---|---|---|
| $HD^+$ | 5.19 | 0.944 | 22.9 | yes | 1 | CHORDIS $H_2$ & $D_2$ | $D^-$ ($E_{D^-}$ = 3.46 MeV) 3.43 MeV |
| $H_3^+$ | 5.19 | 0.944 | 22.9 | yes | 1 | CHORDIS $H_2$ | $H^-$ ($E_{H^-}$ = 1.73 MeV) 1.7 MeV |
| $HF^+$(A) | 4.66 | 0.127 | 3.3 | no | 5 | Penning $CHF_3$ | $F^-$ ($E_{F^-}$ = 4.43 MeV) 4.43 MeV (no foil!) |
| $\alpha$ source | | | | | | | $\alpha$ particle ($E\alpha$ = 5.46 MeV) 5.33 MeV |

Table 3.2: Settings as used for the experiments presented in chapters 4 and 5. Listed are the ion beam energy ($E_{ion}$), the electron energy at cooling ($E_e$), the electron density ($n_e$), whether the cooler was used or not, the cooling time and the used gases in the desired ion source for the experiments presented in this thesis.

The test measurements start in principle with the determination of the fragment beam position using the scan procedure with and without the triangular cover as mentioned in chapter 3.2.2. Once the detector is placed in the right position and any necessary beam corrections have been applied as described in chapter 3.3, pulse height spectra are taken in order to get a feeling of the detector performance for the respective ionic fragment or $\alpha$ particle. In the following the determination of the detector position will be presented followed by the test measurements of the pulse height spectra. Latter is split into two parts: the first covers the measurement with the foil and only the lightguide setup, while the second part includes also the APD, but with the aluminum foil removed, since only for this measurements the diode setup was available.

### 3.5.2 Determination of the negative ionic fragments position on the YAP:Ce crystal

As mentioned above the DEMON detector is not movable in vertical direction. To obtain the vertical fragment beam position on the crystal and apply ion beam orbit corrections if needed, the detector head is equipped with a triangular metal plate (see also chapter 3.2). Using this triangle in front of the crystal it is possible to roughly obtain the vertical position of the fragments on the crystal. The working principle is as follows: while the detector is moved horizontally through the dipole chamber the countrate is recorded. Without the triangular cover, this countrate depends on the horizontal detector position only. Over the whole range corresponding to the crystal width fragment hits are measureable (see figure 3.16). This picture changes with the cover. The spread $w$ in horizontal detector position of the countrate now depends on the vertical position $y$ of the fragment beam:

$$y = h - w \tag{3.12}$$

with $h$ being the height of the sensitive detector area. According to this approximate formula the width of the count rate peak is linearly depending on the vertical position of the fragment beam. A narrower countrate peak with respect to a horizontal detector scan indicates a higher position of the fragments hitting the crystal (see figure 3.16). This information of the vertical position as well as the expected fragment beam spread are combined in order to decide whether the orbit of the ion beam has to be changed in the experiments.
During the experiments and tests first the fragment position was roughly determined, followed by a fine scan around the detected point with and without the triangle. The comparison of both results and the theoretical beam height assignment following equation 3.12, showed in the case of the $HD^+$ ion beam (see figure 3.17) that the fragments of the ion pair formation $D^-$ are hitting the crystal at its

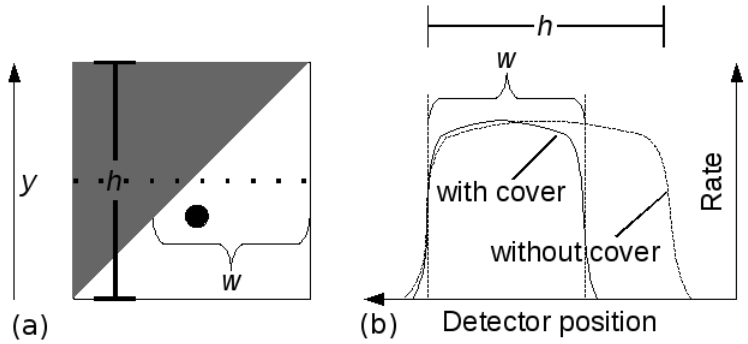


Figure 3.16: *Schematical drawing of the horizontal positions scan using the triangular cover. (a) shows the crystal covered with the triangle; (b) shows the resulting countrate distribution vs. the horizontal detector position.*

lower edge, while the $H^-$ fragments from the IPF of $H_3^+$ are hitting the crystal in its middle (see figure 3.5.2). The $F^-$ fragments were hitting the crystal relatively low (see figure 3.5.2). For all three experiments no change was applied to the beam orbit. In the case of $D^-$ and $F^-$ fragments the position of the fragments were acceptable, as their beam spreads were very narrow [50]. In the case of the $H^-$ no more changes besides the correction mentioned in chapter 3.3 were needed. For completeness the results of the position scan using the $\alpha$ source inside the detector vacuum chamber is shown in figure 3.20. The FWHM is broader than the crystal width (see chapter 3.2) which is due to the uncollimated $\alpha$ particles. The maximum of this peak is the countrate taken directly in front of the crystal. Conventionally this position is taken as the origin of spaces of the detector setup.

### 3.5.3 Test measurement with the lightguide setup

**Test measurements using a $HD^+$ ion beam.** The ion pair formation of $HD^+$ leading to the negative $D^-$ fragment have an energetic threshold. Only above this energy electron induced negative fragments are possible (for more details see chapter 4). Therefore pulse height spectra were measured at an energy below and above this threshold subsequently ("threshold method"). The $D^-$ fragment must have an energy of 3.46 MeV (two thirds of the total energy of 5.19 MeV), which will be deposited nearly without any losses on the crystal (see table 3.2). In figure 3.21 these two measurements are plotted in one graph. The red curve for energies above the threshold shows a clear signature of the electron induced $D^-$ fragment. Additionally a peak at lower energies occurs which is also reproduced in the background measurement for energies below the threshold (black curve). This peak is exactly at half of the energy of the $D^-$ peak, which leads to the presumption that

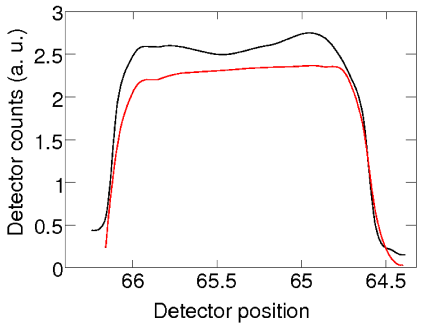


Figure 3.17: *Horizontal position scan with (red) and without (black) cover using the $HD^+$ ion pair formation leading to $D^-$.*

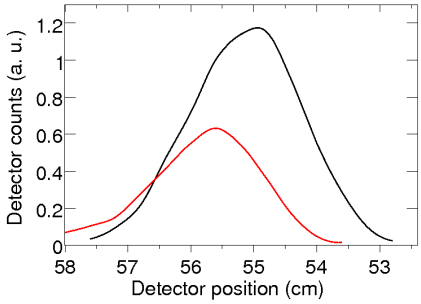


Figure 3.18: *Horizontal position scan with (red) and without (black) cover using the $H_3^+$ ion pair formation leading to $H^-$.*

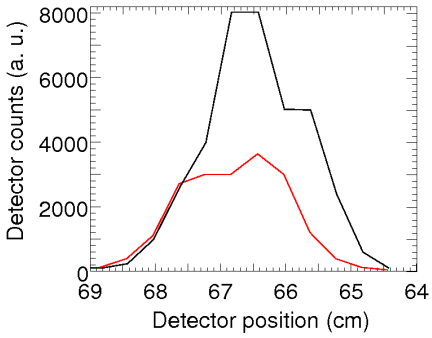


Figure 3.19: *Horizontal position scan with (red) and without (black) cover using the $HF^+$ ion pair formation leading to $F^-$.*

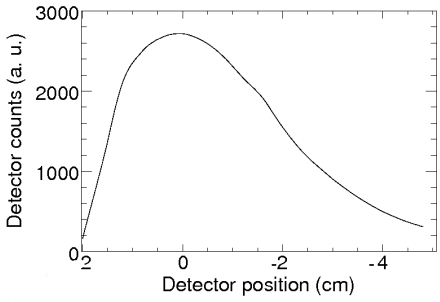


Figure 3.20: *Horizontal position scan without cover using the $\alpha$ source.*

this peak is caused by hydrogen atoms. These fragments are caused by residual gas dissociative excitation. Thereby the emerging neutral hydrogen atoms cover the whole solid angle and can hit the crystal. For the same reason the tail of the background peak can be explained by neutral D atoms from the rest gas DE. For the data analysis of the ion pair formation the ADC spectrum was cut at the ADC values of 1800 and 3200. The area in between (see figure 3.21) was integrated to give the total signal countrate. The background countrate was checked several times during the experiment and was constant over all runs (see also chapter 4).

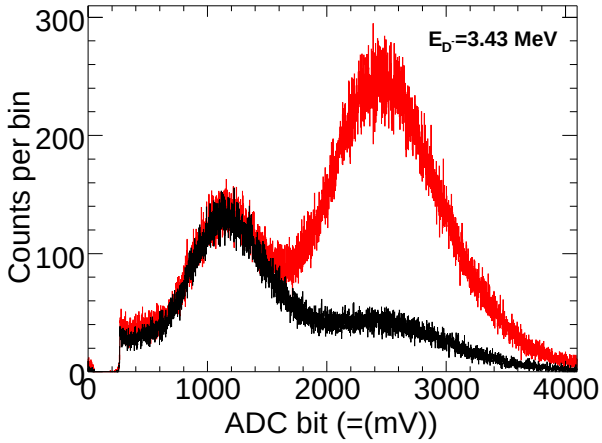


Figure 3.21: *ADC spectrum of the $D^-$ fragment (3.43 MeV energy deposition on crystal) of the $HD^+$ ion pair formation. Black curve: background measurement ($E_e$ = 0 eV); red curve: electron induced signal ($E_e$ = 3eV).*

**Test measurements using an $H_3^+$ ion beam.** The ion pair formation produces $H^-$ fragments, which are used in order to perform the measurement of the pulse height distribution. The same principle of probing below and above the ion pair threshold was used (for more details about the ion pair formation of $H_3^+$ see chapter 4.3). The detected $H^-$ fragments initially have one-third of the total ion energy of 5.19 MeV. This corresponds to an energy of 1.73 MeV, which will almost completely be deposited on the crystal (see table 3.2). In figure 3.22 the results of these measurements are presented. In this case the background measurement were taken with an electron-ion energy of 0.7 eV, whereas the electron induced fragments were detected at an energy of 11 eV. For the same reason as discussed in the previous paragraph the background contains a peak produced by neutral hydrogen atoms. Due to the fact that neutrals as well as charged fragments have the same energy, the electron induced peak lies on top of the background peak (red curve). Therefore the integral of the whole peak were taken in order to get the count- and background-rate. Also here the background was checked several times during the experiment and was found to be constant as well. Taking the vertical fragment beam spread for these light fragments into account (figure 3.12), it is clear that the pulse height spectra shown here cannot include all negative

fragments. The derived rate had to be scaled to a known rate (included in the results presented in chapter 4.3) and absolute rate measurements were therefore not possible.

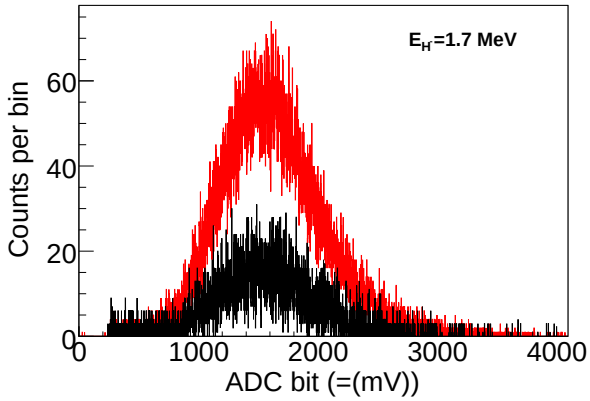


Figure 3.22: *ADC spectrum of the $H^-$ fragment (1.7 MeV energy deposition on crystal) of the $H_3^+$ ion pair formation measurements. Black curve: background measurement ($E_e$ = 0.7 eV); red curve: electron induced signal ($E_e$ = 11 eV).*

**Test measurement using the $^{241}$Am $\alpha$ source.** In this case the $\alpha$ source inside the detector vacuum chamber was used to gain information of the performance of the detector setup. The alpha source emits particles at two different energies (5.442 and 5.485 MeV [15]), which are so close to each other that they are not resolvable by DEMON and were therefore treated as one line. A clearly resolved peak was observed which was caused by the $\alpha$ particle (red curve in figure 3.23). The black curve shows the background where the detector was put to a position far away from the source. This red curve will later be compared to the measurements done without the aluminum foil. However, the energy resolution of 44% FWHM is a factor of three worse compared to MIDAS, which uses the same source and crystal [57]. This is caused by the transmission of the lightguide of around 75% [31] which smears out the light intensity distribution of the crystal and leads to a corresponding smear-out of the distribution of the deposited energy of the particles on the crystal.

### 3.5.4 Comparison of the lightguide and the APD setup

Due to unsatisfactory results during the $CF^+$ measurement the stray light protective aluminum foil was removed and the performance of the detector was tested using the $\alpha$ source as well as during the ion pair measurement of $HF^+$ (see chapter 5). Additionally the then available APD was tested, which was considered as a possible replacement of the lightguide setup, in order to avoid transmission losses which worsen the energy resolution of DEMON.

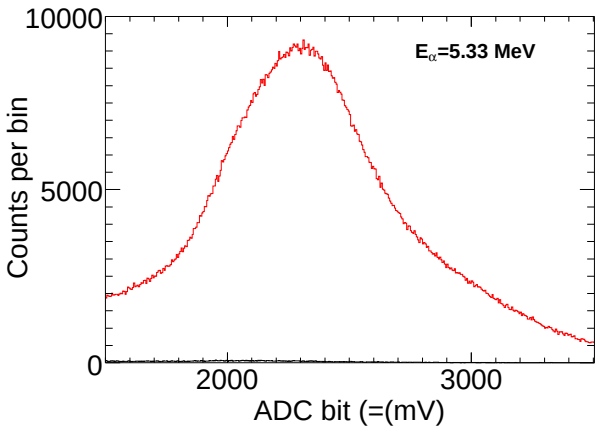


Figure 3.23: *Test measurements for the lightguide setup and foil with the $^{241}Am$ source. black: background; red: with $\alpha$ irradiation.*

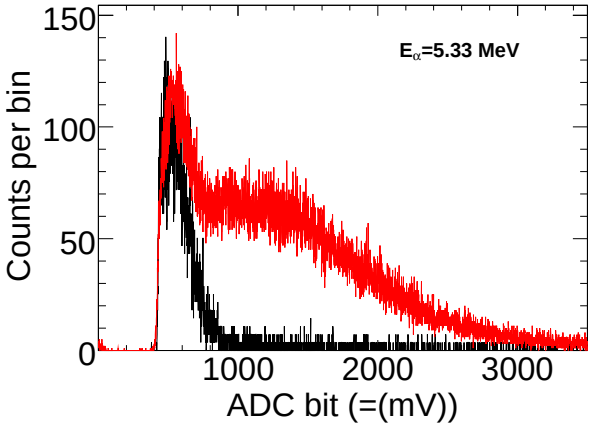


Figure 3.24: *Test measurements for the lightguide setup and without foil with the $^{241}Am$ source. black: background; red: with $\alpha$ irradiation.*

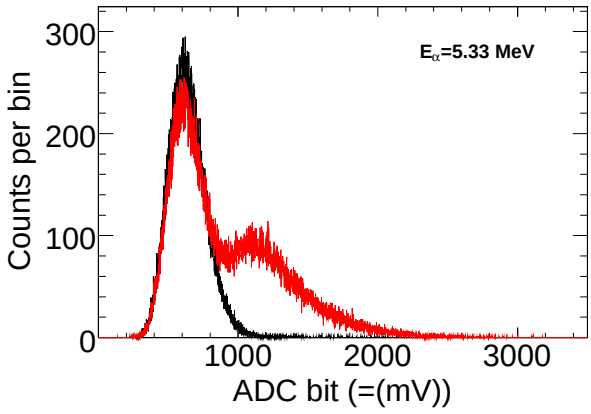


Figure 3.25: *Test measurements for the APD setup and without foil with the $^{241}Am$ source. black: background; red: with $\alpha$ irradiation.*

**Test measurement using the $^{241}$Am $\alpha$ source** The results of these test measurements are shown in figure 3.24 for the lightguide setup, and in figure 3.25 for the APD setup. Therein the black curves show the background measurements, while the red ones show the pulse height distribution in front of the $\alpha$ source. Comparison of the two lightguide measurements (figure 3.23 and 3.24) shows that the resolution worsens due to the missing foil, which indicates high stray light input on the crystal. Therefore the $\alpha$ particels could not be completely separated from the background, although a clear difference of background and particles can be seen. Thus the energy resolution worsens to 100% FWHM. The APD instead shows a better resolution (50% FWHM) compared to the lightguide setup in the measurement without the foil. Nevertheless also with the diode the events caused by the $\alpha$-particles are not completely separable from the background. The resolution is comparable to that of the lightguide setup. Development of the hardware needed for APD operation of DEMON has thus been stopped as the diode seems not to provide the advantages that were hoped for. This is mainly due to the small detection area in comparison to the lightguide setup. To prove this, both setups were tested using an $HF^+$ ion beam, were the $F^-$ was detected (see chapter 5).

**Test measurements using an $HF^+$ ion beam** Both light detection setups were tested using an $HF^+$ ion beam. Therefore the $F^-$ ion of energy 4.4 MeV was detected and pulse height spectra were recorded. In contrast to the $HD^+$ and $H_3^+$ measurements, no threshold energy is expected for this ion pair formation. Therefore the background was measured by blocking the ion beam in the TSR's injection line so that no $HF^+$ ions were travelling along the closed orbit of the TSR. The results of these measurements can be seen in figure 3.26. While with the lightguide setup a difference between data without ions (black curve) and with ions (red curve) can be seen, no difference is observable with the APD setup. A possible explanation could be that the magnetic fields of the dipole influence the electronics of the APD which is located directly behind the diode in the detector head, while the lightguide is not influenced by magnetic fields. Up to now the APD setup does not gain any advantage that would justify further development of this technique. That said, the diode has not been tested with the aluminum foil so far.

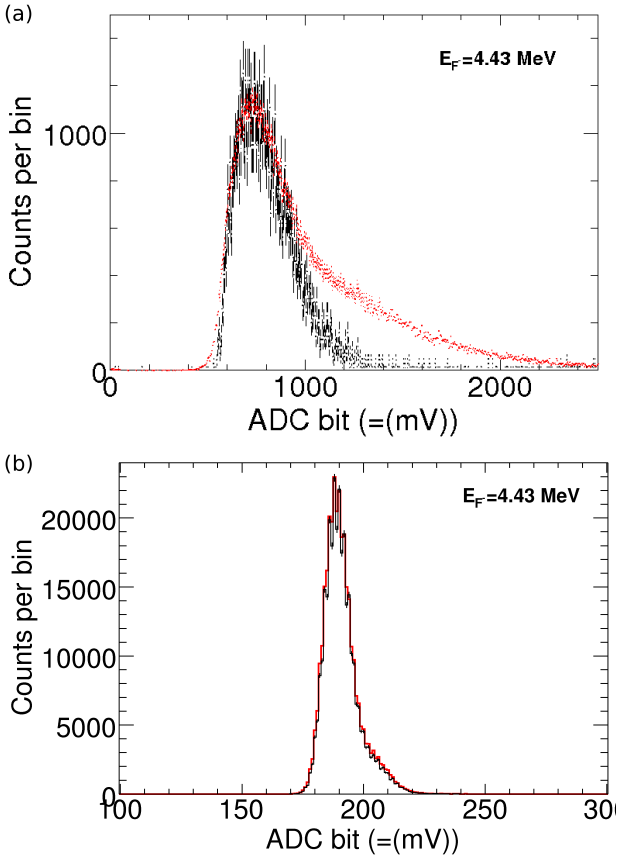


Figure 3.26: *Comparison of the lightguide and APD setup in a "real-life" experimental run. For the lightguide setup (a) a clear difference between the data with (red) and without (black) ion beam can be observed while in the APD setup (b) no difference can be seen at all. The data were taken using a $HF^+$ ion beam during the ion pair experiment described in chapter 5.*

# Chapter 4

# Ion pair formation of di- and triatomic hydrogen ions

Molecules and molecular ions play an important role in various environments, such as the interstellar medium, the atmosphere and in industrial plasmas used for instance for the etching processes (cf [78]). Their formation and destruction processes influence the reaction chains and thus the composition in these media. Therefore, theoretical models describing the behavior of a plasma require good knowledge of the various mechanisms involved.
Especially in the interstellar medium, $H_2$ and its corresponding ion $H_2^+$ play a major role. For instance, a collision between both molecules can cause the formation of the $H_3^+$ molecule through the reaction

$$H_2^+ + H_2 \rightarrow H_3^+ + H \tag{4.1}$$

$H_3^+$ itself is a key molecule in subsequent reactions towards the formation of more complex polyatomics in the interstellar medium and has therefore motivated numerous experimental studies (e.g. [13; 38]).
Meanwhile $H_2^+$ and $HD^+$ have reached the status of benchmark molecules both in theory and experiment. Latter molecule is often preferred in experiments, where thanks to its permanent dipole moment it can cool through radiative emission. Consequently molecules with initial states in equilibrium with the background radiation are provided, simplifying the comparison to theory and among experimental results. From the theoretical point of view the diatomic hydrogen molecules are the only ones, where present models achieve high accuracy.
$H_3^+$ is the simplest polyatomic molecule and therefore it is apart from its key role in the interstellar medium a preferred candidate for testing theoretical predictions on the interacting polyatomic molecules with atomic and molecular species, electrons or even photons (cf [12; 19; 37]). Consequently the triatomic hydrogen has

attracted the attention of physicists for many decades, but still its reaction processes are known only to an unsatisfactory degree.
For both molecules the most important loss process in interstellar clouds is dissociative recombination. Here the special case of ion pair formation will be focussed and discussed in the following in more detail. Therefore the chapter is organized as follows: in the first part the experiment on $HD^+$ will be described, followed by a comparison to previous CRYRING experiments and theoretical calculations. Based on the experimental results is the subsequently following chapter on the Fast Fourier Transformation (FFT) technique and its application on the $HD^+$ data. The chapter is finalized by the basics and results on the $H_3^+$ ion pair formation, also compared to previous CRYRING results and theory.

## 4.1 Ion pair formation of $HD^+$

The ion pair formation of $HD^+$ is initiated similarly as the DR process by the capture of a free electron. However, propagation of the neutral intermediate compound state along the repulsive curve leads to the dissociation into charged fragments:

$$HD^+ + e^- \rightarrow HD^{**} \rightarrow \left\{ \begin{array}{l} D^- + H^+ \\ H^- + D^+ \end{array} \right\} (E > 1.913 \text{ eV}) \tag{4.2}$$

This reaction channel requires a threshold energy of 1.913 eV considering both the dissociation limit of the ion leading to a positive and a neutral fragment at 2.668 eV [59] and the electron affinity of the hydrogen atom (0.755 eV [59]). In the following details of the measurement procedure on the ion pair formation of $HD^+$ at the TSR will be given first, before the data will be presented and discussed in view of previous measurements and theoretical predictions.

### 4.1.1 Ion pair measurement at the heavy ion storage ring TSR

The ions for the ion pair measurement of $HD^+$ were produced by the CHORDIS ion source. The ion beam was accelerated by the High Current Injector (HCI) and the post accelerator to an energy of 5.19 MeV, then injected into the Test Storage Ring (TSR) and stored on a closed orbit. Two electron beams are merged independently with the ion beam, allowing cooling and collision experiments at the same time. For constant cooling the electron cooler was used. Its electron gun was operated at a voltage of 1023V. With an expansion $\xi$ of 9.6 and an electron current of 35.4 mA, this leads to an electron density $n_e = 1.8 \times 10^7\ cm^{-3}$. A space charge correction of 84.65 V, thus a cooling energy in the laboratory frame of

938.35 eV was derived. The electron target was used for the collision experiments. The electron beam was expanded by $\xi = 30$ with an electron current of 4 mA. This leads to an electron density $n_e \approx 2.3 \times 10^7$ cm$^{-3}$
To eliminate relative drifting of the platform voltages of both devices, electron cooler and target, are connected to the same base potential. For the energy variation of the electron target a fast bipolar high voltage supply (Kepco BOP1000M) was installed on top of the electron target platform, which allows to increment or decrement the electron targets platform voltage by ± 1000 V.
All important information such as for instance the electron currents, the platform voltages as well as the detector countrates and pulse heights is recorded with the 32 channel scaler and 8 channel ADC (see chapter 3.4.1). The data were acquired according to the procedure in chapter 3.4. For the current measurement the precooling step was set to 3 s allowing, apart from the phase space cooling the electron cooler, also radiative cooling of the ion beam. The electron target was set to a relative energy in order to avoid additionally faster beam decay due to the high DR rate at zero relative energy. This energy is chosen in such a way that the energy can be used to get an absolute calibration of the $D^+$ rate to the ion beam current as it is described in the section of "ion current normalization". During the measurement all steps of the wobble cycle had a length of 50 ms and each cycle was repeated 100 times for each injection and relative energy respectively. The energy of the cooling and reference step was set to the same energy allowing to use both signals for the ion beam normalization as well as for the background substraction of the $D^-$ rate. In the next section the data processing and the final rate evaluation is presented.

### 4.1.2 Data processing

The window in the ADC spectra of the ion pair measurement of $HD^+$ was set to 1800 to 3200 ADC bits according to figure 3.21. The data analysis follows then the general data processing procedure as described in chapter 3.4.3 whose intermediate result that was used for the online analysis is shown in figure 4.1. The data processing of the ion pair formation of $HD^+$ will be discussed in the following.

#### Background substraction of the $D^-$ rate

As mentioned in chapter 3.5 the not electron induced rate was constant during the whole experiment. Therefore it was possible to substract a constant value from the raw rate, normalized to time.

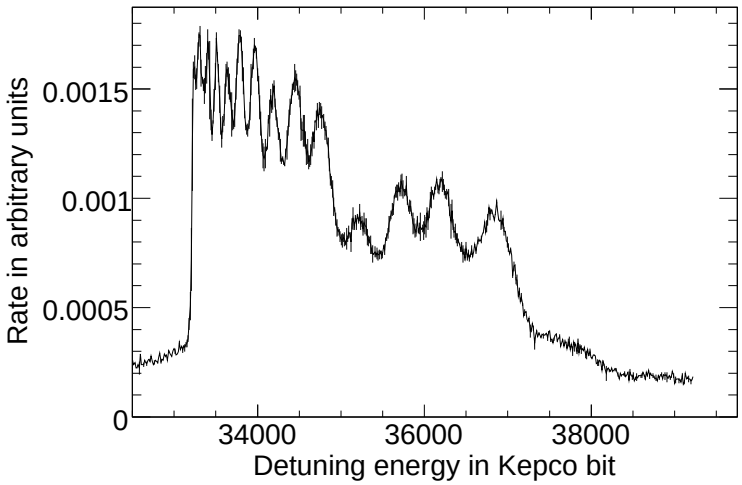


Figure 4.1: *Raw rate versus Kepco bit of the ion pair measurement of $HD^+$.*

### Normalization in respect to the ion current

For the $HD^+$ ion pair formation the count rate was normalized indirectly to the ion current. This was done taking the time normalized count rate of the $D^+$ signal from the precooling step at the energy of 10 eV, comparing this value with a previously measured DE rate coefficient [52] at the same energy and recalculating this rate coefficient to the ion current using formula 2.20, taking the electron density from the present measurement into account. This leads to a conversion factor of the measured count rate of $D^+$ to the number of ions in the storage ring. This factor has been used to transform the $D^+$ count rate at cooling energy and restgas DE, respectively, to number of ions. The $D^-$ rate was normalized by these histograms giving the rate $R_{ion}$ as

$$R_{ion}(E) = \frac{R_{D^-}(E)}{I_{ion}(R_{D^+_{cool,ref}})}\frac{L}{l}. \tag{4.3}$$

### Determination of the cooling energy

As a space charge corrected laboratory energy at cooling the value of 944.34 eV was obtained for the electron target, by subtracting the space charge potential of the electron beam from the directly measured uncorrected energy. This cooling energy is 6 eV higher than the value derived for the electron cooler. A reason for this deviation of the cooling energies could be the space charge potential of the electron cooler. This has a parabolic shape with the maximum in the center of the electron beam [57]. A slight misalignment of the ion beam with respect to the

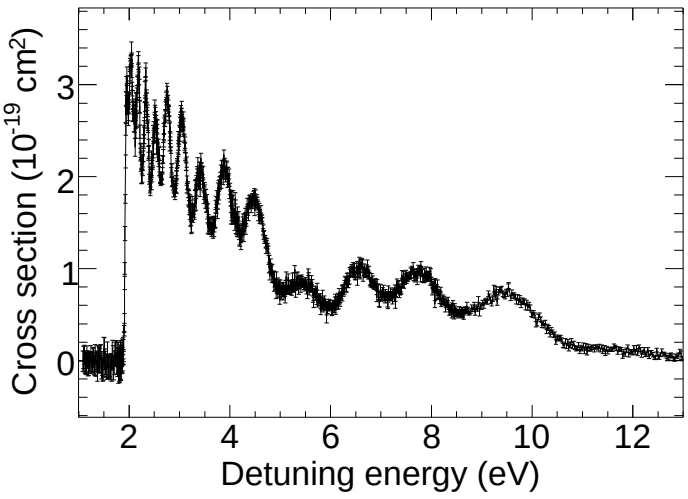


Figure 4.2: *Total cross section of the $D^- + H^+$ channel of the ion pair formation of $HD^+$. The threshold energy of 1.92 eV fits nicely to the predicted one of 1.913 eV. 14 well resolved peaks can be observed, which are caused by quantum interference.*

electron beam can induce a wrong space charge correction. Due to the observation of the cooling of the ion beam with the imaging system in the BAMBI beamline, such a effect could be excluded for the electron targets probing beam.

### 4.1.3 Experimental results

Considering the data processing steps described before the final cross section is obtained. The cross section spectrum (figure 4.2) shows a sharp threshold energy of $(1.92 \pm 0.04)$ eV which fits well to the calculated value of 1.913 eV. The maximum cross section is reached at 2 eV with a magnitude of $3.4 \times 10^{-19}$ cm$^2$. Comparison with the previous CRYRING experiment (cf. [81]) shows overall similar shape and magnitude. However, towards the energetic threshold additional features became visible, thanks to the higher energy resolution achieved at the TSR (see fig. 4.3). Below the dissociation limit, marked by the blue dotted line in figure 4.3, five clearly resolved peaks can be distinguished in the present experimental data down to the energy threshold, in contrast to the previous CRYRING data. In the latter the oscillatory structure becomes unclear below 2.2 eV and at most four peaks can be identified. Additionally the oscillatory structure appears sharper in the present ion pair experiment.
These peaks are caused by an interference effect between the doubly excited capture state and several Rydberg states during the dissociation process [81]. In analogy to the two-slit experiment in quantum mechanics it was suggested that

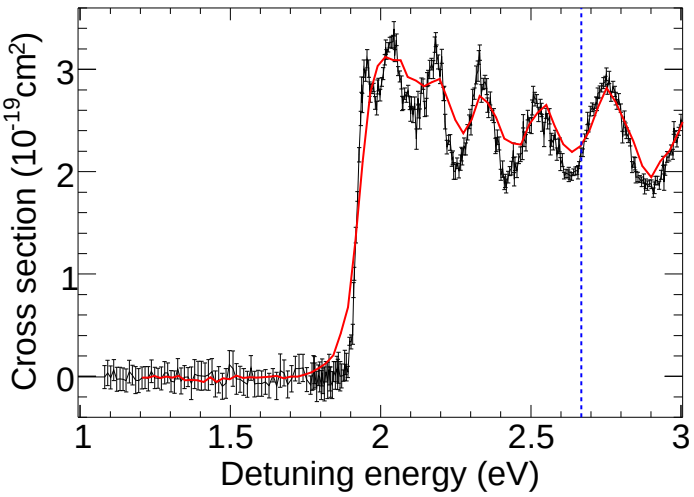


Figure 4.3: *Comparison of the previous ion pair measurement at CRYRING (red) and the present experiment (black). The blue line indicates the dissociation limit, below which the TSR data show five clearly resolved peaks of the interference structure, while the CRYRING data only show four.*

the electron is captured into a resonant state, from where the system can dissociate either directly or along a Rydberg state. Before dissociating the system can then cross back to the resonant state at certain distances in the potential landscape (see fig. 4.4). Different models were developed calculating the interfering pathways. These calculations will be presented in the following sections.

### 4.1.4 Comparison of theoretical calculations and experiment

Several different theoretical calculations are currently available which attempt to explain the structure of the cross section observed in experiments. These theories and their results will be briefly introduced and compared to the experimental results in the following.

#### The Landau-Zener-Stückelberg model

The Landau-Zener-Stückelberg (LZS) model is a semiclassical calculation which is based on the set of potential curves shown in fig. 4.4. There the black solid curve represents the ground state of the molecular ion, while the red solid lines represent a manifold of Rydberg states. The second black solid line represents the resonant state into which the electron is captured and which is diabatically correlated to the ion pair channel at infinite internuclear separations. Parity conservation requires

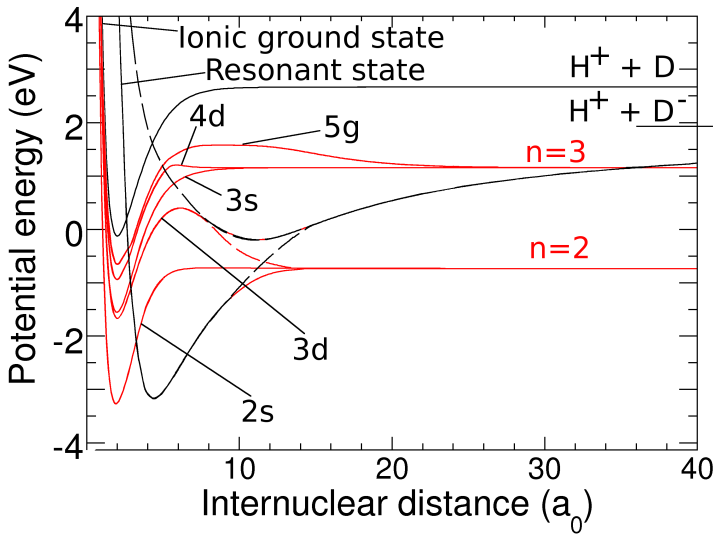


Figure 4.4: *Diabatic potentials of hydrogen and the hydrogen molecular ion as used in the theoretical calculations. The lowest two curves are shown in the diabatic representation, and the dashed lines indicate the corresponding diabatic potentials [82].*

that since the resonant state has even parity, any state coupling go to it must have even parity as well, consequently restricting the quantum number $l$ to even numbers ($s$, $d$ and $g$ states in figure 4.4). In the diabatic representation the resonant state $(2p\sigma_u)^2$ crosses the Rydberg states both at small and at large internuclear distances. The resonant state couples to the latter by the electronic part of the Hamiltonian inducing different pathways to the ion pair limit. For the LZS calculation the $2s$, $3d$, $3s$ and $4d$ Rydberg states are included. Apart from the main resonant state also a second resonant state is taken into account (black dashed line). The transition probability of two diabatic states is determined by equation 2.10. For the present calculation it was suggested that the Rydberg states of s-symmetry are coupled stronger to the resonant state than the $d$ states. Neglecting fine structure, the potential curves possess an n-fold degeneracy for $R$ going to infinity. The potential energy curve of the resonant ion pair state crosses these Rydberg curves at distances of about $R = 11.2a_0$ and $R = 35.6a_0$ respectively. A series of calculations were carried out [10], where the quantum interference effects were primarily controlled by the energy-dependent phases accumulated along the different pathways. In the Wentzel-Kramers-Brillouin-approximation (WKB-approximation) [30; 32; 47] this phase is given by

$$\varphi_j(E) = \int_{R_E}^{R_{final}} \sqrt{2\mu(E - V_j(R))}dR \tag{4.4}$$

where $R_E$ is the appropriate Condon point, a point where the initial excitation step equals the collision energy $E$. The dissociation amplitudes $A_j(E)$ for different pathways $j$ are reduced by the flux into the Rydberg state whose dissociation limit is above the ion pair threshold. With a capture probability of an electron $P_{cap}$, the assumptions that the dissociation in both ion pair channels has equal probabilities and that the total dissociation amplitude is a coherent sum of the amplitudes, the cross section becomes [10]

$$\sigma_{ip}(E) = \frac{2\pi^3}{E} P_{cap}(E) \Big| \sum_j A_j(E) exp[i\varphi_j(E)] \Big|^2 , \tag{4.5}$$

where the index $j$ denotes the Rydberg states. Figure 4.5 shows the calculated cross section [10] in comparison with the present and the previous CRYRING experiment. The overall agreement of the interference structure is fairly good in comparison with the present results, but agrees even better with the CRYRING data, despite an overall mismatch by a factor of 2 in the amplitude. However, the better agreement of the calculation and the previous data are mainly caused by the different resolutions of the both storage ring experiments, which lead to a smear out of the structure at the threshold energy of the older data set. Nevertheless there are still discrepancies of the LZS model and the previous measurements and of course to the present experiment. The authors of the model [10] believed that the differences are caused by this rather simple model, for instance that only one symmetry is included.

**Wave packet propagation method**

The wave packet method was introduced in the 1970's [20] and is based on the numerical solution of the time-dependent Schrödinger equation (in atomic units)

$$i\frac{\partial}{\partial t}\Psi(R,t) = H(R,t)\Psi(R,t) \tag{4.6}$$

where the Hamiltonian $H$ includes the kinetic energy operator and the potential energy matrix. Recently Larson and Orel further developed this method in order to test the influence of various couplings on the system [7]. They used the same potential energy curves like it was done for the LZS method (fig. 4.4) and including the coupling between these curves. Two sets of wave-packet propagation were calculated taking the capture of an s and d electron into account. The cross section is then described as an incoherent sum of s and d cross sections and calculated through

$$\sigma_j(E) = g\frac{2\pi^3}{E}|T_j(E)|^2 \tag{4.7}$$

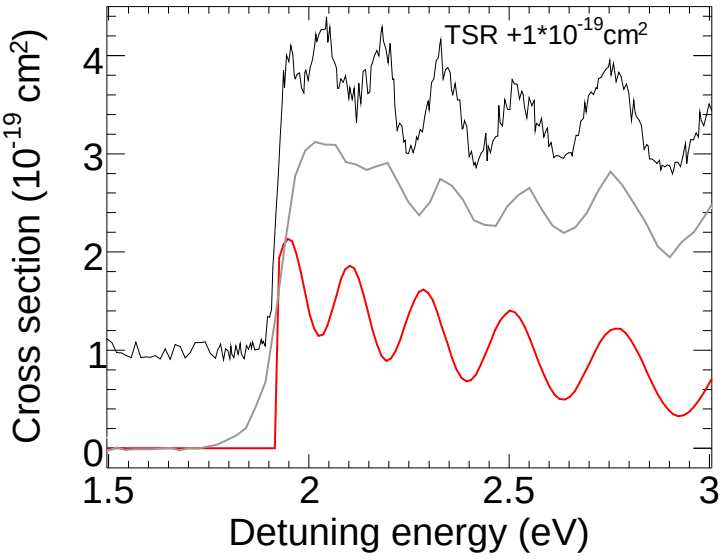


Figure 4.5: *Comparison of the calculated cross section using the LZS method [10] (red) with the experimental one from the previous CRYRING experiment (grey) [54] and the present experiment (black).*

where $T_j(E)$ is the projection of the wave packet $\Psi_j(t, R)$ onto the asymptotic scattering wave function (for more details see [7]) and $g$ the multiplicity ratio of the neutral and ion states as well as for the two ion pair channels. The result of these calculations is shown in fig. 4.6. Larson and Orel found out that the main source of the oscillations in this calculation are due to couplings with $n = 2$ and $n = 3$ final states, i.e. states that asymptotically correlate to the H(1s) + D($n$=2,3) and D(1s) + H($n$=2,3) states, and the resonant state. Note that the presented theoretical cross section was scaled by a factor of 2/3 in order to match the amplitude to the experimental cross section. A careful comparison between theory and experiment shows that the predicted interference structure does not coincidence with either measurements. One reason according to the authors of this theory might be the uncertainty in the knowledge where the couplings at small internuclear distances occurs [7]. However, as shown in the next section latest calculations show that the oscillation causing PEC was not included neither in this calculation nor in the older LZS calculation.

### Results of a recent semiclassical calculation based on the LZS model

A recent calculation [82] has been motivated by the present new high resolution measurements. It is mostly based on the LZS model. However, it differs in the choice of the potential curves included. In this model only the $3d$ and $5g$ Rydberg

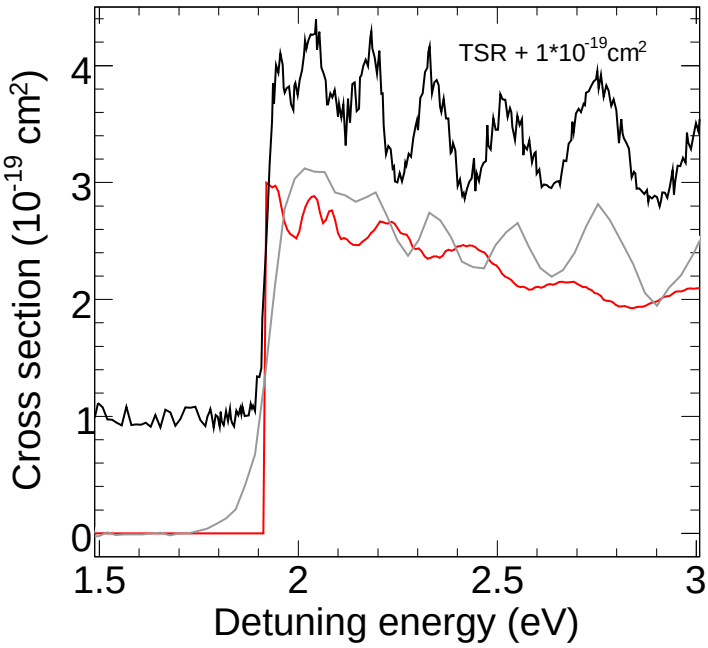


Figure 4.6: *Shown in this plot is the cross section of the previous CRYRING experiment [54] and the present experiment in comparison with the wave-packet method from Larson et al [7] in an energy range of 1.5 to 3 eV. (For more details see text)*

states besides the resonant state are included (see also figure 4.9). In this case the cross section is determined to

$$\frac{\sigma_{IPF}^{total}}{\sigma_{IPF}^{total} + \sigma_{DR}} = |A_{3d}|^2 + |A_{5g}|^2 + 2A_{3d}A_{5g}\cos\left(\varphi_{5g} - \varphi_{3d}\right) \tag{4.8}$$

according to formula 4.5, with the total experimental cross section $\sigma_{IPF}^{total}$ including both ion pair channels (twice the value of the present experiment), $\sigma_{DR}$ the experimental DR cross section, $\varphi_j$ calculated by formula 4.4 and $A_j$ the transition amplitude between the resonant state and the $3d$ or $5g$ state. The cross section calculated according to this formula [82] is shown in figure 4.7. Although only two states are involved in the interference pathways the calculation finds an overall agreement with the measured peak structure and position. Comparison of the previous LZS model [10] and the new calculation [82] poses the question why the results are so different although, the cross section is calculated in the same way and additionally the new calculation uses less states. However, the recent calculation explicitly uses the evidence given by Sidis et al. [79] that for each final channel

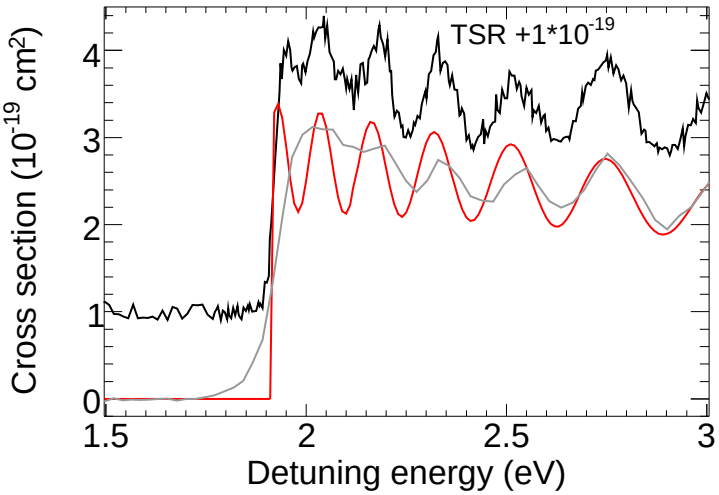


Figure 4.7: *Comparison of the calculated cross section using the new LZS method (red) of X. Urbain [82] with the experimental one from the previous CRYRING experiment (grey) and the present experiment (black) measurements.*

with quantum number $n$ only two states can couple with the doubly excited potential curve. In this case of $HD^+$ only the states labeled with $3d$ and $5g$ contribute to the $n = 3$ crossing. In contrast to the previous calculation, no contribution from the $n = 2$ crossing is accounted for, resulting in very good agreement with the new experimental results. This latest result will be further used for the comparison with the empirical fourier treatment of the $HD^+$ ion pair cross section.

## 4.2 Empirical treatment of the $HD^+$ cross section using the Fast-Fourier-Transformation (FFT) technique

The latest LZS calculation shows, that the structure is mainly caused by the phase difference along two different potential energy curves. According to this result one could expect that the cross section plotted against a dedicated term of equation 4.4 could lead to a regular oscillatory structure of a certain frequency. To analyze the cross section following this assumption the energy axis was rescaled in order to obtain this frequency by using a fourier transformation. Therefore within this thesis an application of the Fast-Fourier-Transformation (FFT) technique was developed in order to link certain areas between potential curves to the interference structure of $HD^+$. For this purpose the phase difference of the pathways through

the potential curves was modeled semiclassically. Following this treatment, the energy axis of the cross section was rescaled, the FFT adopted and finally compared to the potential energy curves. In the following the semiclassical approach will be shortly described, which will be followed in a next section by the application of the FFT and its results.

### 4.2.1 Semiclassical approach

A semiclassical approximation in quantum physics accounts for small perturbations of a classical calculation. In this case the semiclassical WKB-phases (formula 4.9) will be used to express a phase difference between two potential curves along which a wave packet can travel and interfere. Starting with 4.9 and taking figure 4.8 into account, the phase over a single PEC can be written as

$$\varphi_j(E) = \int_{R_E}^{R_{final}} \sqrt{2\mu(E - \overline{V} - \delta V_j(R))} dR \tag{4.9}$$

with $V_j(R) = \overline{V} + \delta V_j(R)$ and $\overline{V}$ as an arbitrary constant average potential and $\delta V_j(R)$ a partial potential (see figure 4.8). Here the kinetic energy $(E - \overline{V})$ is assumed to be constant during the passage of the interference area, as given by the electron impact energy. Assuming that $\delta V_j(R) \ll (E - \overline{V})$ and expanding the square root up to the first order gives

$$\varphi_j(E) \simeq \sqrt{2\mu(E - \overline{V})} \int_{R_E}^{R_{final}} \left(1 - \frac{1}{2}\frac{\delta V_j(R)}{E - \overline{V}}\right) dR \tag{4.10}$$

Taking the second phase $\varphi_i(E)$ of the second PEC into account calculating the difference of the phases one gets

$$\boxed{\varphi_j(E) - \varphi_i(E) = \Delta\varphi(E) \simeq \sqrt{\frac{\mu}{2(E - \overline{V})}} \int_{R_1}^{R_2} \Delta V(R) dR} \tag{4.11}$$

with $\Delta V(R) = \delta V_i(R) - \delta V_j(R)$ and $\mu$ is the reduced mass of the HD molecule in atomic units. In this approximation the square-root corresponds to a reciprocal velocity. The product of this and $dR$ is then the time $\Delta t$ for the wave packet traveling through the area between the interfering potential curves $\Delta V(R)dR$, which is hereafter called interference area. Taking into account that an accumulated phase $\Delta\omega\Delta t$ can be expressed by $\Delta E\Delta t$ in atomic units, the right hand side of equation 4.11 corresponds to such a phase of an interfering wave packet.
Following this approximation the cross section can be expressed in analogy to equation 4.11 approximately by $(1 + \cos\Delta\varphi)$ and the multiplication with an energy dependent factor, which represents an average cross section given in the case

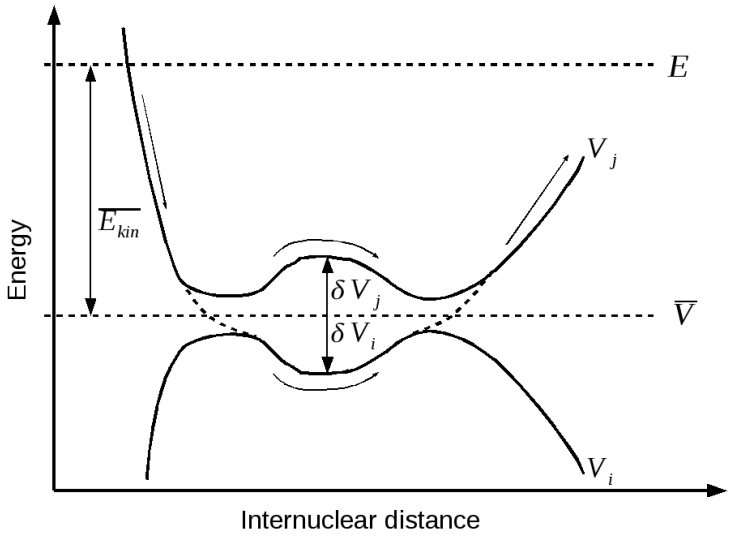


Figure 4.8: *Schematic drawing of potential energy curves as used in the semiclassical approach, including the total energy $E$, the average potential $\overline{V}$, the kinetic energy $E_{kin}$ and the partial potentials $\delta V_{i,j}(R)$. For more details see text.*

of $HD^+$ by a fit of a straight line to the overall structure in the energy range below 6 eV of the experiment. Here the factor in front of the integral of $\Delta\varphi$ represents within this approximation the reciprocal velocity of the wave packet in dependence of the electron impact energy $E$. The two factors of 4.11 are used for a Fourier transformation of the cross section and accounting the transformation results to a certain area in the potential energy landscape. These two steps of the analysis will be discussed in more detail in the following.

### 4.2.2 Rescaling of the energy axis

Following equation 4.11 the energy axis of the cross section was rescaled by representing the cross section as a function of $\left(\sqrt{\frac{\mu}{2}\frac{1}{E-\overline{V}}}\right)$ for several average potentials $\overline{V}$ in order to find an optimal value $\overline{V}$ yielding a regular oscillatory structure. Various calculations were performed using average potentials in the energy range of -1.0 eV to 1.82 eV (see figure 4.10). Using these potentials the energy axis of the cross section was rescaled and then transformed to the atomic units scale. Figure 4.10 show the original cross section and the cross section with the rescaled energy axis for the potentials $\overline{V}_1$ = -1.0, $\overline{V}_2$ = 0.76, $\overline{V}_3$ = 0.9, $\overline{V}_4$ = 1.16 and $\overline{V}_5$ = 1.82 eV (see figure 4.9).
Regular structure was observed in the plots with average potentials of 0.76, 0.9

and 1.16 eV. In order to find dominating frequencies and therefore interference areas according to formula 4.11. the FFT technique was applied to these data sets, where the integral describes the oscillation frequency dominating the cross section. These areas could then be adopted to areas in the potential energy curve (green framed area in figure 4.9).

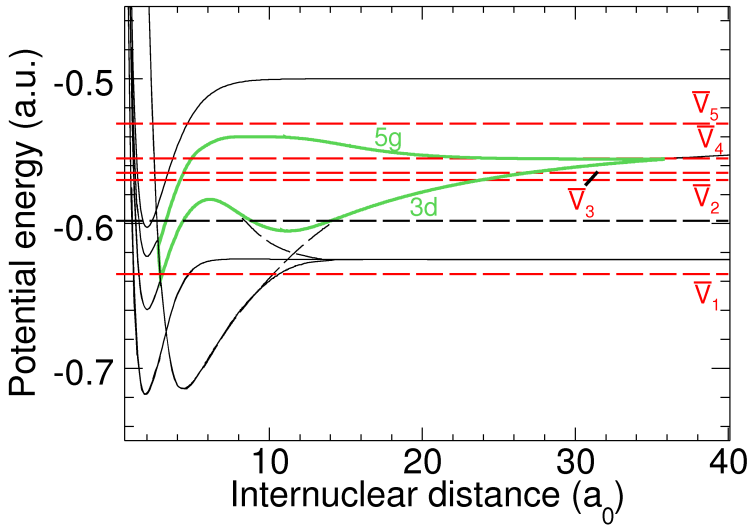


Figure 4.9: *Potential energy curves as used in the new recent LZS-model [82] and for the Fourier transformation.* $\overline{V}_i$ *are different average potentials (for more details see text); green framed: interference area corresponding to the new LZS-model.*

### 4.2.3 Application of the FFT on the ion pair cross section

The Fast Fourier Transformation (FFT) is an algorithm for fast calculations of a discrete Fourier Transformation (DFT). Basically the FFT uses intermediate results and can therefore save several arithmetic operations, which are needed for the direct calculation. This technique, attributed to Cooley and Tukey [45], can be used if the number of the analyzed points have a power of two. If this is the case the DFT with 2n points can be divided in two calculations with n points, whereas one calculation uses the even and one the odd points. In each case the characteristic of the root of unity of the Fouriermatrix is utilized. The FFT was included in the data analysis routine by the FFTW3 library [49], included in the data analysis software root.
The results of the analysis can be recombined afterwards using the magnitude and phase information. In the present calculations cuts on the spectra could be performed, meaning e.g. setting the magnitude for a certain chosen interval to

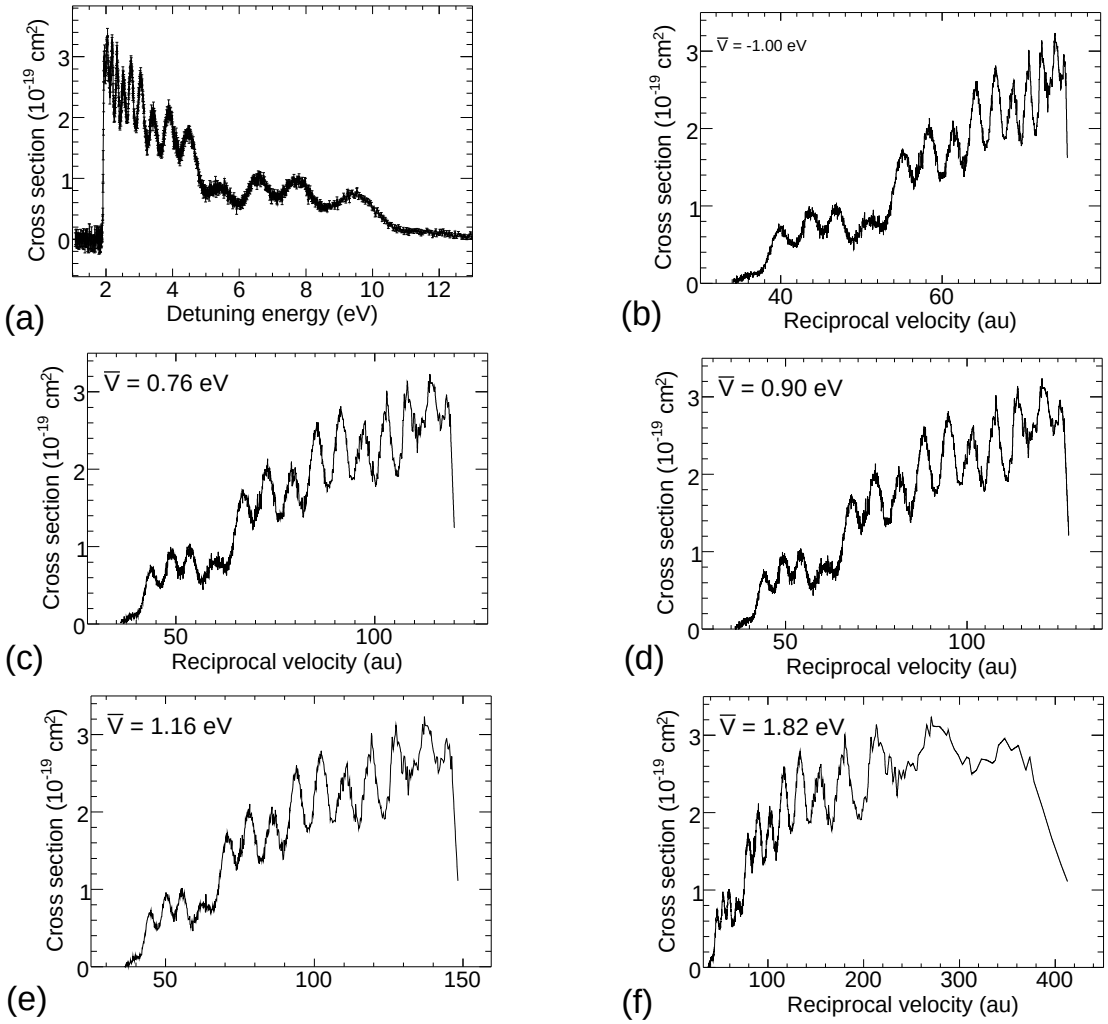


Figure 4.10: *Shown here is the cross section versus energy (a) and a few examples versus the reciprocal velocity for different potentials* $\overline{V}$*. For (b) (*$\overline{V}_1 = -1.0$ *eV) as well as for (f) (*$\overline{V}_5 = 1.8$ *eV) no overall regular structure is observed, while (c),(d) and (e) (*$\overline{V}_2 = 0.76$ *eV,* $\overline{V}_3 = 0.9$ *eV and* $\overline{V}_4 = 1.16$ *eV) show regular structure.*

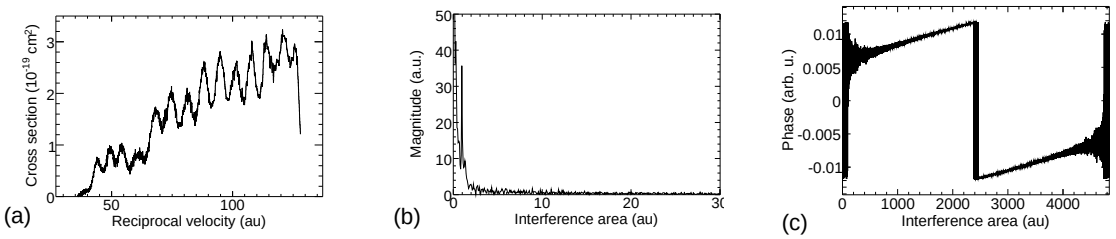


Figure 4.11: *Cross section (a) with the energy axis rescaled to a reciprocal velocity in atomic units (au). In this case $\overline{V}$ was chosen as 0.90 eV. (b) and (c) show the FFT of (a) In (b) two well defined peaks are visible belonging to a certain interference area.*

zero. Then the Fourier analysis gives clear access in the involved processes. In this case this cutting procedure was applied to the magnitude spectrum (figure 4.11(b) to prove which structure in the FFT belongs to a interfering area following equation 4.11. (results see further down). The phase itself (figure 4.11(c)) gives no information about the physics of the system and will therefore not be mentioned further.

### Result of the FFT for the cross section versus the reciprocal velocity

FFT calculations were carried out for some of the average potentials found in section 4.2.2. Indeed the three different potentials 0.76 eV, 0.9 eV and 1.16 eV produce a significant peak structure in the Fourier transformed spectrum. For 0.76 eV the Fourier spectrum shows only a single broad peak which is responsible for the whole oscillatory structure and belongs to an interference area of 1.05 au (figure 4.12(a). Cutting this peak away leads to a loss of the interference structure in the back transformed figure. Using 0.9 eV for $\overline{V}$ produces two well separated peaks at 0.95 and 1.33 au. Here the peak at the lower interference area is the sharpest and strongest peak in the whole series of calculations. Both peaks belong to the oscillatory structure. In this case the strong peak at the smaller area belongs to the main structure for the low energy part and therefore high reciprocal velocities, as a cutting of the FFT spectrum shows (figure 4.12(b)). For 1.16 eV also two peaks are observable. However, the second peak with a bigger interference area is not as well separated from the other peak as it is the case for 0.9 eV. There the first peak with an area of 0.75 au belongs mainly to the structure of the low energy range, while the second one with its area of 1.13 au belongs to the high energy part (figure 4.12(c)). This series of FFTs shows that separate regular interference structures appear for $\overline{V} \approx 0.9...1.16$ eV with interference areas of $\sim 1.0...0.7$ au at $1/v$ of $\sim$ 70–130 au and of 1.3 au for $1/v \sim$ 40–60 au respectively. In particular, the interference structure at large $1/v$ (i.e., low $E$) persists over

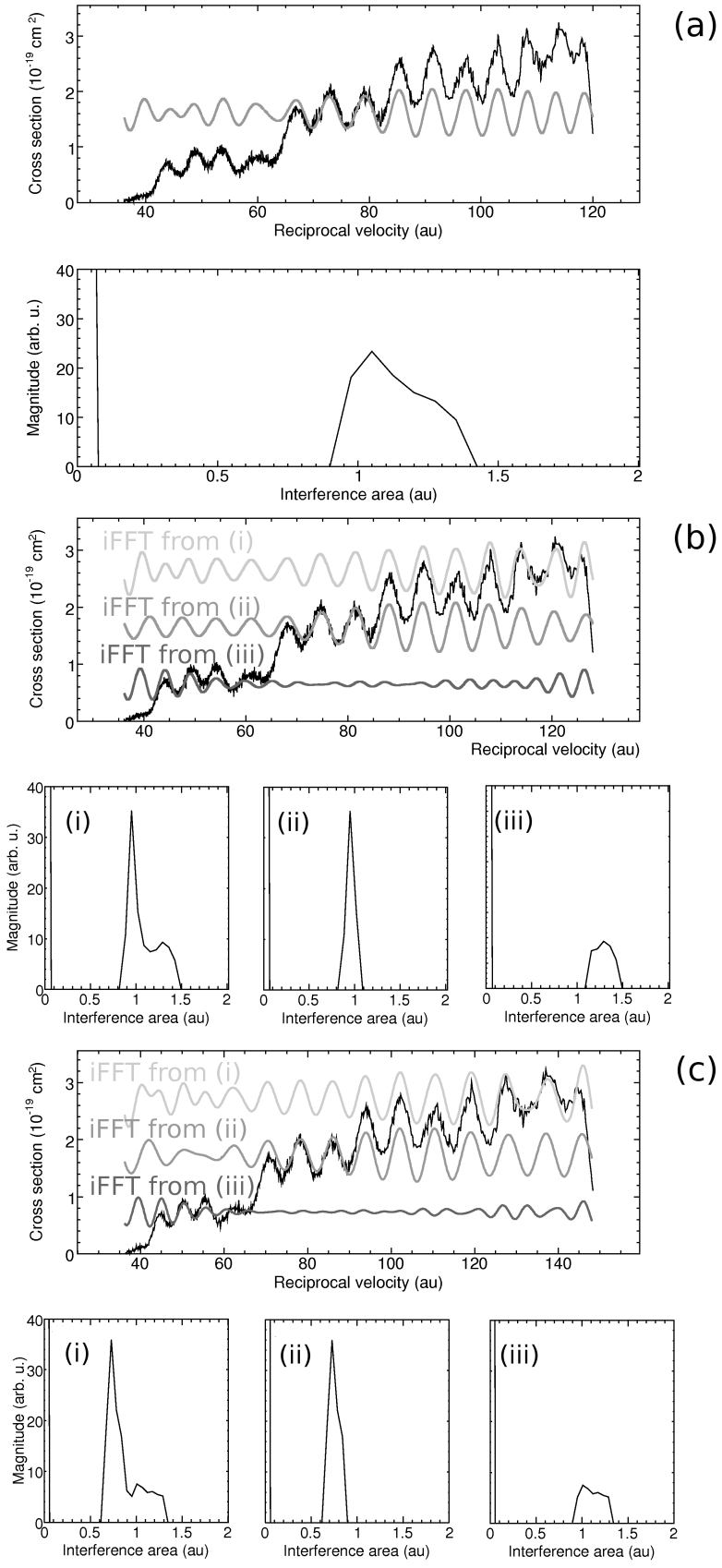


Figure 4.12: *FFT and its inversion iFFT for* $\overline{V}$ = 0.76 *eV (a),* 0.90 *eV (b) and* 1.16 *eV (c). For more details see text.*

almost 10 full oscillations in the TSR experiments. In the following these results will be compared to the calculation using the newest semiclassical LZS calculations [82].

**Comparison of the FFT results with the new semiclassical results**

Considering figure 4.9 and the newest semiclassical results (figure 4.7) the two pathways leading to the interference structure of the $HD^+$ ion pair structure are the 3d and 5g state (green framed in figure 4.9). Therefore the area between these two curves was calculated and compared to the area obtained from the FFT analysis. An area of 0.95 was found, which fits very well to the main peak for the FFT calculations using $\overline{V} = 0.9$ eV. This was also verified by fitting the theoretical phase difference of the fraction of an area $A$ and the reciprocal velocity letting $\overline{V}$ as free fitting parameter [82]. Indeed this fitting procedure shows, that $\overline{V} = 0.9$ eV gives the best result. However, the second peak with an area of 1.3 au could not be assigned to a set of potential curves used. This area could be caused by missing states in the calculation which possibly belong to the structure and behavior of the cross section for the high energy and low reciprocal velocity part, respectively.

## 4.3 Ion pair formation of $H_3^+$

The capture of an electron by $H_3^+$ can lead to the formation of a doubly excited state, which subsequently dissociates either into neutral or ionic fragments or both species at the same time. Ion pair formation becomes possible once the energetic threshold is passed. Two different channels, one two body and one three body, can then be accessed:

$$H_3^+ + e^- \rightarrow H_3^{**} \rightarrow \begin{cases} H^- + H_2^+ & (E > 5.4\ eV) \\ H^- + H^+ + H & (E > 8.1\ eV) \end{cases} \tag{4.12}$$

The two body channel requires a minimum energy of 5.4 eV, which is determined by

$$E_{\text{thr.,2 body}} = E_{\text{bind},H_3^+} + E_{\text{ip},H_2} - E_{\text{ip,H}} - E_{\text{bind},H^-} \tag{4.13}$$

with $E_{\text{bind},H_3^+}$ and $E_{\text{bind},H^-}$ the binding energy of $H_3^+$ (4.37 eV [63]) and $H^-$ (0.76 eV [36]) respectively, $E_{\text{ip},H_2}$ and $E_{\text{ip,H}}$ the ionization potential of $H_2$ (15.43 eV [59]) and H (13.6 eV [59]), respectively. The energy of the three body channel is determined in this case by

$$E_{\text{thr., 3 body}} = E_{\text{bind},H_3^+} + E_{\text{bind},H_2} - E_{\text{bind},H^-} \tag{4.14}$$

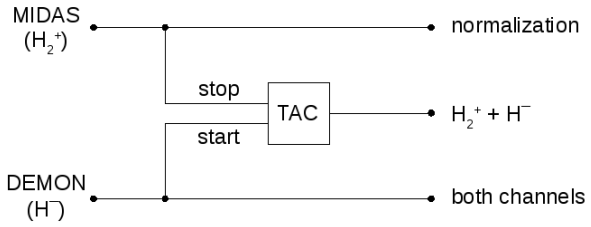


Figure 4.13: *The measurement scheme as applied for the coincidence measurement of $H^-$ and $H_2^+$.*

with $E_{\mathrm{bind,H_2}}$ the binding energy of $H_2$ (4.48 eV [28]). So far previous experiments succeeded to detect the $H^-$ product only, not being able to distinguish between either reaction path [14; 25; 68]. Employing the new detector setup at the TSR, the breakup into both channels could be studied independently for the first time. The measurement will be presented in the following and compared to previous results.

### 4.3.1 Ion pair measurement at the TSR

The $H_3^+$ ions were produced by the CHORDIS ion source, which were used previously for the $HD^+$ production (see chapter 4.1) and then accelerated by the HCI and the post accelerator to a final energy of 5.19 MeV. Due to the same mass and energy as the diatomic deuterated hydrogen, the TSR could be operated at similar settings. However, in order to guide the light fragment $H^-$ to the detector, slight corrections to the ion beam trajectory behind the electron target section become necessary. As described in chapter 3.3, an additional angle was applied to the ion beam allowing the light $H^-$ fragments to pass the entrance gap of the dipole chamber. Additionally the detection efficiency could be increased by adjusting an extra angle to the ion beam trajectory by using the electron target correction magnets KDY. Unfortunately not all $H^-$ fragments could be focussed onto the detector (see also chapter 3.3), causing a deficiency which had to be corrected in the subsequent offline analysis as explained later.
As it is possible to measure at the TSR the negative fragments as well as the $H_2^+$ fragments at the same time, a coincidence scheme (see figure 4.13) was set up in order to distinguish the two and the three body breakup in the ion pair formation of $H_3^+$. This becomes possible due to the 100% detection efficiency for the $H_2^+$ fragments using MIDAS. For recording the coincidence rate a time-to-amplitude converter (TAC) was used to convert the time difference of two different events of the two detectors into a pulsheight distribution (see figure 4.14). The evaluated coincidence rate from the TAC can then be used to separate the two channels, whereas the three body channel was derived by subtracting the coincidence rate from the total $H^-$ countrate.
The measurement procedure was similar to the one during the $HD^+$ experiment.

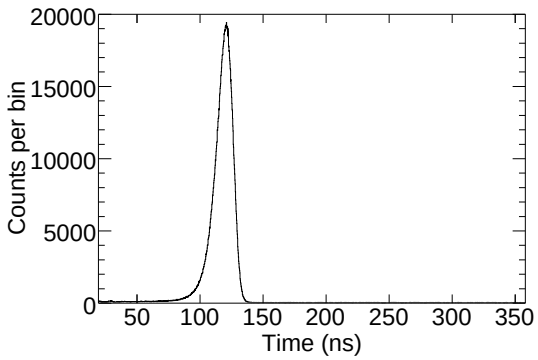


Figure 4.14: *Coincidence time spectrum of the coincidence $H^-$ and $H_2^+$ events on the DEMON and MIDAS detector, respectively. The counts presented in this picture are taken during the measurement step of the wobble cycle and in this stage are not time normalized or sorted to the dedicated energy.*

After precooling for 30 ms, the measurement period lasted 10 s. The latter consisted of 100 cycles each changing in consecutive steps between cooling (15 ms duration), reference (5 ms) and measurement (65 ms) energy, where the energy of the reference step was also set to cooling energy. For the data analysis only the data recorded after 3 s of storage were used, ensuring that the ion beam was cooled down in phase space and vibrationally.

### 4.3.2 Data processing

The data processing is mostly similar to the general scheme presented in section 3.4.3., except for a few changes required. First the additional information from the TAC had to be recorded, requiring a few changes in the data acquisition software md2h.c. Second, the $H_2^+$ rate recorded at cooling and reference energy could directly be related to the ion current, since the common energy of both steps is below the ion pair and DE threshold (about 4 eV). Therefore the $H_2^+$ rate was additionally measured in a separate run, during whose the ion current from the ion current monitor was recorded simultaneously to the countrate. Combining the $H_2^+$ countrate and the ion current it was possible to transform the $H_2^+$ events to a number of ion per second equivalent by a rather simple formula, which also includes the length factor of the ring circumference and the electron target length. Thus the number of ions is calculated through

$$N_{ion} = 19.71 \times N_{\mathrm{H}_2^+}. \tag{4.15}$$

Taking this transformation into account equation 3.4 becomes

$$R_{ion}(E) = \frac{R_{\mathrm{H}^-}(E)}{19.71 R_{\mathrm{H}_2^+ @cool,ref}(E)} \tag{4.16}$$

with $R_{H_2^+@cool,ref}(E)$ being the measured $H_2^+$ counts per second recorded during the cooling and reference step.
The final analysis follows chapters 3.4.3 and 4.1.2. (determination of the cooling energy) and will not be repeated here. To account for the incomplete detection efficiency of the $H^-$ fragments the measured rate was scaled at the maximum value at the energy of 11 eV to the one observed at CRYRING where an absolute determination of the coefficient was achieved (see figure 4.15).

### 4.3.3 Data analysis and comparison to other experiments

Following the measurement scheme and data acquisition described in the former section the total cross section for $H_3^+$ ion pair formation was obtained. Figure 4.15 shows the total cross section as a function of the detuning energy after all analysis steps, including the toroid correction, were applied. In this figure the cross section from the present experiment is also compared to former measurements using the inclined beam [14], single passed merged beam [25] and the storage ring technique (CRYRING;[68]). While the first two measurements were most likely performed with vibrationally excited ions, the data taken at CRYRING were measured with rotationally and vibrationally cooled ions. For the present experiments the $H_3^+$ ions can be assumed in the vibrational ground, but rotationally excited state as shown earlier by Kreckel et al. [37]. The difference to the storage ring results in the energy dependence could thus be caused by the initial ionic vibrational

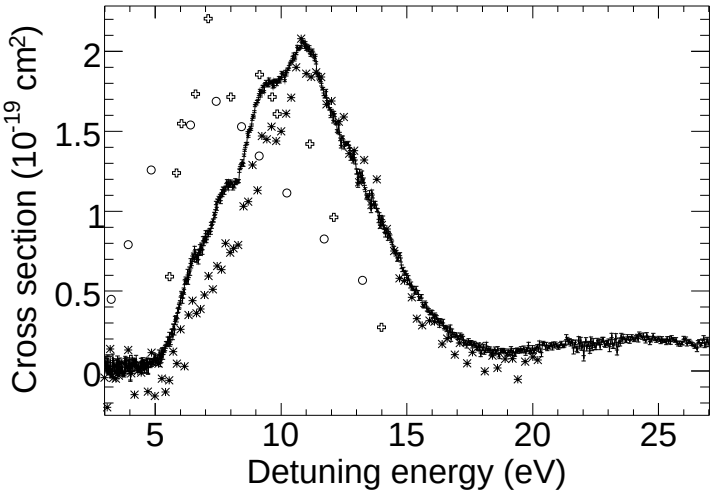


Figure 4.15: *Total cross section $H_3^+$ measured at the TSR (points) in comparison to the measurement of Peart [14] (open circles), Yousif [25] (open crosses) and the CRYRING group [68] (stars).*

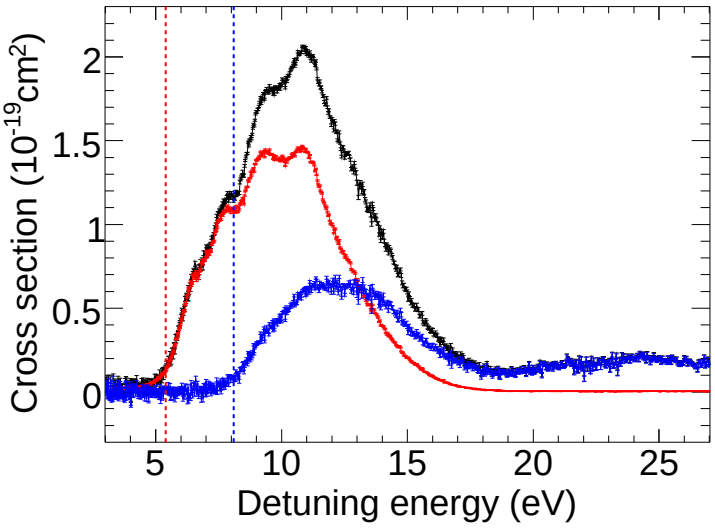


Figure 4.16: *Total cross section $H_3^+$ (black line) including two- (red curve) and three-body channel (blue curve). The dashed red line marks the two body threshold 5.4 eV, while the dashed blue line marks the three body threshold 8.1 eV.*

excitations, whereas the maximum value ($\sim 2 \times 10^{-18}$ cm$^2$) seems to be unaffected and comparable among the experiments. Thanks to the much higher statistic together with the high energy resolution the present data revealed for the first time an oscillatory structure.
Additionally it was, now for the first time, also possible to distinguish the two and three body breakup using the coincidence method described in section 4.3.1. The cross section for the respective reaction path is shown together with the total $H^-$ cross section in figure 4.16. Interestingly the interference structure seems to occur only for the two body channel. In fact, this behavior was predicted by theory [7], since similar to the neutral repulsive curve for $HD^+$ also the resonant state for $H_3^+$ crosses the Rydberg manifold twice, inducing interference patterns.
Furthermore a closer comparison of the measured $HD^+$ and $H_3^+$ cross section shows that the peak structure for $H_3^+$ coincides energetically with the one for the $HD^+$ ion (see fig. 4.17). This might suggest a similar characteristic of the involved potential energy curves (PEC). However, since currently the PEC responsible for the high energy structure have not been identified, any discussion would go beyond the scope of this work.

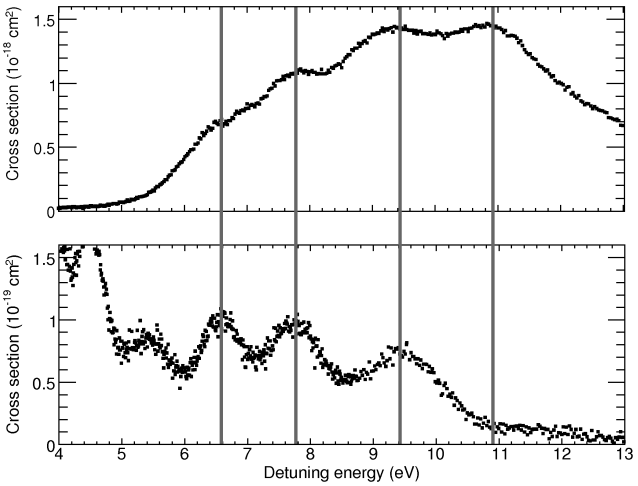


Figure 4.17: *Comparison of the $HD^+$ and the two body channel of the $H_3^+$ ion pair formation. Possibly due to the similarity in the reaction products oscillatory structure at the same energy position (grey lines) occur for both experimental results.*

### 4.3.4 Comparison with theoretical calculations

**Wave packet propagation method**

For the three atomic molecule it is much more difficult to calculate the cross sections. Nevertheless calculations were done for the geometry shown in figure 4.19 [68]. The diabatic states (see figure 4.18 for the one-dimensional case) and couplings needed for this model were calculated using the adiabatic representation transformed by a configuration interaction (CI) calculation (for details see [68]). Thereby two resonant states and four Rydberg states were included [68], of which the highest Rydberg state is an effective state according to the coupling to the ion pair state in order to account for the couplings of the infinite number of Rydberg states converging up to the ion [68]. The potentials shown in figure 4.18 and their couplings [68] are then used to study the dissociation dynamics by using the wave

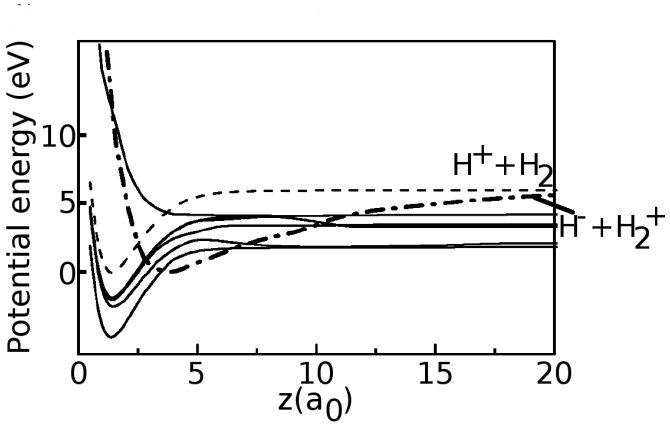


Figure 4.18: *$H_3^+$ potential curves as used in the one-dimensional calculation. Dashed curve is the ionic potential and the solid curves are the Rydberg states of the neutral molecule. The dashed-dotted curve is the diabatic ion-pair state.*

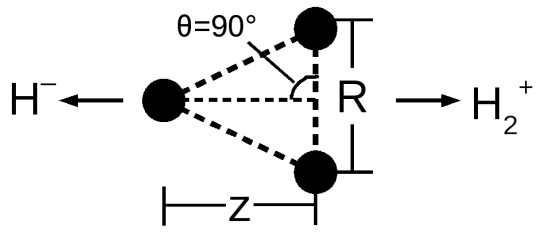


Figure 4.19: *The $H_3^+$ molecule and the coordinates as used in the one- and two-dimensional studies.*

packet propagation on the coupled potentials similar to the $HD^+$ molecule (see chapter 4.1.4) [68]. Starting with wave packets on the two resonant states, the wave packets then propagate by direct integration of the time-dependent Schrödinger equation. The Hamiltonian contains the kinetic energy and the diabatic potentials on the diagonal entries, while the non-diagonal contain the information on the electronic coupling. Leaving the potential be complex above the ion-potential, autoionization of the resonant state is included [8]. The wave packets then propagate to a region where the couplings are zero, so that the cross section can then be obtained from the dissociation flux through a plane with $z = z_{stop} = 15a_0$ (see figure 4.19). The cross section is then given by

$$\sigma(E) = g\frac{\pi^2}{E}\sum_v \frac{K_v}{\mu_z}\left|T(v,E)\right|^2 \tag{4.17}$$

with $\mu_z$ the reduced mass along the z coordinate (see figure 4.19), $K_v$ the wave number of the two body channel fragments, and $T(v,E)$ the dissociation flux for a given Energy $E$ and vibrational level $v$ respectively. In the following studies only the two body breakup was considered.

**One-dimensional study.** To simplify the problem, first a one dimensional study was performed by Kalhori et al (see [68]) where $R = 1.65$ $a_0$ as well as $\theta = 90°$ (figure 4.19) were kept fix. The calculation includes all couplings between the states and shows a double peak structure which is accounted to an interference effect between the two ion pair states. However, the magnitude of the cross section is a factor of 5 higher than the measured ones in the present experiment (two body channel) (see figure 4.20). In addition, the predicted low energy peak is not observed in the experiment and only the position of the calculated second peak coincides with the measurement result. Overall one can conclude that this one-dimensional model oversimplifies the process and gives only an unrealistic treatment.

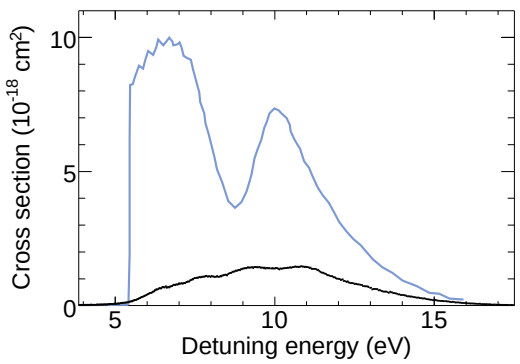


Figure 4.20: *The theoretical cross section (blue line) of the two body channel of $H_3^+$ based on the one-dimensional model (data extracted at [8]) is compared to the experimental results from the present ion pair measurements (black curve).*

**Two-dimensional study.** In this second step Kalhori et al [68] extended the simple one-dimensional model, keeping the angle $\theta$ fixed, while $R$ is allowed to vary (figure 4.19). It turns out, that considering the second dimension washes out the interference effect. The resulting cross section (figure 4.21) including also the losses due to the Rydberg states [8] shows now more similarities to the measured cross section, but still the magnitude remains by a factor of 5 too large and peaks at lower energies. An alternative two-dimensional method in the sense of treating the losses through the Rydberg states, uses the Landau-Zener model and calculates the survival probability along the diabatic ion pair state. This was done by Larson et al [8] using the classical trajectory in the diabatic ion-pair as a reaction coordinate, since the Landau-Zener model itself is one-dimensional. The cross section is now smaller and close to the one measured for the two body channel (figure 4.22). This leads to the conclusion that at least two dimensions are needed to describe the ion pair formation of $H_3^+$, apart from the improved calculations of the couplings between the states [8].

**Multi Configuration Time Dependent Hartree (MCTDH) Method.** Recently, the cross section of the $H_3^+$ two body ion pair channel was calculated, applying the MCTDH method [27]. Additionally the extrapolation of the resonant state and the couplings was improved by Larson et al. [9]. The result of this two-dimensional calculation is shown in figure 4.23. Here a drop in the cross section in comparison to the former calculations, with exclusion of the Landau-Zener model, was observed. Also the overall shape and magnitude fits now at least with the two-body cross section from the present experiment. However, the cross section is shifted in energy, an effect which could not be explained so far.

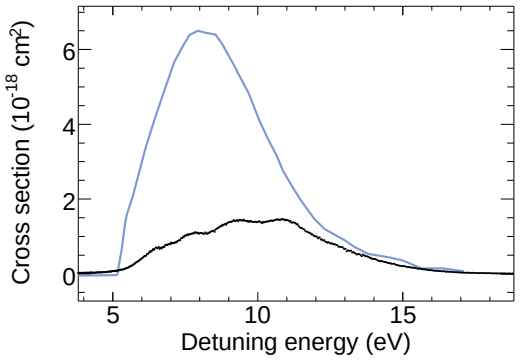


Figure 4.21: *Results of the two-dimensional calculations (data extracted from [8]) for the $H_3^+$ two body channel (blue line) in comparison with the present experiment (black curve).*

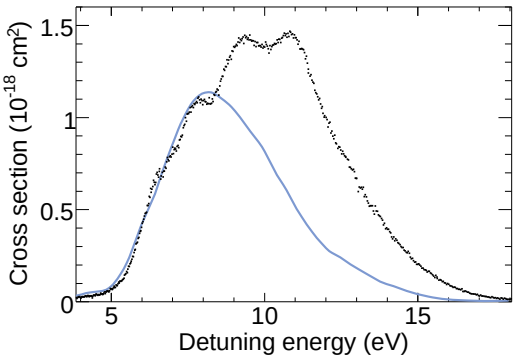


Figure 4.22: *Results of the "LZ-model" calculation of the two body channel (data extracted from [8]) of $H_3^+$ ion pair formation (blue line) in comparison with the present experiment (black curve).*

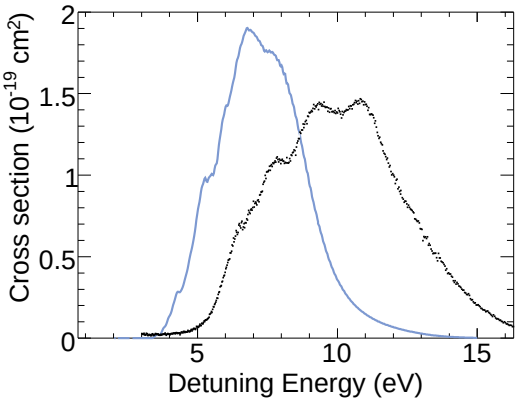


Figure 4.23: *Comparison of the MCTDH method [6; 40] and the present experiment.*

### 4.3.5 FFT treatment of the ion pair cross section

In order to find also in this case an interference area linked to the oscillatory structure on the two body cross section of the $H_3^+$ ion pair formation, the FFT technique was applied using the same simple model as described in chapter 4.2. As can be seen in figure 4.24 the FFT spectrum shows in dependence of the potential no prominent peak, although the peakwidth certainly becomes smaller. This is not a physical effect but rather an analytical fact since the only peak constantely moves towards smaller areas the higher the average potential $\overline{V}$ was chosen. So, the width and position of this peak have no significance. This negative result might be caused by the simple, one-dimensional model used in the semiclassical approach of the FFT procedure. At least it is known from the presented theoretical models

in the section before, that a one-dimensional model cannot reproduce the cross section structure of $H_3^+$. So one can conclude at this point that the FFT procedure has to be modified in that way, that at least a second dimension could be included.

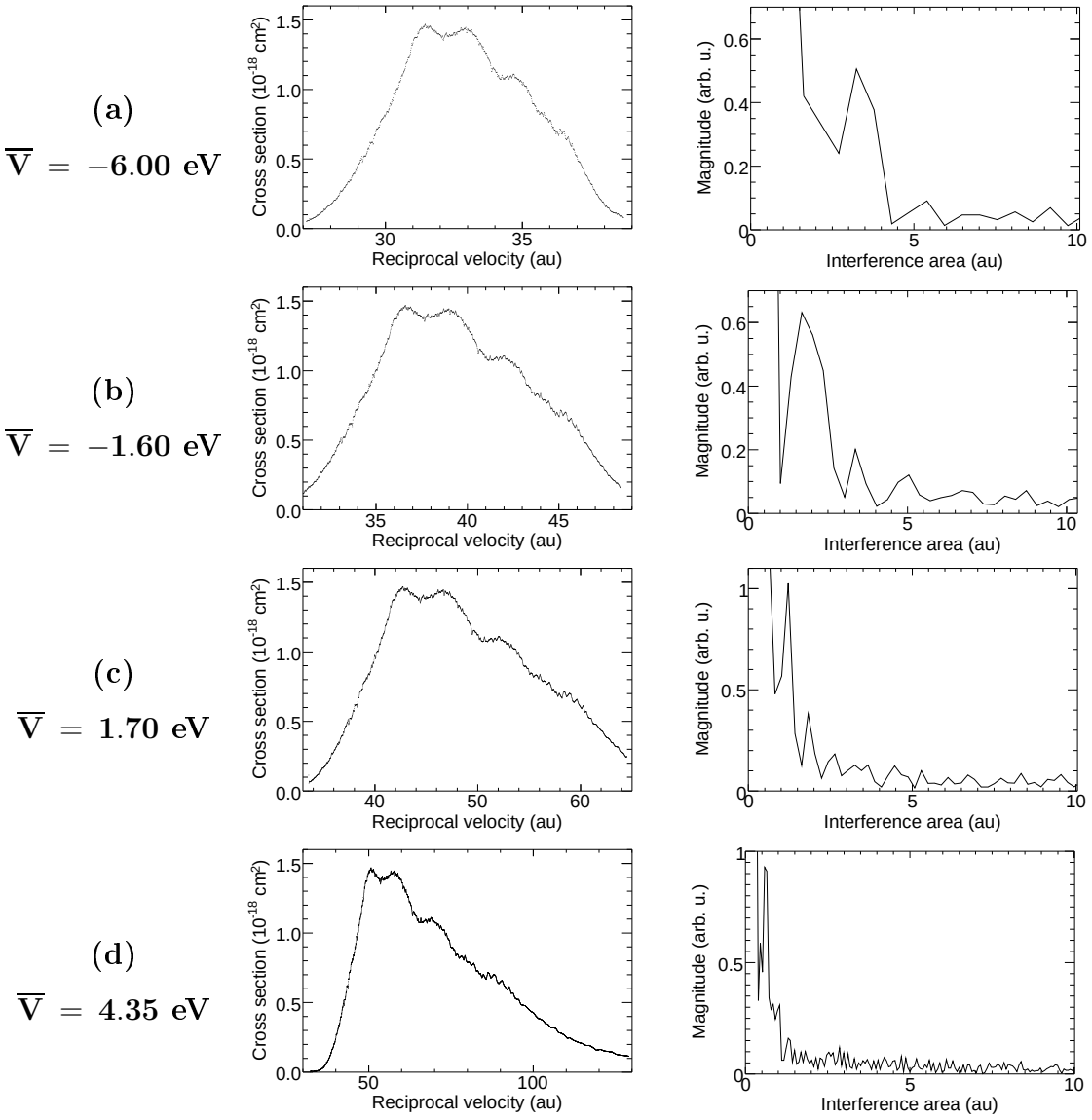


Figure 4.24: *Study of the $H_3^+$ two body ion pair cross section using the FFT technique. The left column shows the rescaled cross section at different average potential $\overline{V}$, while the right column gives the corresponding interference areas. (a) the FFT for $\overline{V} = -6.0$ eV, (b) $\overline{V} = -1.6$ eV, (c) $\overline{V} = 1.7$ eV and (d) $\overline{V} = 4.35$ eV.*

# Chapter 5

# Ion pair formation of the hydrogen-fluoride ion

The unique physics characteristics of the hydrogen fluoride ion $HF^+$ and the abundance of the neutral system HF in nature and industry have raised the interest to study its destruction processes dissociative recombination (DR) and ion pair formation (IPF). The neutral molecule was discovered in interstellar clouds [17] and planetary atmospheres [64]. Furthermore HF plays meanwhile an important role in the manufactoring process of electronics and in the photochemical industries. Additionally its properties in etching plasmas [75] and chemical lasers are of

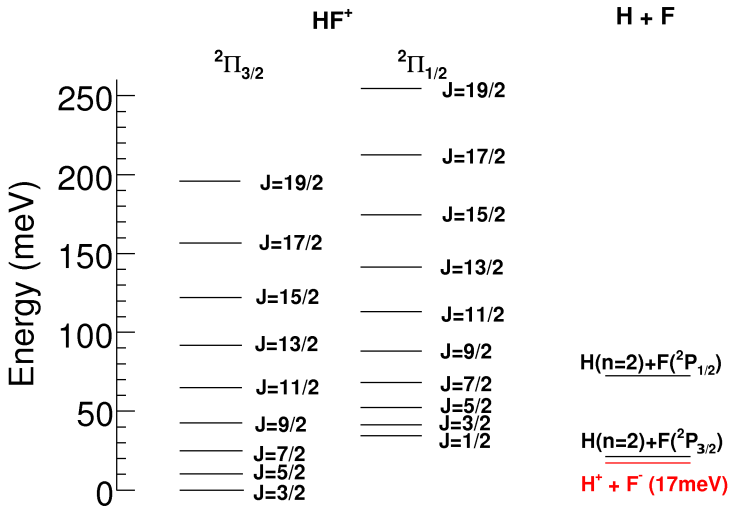


Figure 5.1: *Level scheme of $HF^+$. Left hand side the two ground state configurations of the ion; right hand side the final energy levels ( F in its ground state) accessible at these energies.*

strong interest. The much higher ionization potential of the F atom (17.423 eV) [59] compared to that of the H atom (13.598 eV) creates unique characteristics of the molecular system. This results in effectively isolated ground and excited potential energy curves (PECs). While the ground and the first excited ionic state are shown in figure 5.2 (rotational levels of the ionic ground state are presented in figure 5.1) higher excited states are not shown due to the fact that they are located almost 4 eV above. The lowest two ionic states converge to the same asymptotic limit $H^+ + F(^2P)$. Thereby the excited state correlates to the $H^+ + F(^2P_{1/2})$, whereas both spin-orbit components of the ground state, with a spin-orbit coupling in the order of 30 meV, correlate to the $H^+ + F(^2P_{3/2})$. Both final states are separated by 50 meV (figure 5.1).
In figure 5.2 also the potential energy curve $V\ ^1\Sigma^+$ leading to ion pair products is shown (final energy level: red line in figure 5.1). For this state, which is especially important for both DR and IPF processes, calculations have not yet converged so that two curves can currently be found in literature [4; 41] and are thus shown in figure 5.2. Additionally the first Rydberg state is shown with its dissociation limit $H(n=2) + F(^2P_{1/2})$ [4], as well as an approximate curve which converges to the

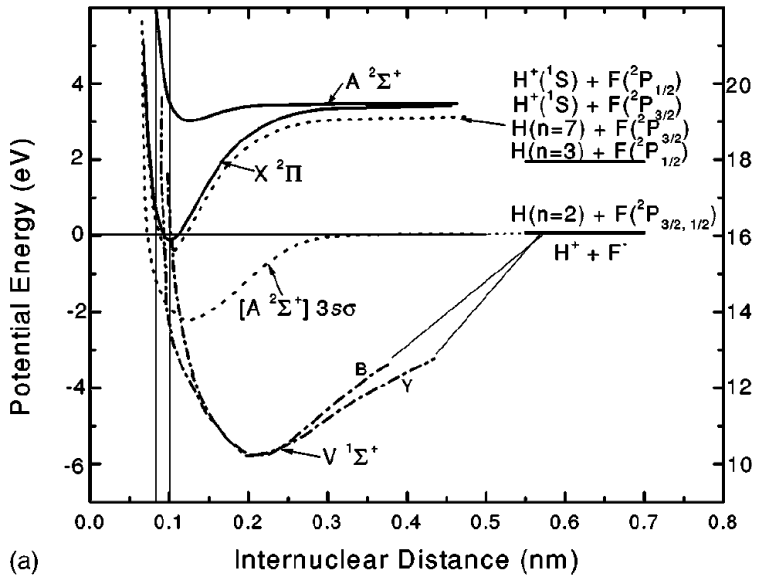


Figure 5.2: *Relevant potential energy curves for $HF^+$ [58]. Bold lines: Ground and first excited state [5]. Dot-dashed curve: two possible curves for the ion pair state [4; 41] (see text). Dotted line: Rydberg state converging to the $H(n=2) + F(^2P_{3/2,1/2})$ [5] and Rydberg state which converges to the ground-ionic state $H^+(^1S) + F(^2P_{3/2,1/2})$. The two vertical lines deifine the Frank-Condon region for the excitation from the ground state of HF*

ground-ion state, producing hydrogen in the n=7 level.
In the following, the IPF process will be described in more detail before first results of experiments at the TSR will be presented and compared to previous CRYRING experiments and theory.

## 5.1 Ion pair formation of $HF^+$

In contrast to previously discussed molecular systems both the DR and IPF process can be initiated already at low energies. IPF can thereby either proceed along a direct (equation 5.1) or an indirect (equation 5.2) pathway as soon as the energy threshold of 17 meV (see figure 5.1) is reached:

$$HF^+(v=0) + e^- \rightarrow HF^{**} \rightarrow H^+ + F^- + KER \quad (5.1)$$

$$HF^+(v=0) + e^- \rightarrow HF^{Ryd}_{nv} \rightarrow HF^{**} \rightarrow H^+ + F^- + KER. \quad (5.2)$$

This is generally already realized even at zero electron energy taking the thermal rotational energies of the ion (figure 5.1) and the energy resolution of the storage ring into account. Not shown here is the second ion pair channel, producing a negative hydrogen and a positive fluorine atom, because it is due to the extremely small mass ratio of fragment and initial ion, almost impossible to detect (cf. chapter 3). DR and IPF involve stabilization along the same compound state $HF^{**}$, which can induce similarities between both rate coefficients [58].

## 5.2 Ion pair formation measurement at the TSR

The ions for the IPF measurement were produced by the penning source located inside the ISSI accelerator and accelerated to an energy of 2.56 MeV. Using the TSR's synchrotron mode the ions were further accelerated inside the storage ring to a final energy of 4.66 MeV. The electron cooler was not used during these measurements since the low beam intensity available after accelerating did not allow an alignment of the electron beam. Thus the electron target provided electrons for the cooling and measurement. Thereby the cooling energy was set to 129.46 V, which leads with an electron current of 355 $\mu$A to an electron density $n_e$ of $2.34610^6$ cm$^{-3}$ and to a space charge corrected cooling energy of 127.06 V.
The detector counts of DEMON ($F^-$) and MIDAS ($F^+$ for normalization) were recorded by the ADC, the scaler and the VME interface and stored into a raw data file. The precooling step lasted 3 s whereas the measurement wobble cycle was set to 19.8 s. In this cycle the cooling, reference and measurement step lasted each for 50 ms, and were repeated 120 times. Due to the fact that only the electron target was used, both the energy of the cooling and measurement step were set to cooling energy to increase the interstage cooling time.

**Data processing.** The data processing procedure mainly follows the one described in chapter 3.4.3. However, the partial overlap of the background and the $F^-$ signal in the ADC spectrum (see figure 3.26) required to take special care in the analysis. In order to avoid a dominant background contribution the ADC spectrum was cut at an ADC bit of 1200. The influence of the remaining background events could then be estimated by comparing measurements with and without the ion beam, while switching off the electrons. Both measurements show the same amount of counts per time unit originating from stray light inside the TSR (black curve in figure 3.26). This contributes as a constant time-normalized offset $c$ in the measured signal, which was then subtracted from the raw count rate of the time normalized $F^-$ signal $R_{F^-}$ to yield the background corrected rate $R_{bc} = R_{F^-} - c$. This rate is finally analyzed, as mentioned above, according to chapter 3.4.3. The final rate is then scaled to the previously measured absolute rate coefficient obtained at CRYRING [58], because the low beam intensity (see beginning of this section) did not allow a calibration to the ion beam itself.

## 5.3 Results and Discussion

The analyzed data is shown in figure 5.3 in comparison with the previous CRYRING experiment. The rate coefficient was measured up to energies of 10 eV, showing a constant value above 3.5 eV. Therefore only the data at energies below 3.5 eV is presented here. Overall one can note, that the rate coefficient follows the threshold law up to about 0.1 eV and is in contrast to other molecular systems significantly larger in comparison to the DR rate $\alpha_{DR}$ ($\alpha_{IPF}/\alpha_{DR} \simeq 0.13$ compared to e.g. $HD^+$ where $\alpha_{IPF}/\alpha_{DR} \simeq 0.04$; see chapter 4 and [52]).
The rate coefficient of the ion pair formation features no energetic threshold neither in the TSR experiment nor in the CRYRING experiment (figure 5.3(a)), despite its theoretical prediction (see figure 5.3(b) and [58]). This can be explained since the threshold energy of 17 meV is easily exceeded considering the expected rotational excitation at 300 K (25 meV) and the energy resolution of the electron beam. However, the decreasing rate coefficient (see figure 5.3(a)) shows a small peak at about 17 meV which might be a hint at the opening of the ion pair channel and threshold, respectively. Studying the measurements of Yencha et al [4] including photo-ion-pair formation, the peaks were assigned by Djuric et al [58]. Therein the first peak at 20 meV (1) (see mark with label in figure 5.3(a)) is assigned to the high vibrational states ($v \approx 18$) of the predissociating molecular state $[A^2\Sigma^+]3s\sigma$ (see figure 5.2); this state correlates to the final state $H(n = 2) + F(^2P_{1/2})$ lying about 55 meV above the ion pair channel (see figure 5.1). The peaks at higher energies are connected to the n = 7,8 Rydberg states with $v = 1$ converging to the molecular curves $HF^+$ $[X^2\Pi_{3/2,1/2}]$ [4; 58]. The local maximum at 90 meV (2) is

then assigned to n = 7, whereas the maximum at 140 meV (3) and the shoulder (200 meV) (4) of this peak correspond to the n = 8 Rydberg states. In [58] the peaks at higher relative energies (380 meV (5) and 600 meV (6)) are connected to the vibrational levels of the second predissociating molecular state $[A^2\Sigma^+](3p\sigma)$ which converges to the $[A^2\Sigma^+]$ excited ionic state shown in figure 5.2. However, the peak positions in the photo-ion pair formation are energetically slightly displaced from the electron induced ion pair results due to the differences in the experimental setups and the different equilibrium internuclear separation in the ground state of HF ($r = 1.001a_0$) and $HF^+$ ($r = 1.224a_0$) [58].
Furthermore additional peak structures were observed in the present experiments at electron collision energies higher than 1 eV. In this energy range neither the photoionization measurements [4] nor theory (see figure 5.3) [9] can explain the structure, although the results of [9] can give a hint on the origin of the observed rate coefficient. On the other hand the count rate was here significantly higher than the stray light induced constant background. Also restgas induced background events can be excluded from the background measurement so that this rate has to originate from electron induced $F^-$ fragments hitting the crystal. Nevertheless the statistics are very poor at these energies giving an error of the rate coefficient of up to about 75% at an energy of 3.5 eV, with an even higher uncertainty at higher energies (not shown in figure 5.3). Therefore further measurements have to be performed in order to improve the quality of the rate coefficient at energies larger than 1 eV.

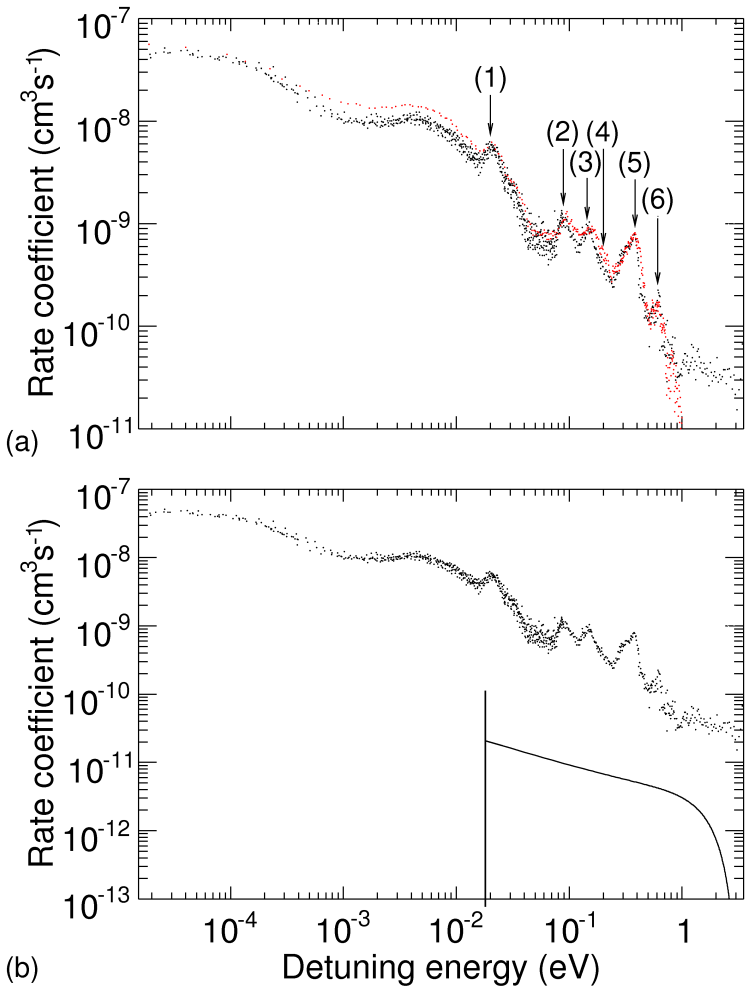


Figure 5.3: *Comparison of the present $HF^+$ experiment (black) with the previous CRYRING experiment ((a), red) and theory ((b), black solid line). (a) Both measurements show an overall agreement up to 1 eV, while the theoretical rate coefficient (b) is about two orders of magnitudes lower and does not show any of the observed structures. The vertical line in (b) indicates the theoretical ion pair threshold.*

# Chapter 6

# Summary and Outlook

A new detector system for strongly deflected molecular fragments, complementing the existing electron target setup, has been installed at the TSR and has been used to study ion pair formation (ion pair formation) in electron collisions of $HD^+$, $H_3^+$ and $HF^+$

## 6.1 The new DEMON setup

The new detector setup was installed and taken into operation in 2005. Improving the initial design a new lightguide has been developed. Later, also an Avalanche Photodiode (APD) has additionally been tested as a detector of the light emitted by the YAP:Ce scintillator upon fragment impact. Various tests have been performed, both with and without a stray-light-screening aluminum foil covering the scintillator surface. While the first case could only be tested with the lightguide setup the second was tested with the APD as well as the lightguide setup. The results indicate that the stray light contribution during the measurement without the foil worsens the overall energy resolution of the detector, in the case of the APD setup up to the point of the detector becoming unusable for $F^-$ fragments. It has been shown (chapter 3) that the lightguide setup operated reliably in all presented experimental conditions. Further experiments are necessary to get an overview over the fragment mass range that is detectable using this setup. The mass ratio between that of the fragment to that of the initial ion is limited for reasons of fragment ion deflection in the storage ring to a range above about one third, as has been demonstrated by the large special corrections necessary for $H_3^+$ (mass ration 0.33). Lighter masses will have an even larger spread of the fragment cone and will require even larger systematical corrections of the data

## 6.2 Ion pair formation of $HD^+$

The measurement on $HD^+$ demonstrates the high energy resolution available, thanks to the twin electron beam setup at the TSR: the ion pair formation cross section shows a total number of 14 well resolved peaks. Below the dissociation limit of 2.668 eV five peaks are visible, while in previous experiments performed at Cryring only four, considerably less well resolved peaks were visible. The observed threshold energy of (1.92±0.04) eV fits within its uncertainty to the theoretical one of 1.913 eV. The cross section shows a maximum of $3.4 \times 10^{-19}$ cm$^2$ with a steady decrease up to an energy of about 6 eV, followed by a step in the cross section. The oscillatory structure continues up to energy of about 12 eV. Newest calculations as well as an empirical FFT treatment of this cross section show, that the interference effect to the overwhelming part stems from only two potential energy curves (labeled with 3d and 5g in figure 4.4) in the energy range 1.92 eV $< E_e <$ 6 eV. Efforts are underway to extent the calculations to higher collision energies, which requires the inclusion of more states into the model.

## 6.3 Ion pair formation of $H_3^+$

The $H_3^+$ experiment drove the experimental setup to its limits. This was due to the large deflection of the light hydrogen fragments in the toroid fields of the electron target and the following vertical correction magnets of the electron target, which are not able to bend the ionic fragments back onto their original trajectory. Several corrections had to be applied in order to be able to detect the light $H^-$ fragments. However the overfocusing of the ring optics could not be compensated. The resulting lower detector efficiency had to be systematically corrected in the data analysis (see chapter 4.3). Thanks to the 100% efficiency of the MIDAS detector for the $H_2^+$ fragments, it was possible to distinguish the two possible ion pair channels by the coincidence technique. Here the $H_2^+$ fragments were measured in coincidence with the $H^-$ fragments thereby giving access to the two body channel (see figure 4.13). The three body channel could then be extracted from the total $H^-$ count rate by subtracting the cross section of the two body channel from the total $H^-$ cross section. Both channels show the theoretically calculated energy thresholds of 5.4 and 8.1, respectively. For the first time interference effects in the ion pair formation cross section of $H_3^+$ have been observed. Up to now, no theory fits to the experimental data. Also with the empirical FFT method no reasonable result could be obtained, which is mainly due to the too simple model used for the application of the FFT.

## 6.4 Ion pair formation of $HF^+$

The latest results are about the ion pair formation of $HF^+$. In this case the rate coefficient shows an overall $1/\sqrt{E}$ dependence up to an energy of about 30 meV, followed by a steeper decline. Due to the low energy threshold of 17 meV, the presence of rotational excitations (25 meV at 300K), and the limited energy resolution of the storage ring technique no threshold energy could be observed. Up to an energy of around 100 meV the ion pair formation cross section competes with the DR cross section [58], which is unique among diatomic molecules. However the statistics of the measured cross section is good up to 3.5 eV, in contrast to earlier CRYRING data, where no conclusive results could be obtained above 1 eV. At the energies above 1 eV additional structure was observed in the TSR data. Unfortunately, the available theory is off by several orders of magnitude, and also the observed structure cannot be reproduced even qualitatively in present theoretical calculations.

## 6.5 Future experiments and possible new detectors

**Future experiments.** Upcoming experiments on ion pair formation involve $CF^+$ and $H_2^+$ ions. While as mentioned above the former will push the detector to its limits, due to the low kinetic energy deposited in the crystal, the latter will allow to detect the isotopic effects between the deuterated diatomic hydrogen ion and the diatomic hydrogen ion, as has been proposed by X. Urbain [82] very recently. Additionally it is planned to examine the diatomic molecular ion $^3HeD^+$ which is the analogon to $^4HeH^+$. The ion pair formation rate coefficients and cross sections for these ions have not been measured up to now, but theoretical calculations exist. Ion pair formation in these cases can thus lead to a better understanding of the reaction dynamics involved and can help to improve theoretical models. Additionally this process would fill the "blank" at reactant-product mass ratio of 0.4 and could contribute to even better understanding of the storage ring and detector setup. A completely different possible application of the DEMON detector would be the measurement of electron induced double detachment of atomic anions, like

$$Li^- + e^- \rightarrow Li^+ + 2e^- \tag{6.1}$$

For such a measurement the TSR would obviously have to be operated at inverted polarity.

**New detector setups at the TSR.** As mentioned in chapter 3 the DEMON could with small reversible modifications installed also towards the inside of the

TSR. It would offer the detection of strongly deflected light fragments with the same charge as the stored ions, for example products released from heavier molecules. An almost identical copy of the DEMON detector installed at the inside position, together with DEMON operating outside, would yield access to a wider range of cation/anion coincidences similar to the case of $H_3^+$ studied here. This detector could in future finalize the entire new electron target setup, leading to a complete coverage of electron ion collision products, within the limitations presented in chapter 3.

# Appendix

## A Electronic layout of the Avalanche Photodiode (APD)

The Layout of the electronic circuit as used in the APD setup (chapter 3) is shown in 1. In figure 2 the layout of the circuit board is presented which includes the circuitry, as well as the APD (schematically included as squares in the middle (ochery)).

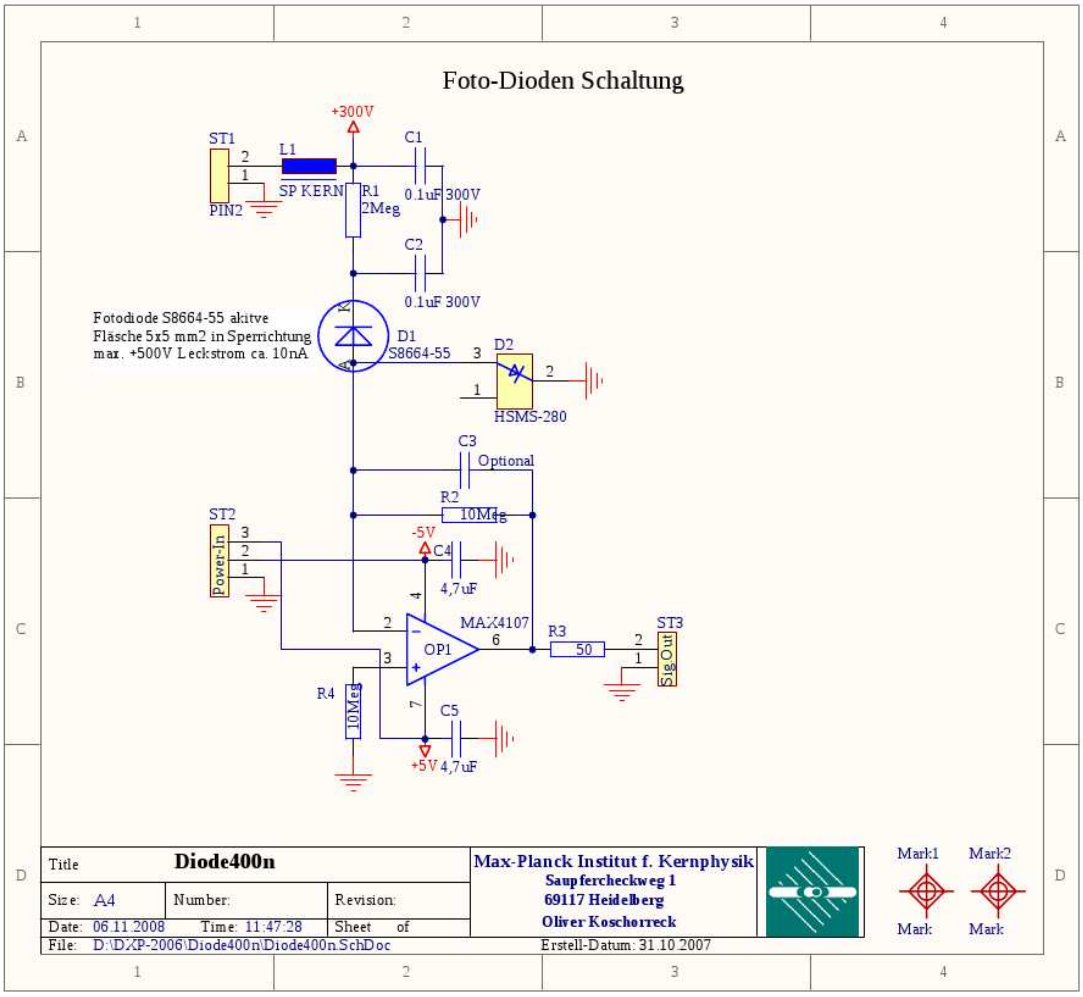


Figure 1: *Layout of the electronic circuit as used in the APD setup.*

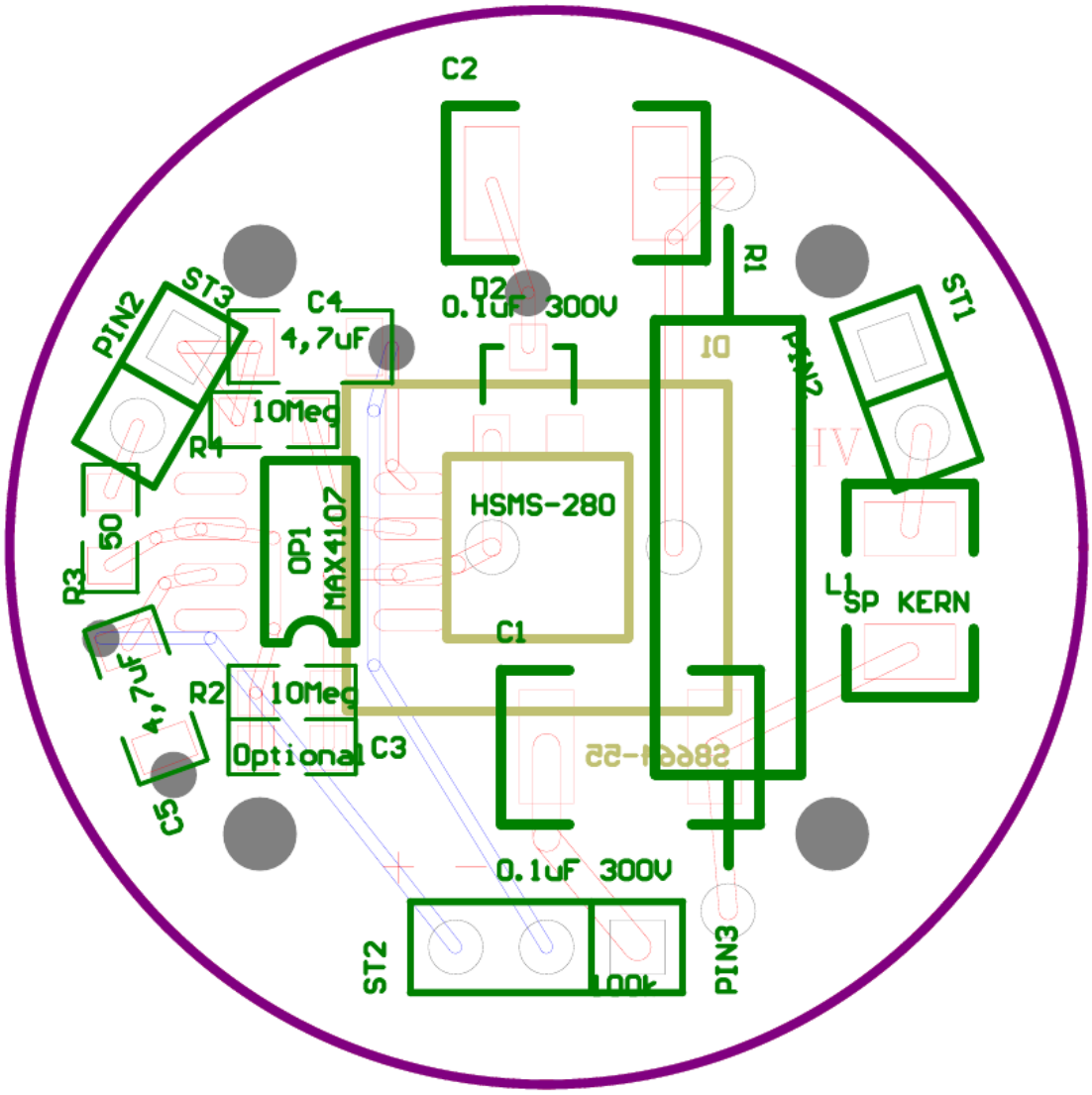


Figure 2: *Layout of the circuit board as used for the APD electronic circuit. Schematic included the APD (ocher)*

# B Fast Fourier Transformation (FFT)

In this chapter the FFT principle will be shortly explained in the formal description given by Cooley and Tukey. This formalism bases on a Discrete Fourier Transformation (DFT) with 2n points and is defined by

$$f_i = \sum_{k=0}^{2n-1} x_k e^{-\frac{2\pi i}{2n} jk} \qquad j = 0, \ldots, 2n-1. \tag{2}$$

If the $x_k$ with a even indices are redifened as follows

$$x'_0 = x_0,\ x'_1 = x_2,\ \ldots,\ x'_{n-1} = x_{2n-2} \tag{3}$$

and identify the transformed $x'_j$ using the DFT with the size n as

$$f'_0, \ldots,\ f'_{n-1} \tag{4}$$

the transformation is then given by

$$f_j = \begin{cases} f'_j + e^{-\frac{\pi i}{n} j} f''_j & ,j < n \\ f'_{j-n} - e^{-i\frac{\pi i}{n}(j-n)} f''_{j-n} & ,j \geq n \end{cases} . \tag{5}$$

The transformation is then calculated recursively.

# List of Figures

# Bibliography


**1** A. Giusti. A multichannel quantum defect approach to dissociative recombination. *J. Phys. B*, 13:3867, 1980.

**2** A. Lampert, A. Wolf, D. Habs, J. Kenntner, G. Kilgus, D. Schwalm, M. S. Pindzola and N. R. Badnell. High-resolution measurement of the dielectronic recombination of fluorinelike selenium ions. *Phys. Rev. A*, 53:1413, 1996.

**3** A. Neau, A. Derkatch, F. Hellberg, S. Rosén, R. Thomas, M. Larsson, N. Djurić, D. B. Popović, G. H. Dunn and J. Semaniak. Resonant ion pair formation of $HD^+$: Absolute cross sections for the $H^- + D^+$ channel. *Phys. Rev. A*, 65:044701, 2002.

**4** A. Yencha, A. Hopkirk, J. B. Grover, B.-M. Cheng, H. Lefebvre-Brion and F. Keller. Ion-pair formation in the photodissociation of HF and DF. *Jour. Chem. Phys.*, 103:2882, 1995.

**5** A. Yencha, A. J. Cormack, R. J. Donovan, A. Hopkins and G. C. King. Threshold photoelectron spectroscopy of HF and DF in the outer valence ionization region. *Jour. Phys. B*, 32:2539, 1999.

**6** Å. Larson, 2008. private communication.

**7** Å. Larson and A. E. Orel. Ion-pair formation and product branching ratios in dissociative recombination $HD^+$. *Phys. Rev. A*, 64:062701, 2001.

**8** Å. Larson, J. Roos and A. E. Orel. Ion-pair formation in electron recombination with $H_3^+$. *Phil. Trans. R. Soc. A*, 364:2999, 2006.

**9** Å. Larson, J. Roos, M. Stenrup and A. E. Orel. Ion-pair formation in electron recombination with molecular ions. *Jour. Phys. Conf. Ser.*, 88:012065, 2007.

**10** Å. Larson, N. Djurić, W. Zong, C. H. Greene, A. E. Orel, A. Al-Khalili, A. M. Derkatch, A. Le Padellec, A. Neau, S. Rosén, W. Shi, L. Vikor, H. Danared, M. af Ugglas, M. Larsson and G. H. Dunn. Resonant ion-pair formation in electron collisions with $HD^+$ and $OH^+$ . *Phys. Rev. A*, 62:042707, 2000.

**11** B. Franzke. The heavy ion storage and cooler ring project ESR at GSI. *Nucl. Instr. Methods B*, 24/25:18, 1987.

**12** B. J. McCall. *Spectroscopy of $H_3^+$ in laboratory and astrophysical plasmas.* PhD thesis, University of Chicago, 2001.

**13** B. J. McCall, A. J. Huneycutt, R. J. Saykally, N. Djuric, G. H. Dunn, J. Semaniak, O. Novotný, A. Al-Khalili, A. Ehlerding, F. Hellberg, S. Kalhori, A. Neau, R. D. Thomas, A. Paal, F. Österdahl and M. Larsson. Dissociative recombination of rotationally cold $H_3^+$. *Phys. Rev. A*, 70:052716, 2004.

**14** B. Peart, R. A. Forrest and K. Dolder. Measured cross sections for the formation of $H^-$ by collisions between $H_3^+$ ions and electrons. *Jour. Phys. B*, 12:3441, 1979.

**15** C. M. Lederer, V. S. Shirley. Table of Isotopes. Wiley Interscience, New York, 1978.

**16** C. Zener. Non-adiabatic crossing of energy levels. *Proc. R. Soc. London*, 137:696, 1932.

**17** D. A. Neufeld, J. Zmuidzinas, P. Schilke and T. G. Phillips. Discovery of interstellar hydrogen fluoride. *Astr. Jour. Let*, 488:141, 1997.

**18** D. A. Orlov, H. Fadil, M. Grieser, C. Krantz, J. Hoffmann, O. Novotny, S. Novotny and A. Wolf. Electron cooling with photocathode electron beams applied to slow ions at TSR and CSR. *Proceedings of COOL 2007*, page 230, 2007.

**19** D. Gerlich, E. Herbst and E. Roueff. $H_3^+ + HD \rightarrow H_2D^+ + H_2$: Low-temperature laboratory measurements and interstellar implications. *Planetary and Space Science*, 50:1275, 2002.

**20** E. J. Heller. The semiclassical way to molecular spectroscopy. *Acc. Chem. Res.*, 14:368, 1981.

**21** E. Traebert, S. Reinhardt, J. Hoffmann and A. Wolf. M1 transition rates in Co XI and Co XIII measured at a heavy-ion storage ring. *J. Phys. B*, 39:945–54, 2006.

**22** E. U. Condon. A theory of intensity distribution in band systems. *Phys. Rev.*, 28:1182, 1926.

**23** E. U. Condon. Nuclear motions associated with electron transitions in diatomic molecules. *Phys. Rev.*, 32:1182, 1928.

**24** E. W. Schmidt, S. Schippers, D. Bernhardt, A. Müller, J. Hoffmann, M. Lestinsky, D. A. Orlov, A. Wolf, D. V. Lukić, D. W. Savin and N. R. Badnell. Electron cooling: theory, experiment, application. *Phys. Rep.*, 196:135, 1990.

**25** F. B. Yousif, P. Van der Donk and J. B. A. Mitchell. Ion-pair formation in the dissociative recombination of $H_3^+$. *Jour. Phys. B*, 26:4249, 1993.

**26** F. Sprenger. *Production of cold electron beams for collision experiments with stored ions.* PhD thesis, Ruperto-Carola University of Heidelberg, Germany, 2003.

**27** G. A. Worth, M. H. Beck, A. Jäckle and H.-D. Meyer. The multiconfiguration time-dependent Hartree (MCTDH) method: a highly efficient algorithm for propagating wavepackets. *Phys. Rep.*, 324:1:1, 2000.

**28** G. Herzberg. Dissociation Energy and Ionization Potential of Molecular Hydrogen. *Phys. Rev. Lett.*, 23:1081, 1969.

**29** G. Kilgus. *Hochauflösende Messungen zur dielektronischen Rekombination.* PhD thesis, Ruperto-Carola University of Heidelberg, Germany, 2001.

**30** G. Wentzel. Eine Verallgemeinerung der Quantenbedingungen für die Zwecke der Wellenmechanik. *Zeits. f. Phys. A*, 38:518, 1926.

**31** G. Wissler. *Ein Detektorsystem für Umladungs- und Fragmentationsexperimente mit gespeicherten Ionen.* PhD thesis, Ruperto-Carola University of Heidelberg, Germany, 2002.

**32** H. A. Kramers. Wellenmechanik und halbzahlige Quantisierung. *Zeits. f. Phys. A*, 39:828, 1926.

**33** H. Buhr. *Electron collisions and internal excitation in stored molecular ion beams.* PhD thesis, Ruperto-Carola University of Heidelberg, Germany, 2006.

**34** H. Buhr et al. to be published.

**35** H. Buhr, H. B. Pedersen, S. Altevogt, V. Andrianarijaona, H. Kreckel, L. Lammich, S. Novotny, D. Strasser, J. Hoffmann, M. Lange, M. Lestinsky, M. B. Mendes, M. Motsch, O. Novotný, D. Schwalm, X. Urbain, D. Zajfman and A. Wolf. Inelastic electron collisions of th eisotopically symmetric helium dimer ion $^4He_2{}^+$ in a storage ring. *Phys. Rev. A*, 76:022713, 2007.

**36** H. C. Bryant, A. Mohagheghi, J. E. Stewart, J. B. Donahue, C. R. Quick, R. A. Reeder, V. Yuan, C. R. Hummer, W. W. Smith, S. Cohen, W. P. Reinhardt and L. Overmann. Oberservation of motional-field-induced ripples in the photodetachment cross section of $H^-$. *Phys. Rev. Lett.*, 58:2412, 1987.

**37** H. Kreckel, L. Lammich, M. Lange, J. Levin, M. Scheffel, D. Schwalm, J. Tennyson, Z. Vager, R. Wester, A. Wolf and D. Zajfman. Vibrational and rotational cooling of $H_3^+$. *Phys. Rev. Lett.*, 95:263201, 2005.

**38** H. Kreckel, M. Motsch, J. Mikosch, J. Glosik, R. Plasil, S. Altevogt, V. Andrianarijaona, H. Buhr, J. Hoffmann, L. Lammich, M. Lestinsky, I. Nevo, S. Novotny, D. A. Orlov, H. B. Pedersen, F. Sprenger, A. S. Terekhov, J. Toker, R. Wester, D. Gerlich, D. Schwalm, A. Wolf and D. Zajfman. High-Resolution Dissociative Recombination of Cold $H_3^+$ and First Evidence for Nuclear Spin Effects. *Phys. Rev. Lett.*, 95:263201, 2005.

**39** H. Poth. Electron cooling: theory, experiment, application. *Phys. Rep.*, 196:135, 1990.

**40** J. B. Roos, Å. Larson and A. E. Orel. Dissociative recombination of $HF^+$. *Phys. Rev. A*, 78:2508, 2008.

**41** J. Berkowitz, W. A. Chupka, P. M. Guyon, J. H. Holloway and R. Spohr. Photoionization Mass Spectrometric Study of $F_2$, HF and $DF^*$. *Jour. Chem. Phys.*, 54:5165, 1973.

**42** J. Franck. Elementary processes of photochemical reactions. *Trans. Faraday Soc.*, 21:536, 1926.

**43** J. Liebmann. *Synchrotronbetrieb am Schwerionenspeicherring TSR.* PhD thesis, Ruperto-Carola University of Heidelberg, Germany, 1993.

**44** J. Stützel, 2008. private communication.

**45** J. W. Cooley and J. W. Tukey. An algorithm for the machine calculation of complex Fourier series. *Math. Comput.*, 19:297, 1965.

**46** K. Abrahamsson, G. Andler, L. Bagge, et al. CRYRING - a synchroton cooler and storage ring. *Nucl. Instr. Meth. Phys. Resa. B*, 79:269–272, 1993.

**47** L. Brillouin. La mécanique ondulatoire de Schrödinger; une méthode générale de resolution par approximations successives. *Comptes Rendus*, 183:24, 1926.

**48** M. Born, R. Oppenheimer. Zur Quantentheorie der Molekeln. *Annalen der Physik*, 389:457, 1927.

**49** M. Frigo and S. G. Johnson. The Design and Implementation of FFTW3. *Proceedings of the IEEE*, 93(2):216, 2005. special issue on "Program Generation, Optimization and Platform Adaptation".

**50** M. Grieser, 2008. private communication.

**51** M. Grieser, H. Deitinghoff, D. Habs, R. von Hahn, E. Jaeschke, C.-M. Kleffner, V. Kössler, S. Papureanu, R. Repnow, M.-H. Rhee, D. Schwalm and A. Schempp. Upgrading of the Heidelberg accelerator facility with a new high current injector. *Nucl. Instrum. Methods A*, 328:160, 1993.

**52** M. Lange. *Competition between Reaction Channels in Electron Collision of the Hydrogen Molecular Ion $HD^+$*. PhD thesis, Ruperto-Carola University of Heidelberg, Germany, 2002.

**53** M. Larsson. Dissociative recombination with ion storage rings. *Annu. Rev. Phys. Chem.*, 48:151, 1997.

**54** M. Larsson, 2007. private communication.

**55** M. Larsson, A. E. Orel. *Dissociative Recombination of Molecular Ions*. Cambridge University Press, 2008.

**56** M. Larsson, M. Carlson, H. Danared, L. Broström, S. Mannervik and G. Sundström. Vibrational cooling of $D_2^+$ in an ion storage ring as revealed by dissociative recombination measruements. *J. Phys. B.*, 27:1397–1406, 1994.

**57** M. Lestinsky. *High-resolution electron collision spectroscopy with multicharged ions in merged beams*. PhD thesis, Ruperto-Carola University of Heidelberg, Germany, 2007.

**58** N. Djurić, G. H. Dunn, A. Al-khalili, A. M. Derkatch, A. Neau, S. Rosén, W. Shi, L. Vikor, W. Zong, M. Larsson, A. Le Padellec, H. Danared and M. af Ugglas. Resonant ion pair formation and dissociative recombination in electron collisions with ground-state $HF^+$ ions. *Phys. Rev. A*, 64:022713, 2001.

**59** NIST Chemistry WebBook. http://webbook.nist.gov/chemistry/.

**60** O. Novotný, 2008. private communication.

**61** O. Novotný, O. Motapon, M. H. Berg, D. Bing, H. Buhr, H. Fadil, J. Hoffmann, A. S. Jaroshevich, B. Jordon-Thaden, C. Krantz, M. Lange, M. Lestinsky, M. B. Mendes, S. Novotny, A. Petrignani, D. A. Orlov, I. F. Schneider, A. E. Orel and A. Wolf. Dissociative recombination of $CF^+$: experiment and theory. *J. Phys.: Conf. Ser.* submitted.

**62** P. Baumann, M. Blum, A. Friedrich, C. Geyer, M. Grieser, B. Holzer, E. Jaeschke, D. Krämer, C. Martin, K. Matl, R. Mayer, W. Ott, B. Povh, R. Repnow, M. Steck, E. Steffens and W. Arnold. The Heidelberg ion test storage ring TSR. *Nucl. Instr. Meth. A*, 268:531, 1988.

**63** P. C. Cosby and H. Helm. Photodissociation of Triatomic Hydrogen. *Phys. Rev. Lett.*, 61:298, 1988.

**64** P. Connes, J. Connes, W. S. Benedict and L. D. Kaplan. Traces of HCl and HF in the atmosphere of Venus. *Astrophys. Jour.*, 147:1230, 1967.

**65** PAW. http://paw.web.cern.ch.

**66** ROOT. http://root.cern.ch.

**67** S. Datz, G. Sundström and Ch. Biedermann. Branching processes in the dissociative recombination of $H_3^+$. *Phys. Rev. Lett.*, 74:896–899, 1995.

**68** S. Kalhori, R. Thomas, A. Al-Khalili, A. Ehlerding, F. Hellberg, A. Neau, M. Larsson, Å. Larson, A. J. Huneycutt, B. J. McCall, N. Djurić, G. H. Dunn, J. Semaniak, O. Novotný, A. Paál, F. Österdahl and A. E. Orel. Resonant ion-pair formation in electron collisions with rovibrationally cold $H_3^+$. *Phys. Rev. A*, 69:022713, 2004.

**69** S. Krohn. *Inelastic collisions and recombination between electrons and molecular ions.* PhD thesis, Ruperto-Carola University of Heidelberg, Germany, 2001.

**70** S. Krohn, Z. Amitay, A. Baer, D. Zajfman, M. Lange, L. Knoll, J. Levin, D. Schwalm, R. Wester and A. Wolf. Electron-induced vibrational deexcitation of $H_2^+$. *Phys. Rev. A*, 62:032713, 2000.

**71** S. Novotny. Fast-beam molecular fragmentation imaging using a high-speed gated camera system. Diploma thesis, Ruperto-Carola University of Heidelberg, Germany, 2004.

**72** S. Novotny. *Fragmentation of molecular ions in slow electron collisions.* PhD thesis, Ruperto-Carola University of Heidelberg, Germany, 2008.

**73** S. P. Møller. ELISA, an electrostatic storage ring for atomic physics. *Nucl. Inst. Meth. Phys. Res. A*, 394:281, 1997.

**74** S. Schröder. *Laser cooling and ion beam diagnostics of relativistic ions in a storage ring.* PhD thesis, Johannes Gutenberg University of Mainz, Germany, 1990.

**75** T. Hoshino and Y. Nishioka. Etching process of $SiO_2$ by HF molecules. *Hour. Chem. Phys.*, 111:2109, 1999.

**76** U. Weigel. *Cold intense electron beams from Gallium Arsenide photocathodes.* PhD thesis, Ruperto-Carola University of Heidelberg, Germany, 2003.

**77** V. G. Baryshevsky, M. V. Korzhik, V. I. Moroz, V. B. Pavlenko and A. A. Fyodorov. Properties of the YAP:Ce scintillator. *Nucl. Instr. Meth. B*, 58:291, 1991.

**78** V. Georgieva, A. Bogaerts and R. Gijbels. Numerical study of $Ar/CF_4/N_2$ discharges in single- and dual-frequency capacitively coupled plasma reactors. *J. Appl. Phys.*, 94:3748, 2003.

**79** V. Sidis, C. Kubach and D. Fussen. Ionic-covalent problem in the $H^+ + H^- \leftrightarrow H^* + H$ collisional system. *Phys. Rev. A*, 27:2431, 1983.

**80** W. J. Van der Zande, J. Semaniak, V. Zengin, et al. Dissociative recombination: product information and very large cross sections of vibrationally excited $H_2^+$. *Phys. Rev. A*, 54:5010–5018, 1996.

**81** W. Zong, G. H. Dunn, N. Djurić, M. Larsson, C. H. Green, A. Al-Khalilil, A. Neau, A.M. Derkatch, L. Vikor, W. Shi, A. Le-Padellec, S. Rosén, H. Danared and M. af Ugglas. Resonant Ion Pair Formation in Electron Collisions with Ground State Molecular Ions. *Phys. Rev. Lett.*, 83:951, 1999.

**82** X. Urbain, 2008. private communication.

**83** Z. Amitay, D. Zajfman and P. Forck. Rotational and vibrational lifetime of isotropically asymmetrized homonuclear diatomic molecular ions. *Phys. Rev. A*, 50:2304, 1994.

# Danksagung

es ist geschafft... nun ist es zeit, Danke zu sagen all denjenigen die zu dem Gelingen dieser Arbeit beigetragen haben

Als aller erstes geht ein herzliches Danke an Herrn Prof. Dr. Andreas Wolf für die Möglichkeit, in seiner Gruppe forschen, arbeiten und lernen zu dürfen, wobei er mich mit großem Engagement und vor allem Geduld unterstützt hat. Desweiteren vielen Dank an Herrn Prof. Dr. Thomas Stöhlker der sich bereit erklärt hat, sich Zeit zu nehmen um das Zweitgutachten für diese Arbeit zu erstellen.
An dieser Stelle bleibt nun auch Zeit allen aktuellen und ehemaligen Kollegen für ihre Unterstützung zu danken, allen voran Steffen und Claude für die großartige Betreuung und Hilfe während des Schreibens der vorliegenden Arbeit... ohne sie wäre ich vielleicht gar nicht fertig geworden. Vergessen möchte ich aber auch nicht MiLe für seine Unterstützung und Geduld bei meinem erlernen der Linux-Grundkenntnisse... Ich sag nur "lies die man-page", was ich mittlerweile tatsächlich schätzen gelernt habe, aber auch für sein Verständnis bei meinen Fragen. Allen anderen möchte ich einfach nur noch einmal danken für die Unterstützung bei den Experimenten, für die Laufmotivation und für die tolle Atmosphäre im Kochclub. Es sind dies namentlich: Henrik Buhr, Dennis Bing, Mario Mendes, Max Berg, Julia Stützel, Brandon Jordan-Thaden, Annemieke Petrignani, Andrey Shornikov, Dmitry Orlov, sowie die ehemaligen und auswärtigen Helfer Holger Kreckel, Lutz Lammich, Henrik Petersen und Simon Altevogt.
Bei Dr. Manfred Grieser und Kurt Horn möchte ich mich dafür bedanken daß sie immer den Ionenstrahl in die richtig Richtung gebogen haben. Bei der Beschleuniger Crew um Dr. Roland Repnow, Dr. Robert von Hahn, Manfred König und bei allen Operateuren der Tag- und Spätschichten, sowie den Notdiensten möchte ich mich für die Ionen bedanken, die sie immer in ausreichendem Maße bereit stellten.
Meinen besonderen Dank geht auch an Prof. Xavier Urbain, der die Theorie Rechnungen für unsere $HD^+$ Daten machte und mit dem es sehr ertragreiche Diskussionen über Crossings und Potentialkurven gab.
Nicht zu vergessen ein Danke an die Werkstätten unter der Leitung von Herrn Mallinger und Herrn Hahn. Gerade letztere machte durch Ihre Hilfsbereitschaft in jeder noch so aussichtslosen Lage meine Experimente erst möglich. Auch Oliver Koschorreck gebührt ein Dankeschön für die Hilfe bei allen Elektronikangelegenheiten vom Ausheizen bis zum Bau des APD setups. Dabei gilt mein besonderer Dank Christian Kaiser, der auch stets ein offenes Ohr für Dinge abseits der Arbeit hatte.

Ein weiteres Danke an die gute Fee des MPI, Helga Krieger, die immer wieder hilfsbereit war wenn es um organisatorische Dinge ging und u.a. unseren Kochclub stehts unterstützt hat. Aber auch Herrn Gernot Vogt danke ich für das Auffinden und besorgen noch so exotischer oder alter Paper.

Vielen vielen Dank an meine Familie: Danke an meinem Vater, der mein Studium finanziell unterstützt hat, meiner Schwägering, die meine Frau unterstützt hat bei der Kinderbespassung, meiner Schwiegermutter für ihre Hilfe in jeglicher Hinsicht und bei meinem Schwiegervater ebenfalls für seine Hilfsbereitschaft, gerade beim durchlesen dieser Arbeit und mich abzulenken bei den entspannenden Fussballnachmittagen. Bei meinem Bruder mit Familie möchte ich mit dafür bedanken, dass er einfach da war, wenn ich ihn brauchte.

Zu guter Letzt möchte ich mich bei den wichtigsten Personen in meinem Leben bedanken. Zu einem bei meinem Sohn Finn und meiner Tochter Lara, deren Lachen und Freude am Leben mich immer allen Stress und Kummer vergessen ließen und natürlich bei meiner geliebten Frau, die mich bedingungslos in jeder Hinsicht unterstützt und ohne die diese Arbeit nie zustande gekommen wäre.

Vielen Dank an alle (auch an die, die ich vergessen habe...)